1.0
1.1
1.25   1.4   1.6

4.5
5.0
5.6
6.3

2.8   2.5
3.2   2.2
3.6
4.0   2.0
1.8

MICROCOP`   CHART

AD-A166 774

AD

MTL TR 85-31

NONDESTRUCTIVE EVALUATION OF METAL MATRIX COMPOSITES

December 1985

S. W. SCHRAMM, G. M. KOLLER and J. W. ADAMS
IIT Research Institute
10 West 35th Street
Chicago, IL 60616

FINAL REPORT   Contract No. DAAG46-82-C-0039

DTIC FILE COPY

DTIC
ELECTE
S
APR 1 7 1986
D
D

Prepared for

U.S. ARMY MATERIALS TECHNOLOGY LABORATORY
Watertown, Massachusetts 02172-0001

86 4 17 018

REPORT DOCUMENTATION PAGE		READ INSTRUCTIONS BEFORE COMPLETING FORM
1. REPORT NUMBER MTL TR 85-31	2. GOVT ACCESSION NO. ADA166 774	3. RECIPIENT'S CATALOG NUMBER
4. TITLE (and Subtitle) NONDESTRUCTIVE EVALUATION OF METAL MATRIX COMPOSITES		5. TYPE OF REPORT & PERIOD COVERED Final Report 4/12/82 to 6/30/84
		6. PERFORMING ORG. REPORT NUMBER IITRI-K06035-30
7. AUTHOR(s) S. W. Schramm, G. M. Koller and J. W. Adams		8. CONTRACT OR GRANT NUMBER(s) DAAG46-82-C-0039
9. PERFORMING ORGANIZATION NAME AND ADDRESS IIT Research Institute 10 West 35th Street Chicago, IL 60616		10. PROGRAM ELEMENT, PROJECT, TASK AREA & WORK UNIT NUMBERS D/A Project: 1L263102071
11. CONTROLLING OFFICE NAME AND ADDRESS U.S. Army Materials Technology Laboratory ATTN: SLCMT-ISC Watertown, MA 02172-0001		12. REPORT DATE December 1985
		13. NUMBER OF PAGES 107
14. MONITORING AGENCY NAME & ADDRESS(if different from Controlling Office)		15. SECURITY CLASS. (of this report) Unclassified
		15a. DECLASSIFICATION/DOWNGRADING SCHEDULE

16. DISTRIBUTION STATEMENT (of this Report)

Approved for public release; distribution unlimited.

17. DISTRIBUTION STATEMENT (of the abstract entered in Block 20, if different from Report)

18. SUPPLEMENTARY NOTES

19. KEY WORDS (Continue on reverse side if necessary and identify by block number)

Metal matrix composites;   Fiber-reinforced composites;
Nondestructive testing   Castings;
Magnesium   Aluminum oxides

20. ABSTRACT (Continue on reverse side if necessary and identify by block number)

SEE REVERSE

Block No. 20

ABSTRACT

The objective of this program was to apply nondestructive evaluation (NDE) methods to identify potentially harmful casting defects in FP/ magnesium composites; establish detectability and reproducibility limits of NDE applied to FP/magnesium composites; and establish relationships between casting defects and failure modes of FP/magnesium composites. The material investigated was ZE41A magnesium alloy reinforced with FP (aluminum oxide) fibers. The 27 coupons (four coupons each of five flaw types and seven coupons from a related program, Contract No. DAAC46-80-C-0070) were evaluated using ultrasonic scanning, wave propagation velocity, and wave attenuation inspection techniques. The coupons evaluated were 12.7 cm (5 in.) long x 3.8 cm (1.5 in.) wide x 0.6 cm (0.25 in.) thick, with a fiber volume fraction of 0.50. After the detectability and reproducibility NDE inspections, tensile and/or bend specimens were machined from the parent coupons, strain gaged, and statically loaded to failure. Micrographs were made of the fracture surfaces for comparison with the NDE records. It was found that ultrasonic scanning using a 20 MHz compression wave, focused transducer operated in the pulse-echo mode generating an analog C-scan provided 100% detectability and reproducibility of the intentionally flawed coupons. Keywords:

FOREWORD

This is the final report of IIT Research Institute Project No. K06035, "Nondestructive Evaluation of Metal Matrix Composites," prepared by IITRI for the U.S. Army Materials Technology Laboratory (MTL), under Contract No. DAAG46-82-C-0039. The work described in this report was conducted during the period 12 April 1982 to 30 June 1984; previous related work was performed under Contract No. DAAG46-80-C-0070, reported in AMMRC TR 82-35. Mr. John Nunes was the Technical Monitor for MTL. Additional IIT Research Institute personnel who contributed to this program include S. A. Bortz, J. Morrow, T. Niiro, and S. Moran. Dr. I. M. Daniel, Professor of Mechanics and Mechanical Engineering, IIT, was retained as a consultant to the program.

Accesion For		
NTIS CRA&I	☑	
DTIC TAB	☐	
Unannounced	☐	
Justification		
By		
Distribution /		
Availability Codes		
Dist	Avail and / or Special	
A-1		

QUALITY INSPECTED 3

iii

TABLE OF CONTENTS

LIST OF ILLUSTRATIONS

LIST OF ILLUSTRATIONS (continued)

LIST OF TABLES

1. INTRODUCTION

Advanced metal matrix composite materials possess unique mechanical and physical characteristics which make them desirable for increasingly diverse applications. Composite systems that have received the most attention to date are boron/aluminum, borsic/aluminum, and graphite/aluminum.[1] More recently, with the advent of aluminum oxide (FP) fibers in continuous form, DuPont has introduced systems such as FP/aluminum and FP/magnesium and has developed the basic fabrication (casting) techniques for these composites. However, the fabrication processes need continued improvement, which is directly related to material integrity and performance. It is therefore of great importance to be able to assess the quality of the composites and to reproducibly detect and characterize the most probable flaws that may be introduced or generated during fabrication.

The objective of the program was to apply established nondestructive evaluation (NDE) methods to determine detectability and reproducibility limits of ultrasonic inspections of FP/magnesium composite specimens that were intentionally flawed during fabrication.

One of the most common and widely accepted NDE methods is ultrasonic inspection. Methods and principles for ultrasonic inspection and flaw detection in materials are detailed in the literature.[2-4] Basically, a high frequency (1 to 100 MHz) sound is emitted in periodic bursts from an ultrasonic transducer through a coupling medium into the material being inspected. The resulting attenuated pulse emerging from the specimen is detected by a receiving transducer; the information is electronically processed, and the data are displayed for determination of the presence, size, and location of flaws.

The preferred method of flaw identification is by comparison of pulse information obtained from known flawed and unflawed standard material samples. Appropriate standards, especially in laminated composites, are not always easy to produce and sometimes are not feasible. Alternative pulse processing/ identification techniques for ultrasonic inspection, such as frequency and phase shift analysis, are being developed and implemented.[5-10]

1

Based on the results of a related investigation,[11] the ultrasonic inspections were conducted using ultrasonic transducers of 15 and 20 MHz frequencies operated in the pulse-echo mode. The acoustic couplant between the focused immersion transducers and the specimens was water. The data generated during scanning were recorded on an X-Y plotter as analog C-scans and on oscilloscope photographs of A-scans. Wave attenuation coefficients were determined using two methods. One method used the 20 MHz transducer mentioned above in a water delay line technique. The other method used a 10 MHz shear wave transducer operated in the pulse-echo mode while in intimate contact with the specimen. The acoustic couplant between the contact transducer and the specimen was glycerine. The data generated were recorded on oscilloscope photographs as pulse amplitudes versus reflection number. The amplitudes were then reduced to single attenuation coefficients by solving a set of equations simultaneously.

The wave propagation velocities were determined using an ultrasonic thickness gage. The wave propagation velocity measurements were made by varying the acoustic wave velocity control on the thickness gage until the indicated specimen thickness was identical to that determined by micrometer.

2. EXPERIMENTAL PROCEDURE

2.1 SPECIMENS

The material investigated was ZE41A magnesium alloy reinforced with FP (aluminum oxide) fibers. The specimens were coupons 12.7 cm (5 in.) long x 3.8 cm (1.5 in.) wide x 0.6 cm (0.25 in.) thick with a 0.50 fiber volume ratio. Four coupons of each of five flaw types were machined from 20.3 cm (8 in.) long x 17.8 cm (7 in.) wide x 1.3 cm (0.5 in.) thick casting plates. The casting plates were ultrasonically inspected at IITRI before final machining of the test coupons to determine the orientation and location of the test coupons with respect to the intentional defects and the boundaries of the casting plates. The ultrasonic C-scans of the casting plates are shown in Appendix Figures A1 to A5.

The following FP/Mg coupons with intentional defects were fabricated and evaluated under this contract:

- Type N1: Four FP/Mg coupons with porosity
- Type N2: Four FP/Mg coupons with nonuniform fiber volume ratio
- Type N3: Four FP/Mg coupons with fiber misalignment
- Type N4: Four FP/Mg coupons with fiber fracture
- Type N5: Four FP/Mg coupons with fiber/matrix debonding.

The description of casting plate fabrication procedures, including schematics of the casting plates and test coupons, appears in the Appendix of this report, along with physical property data.

In addition to the 20 new coupons fabricated for this program, seven coupons evaluated by IITRI under AMMRC Contract No. DAAG46-80-C-0070 were returned to IITRI for further nondestructive evaluation. The seven coupons were comprised of one each of six intentional flaw types, and one unflawed coupon as follows:

- Type O1: One FP/Mg coupon with no intentional flaws
- Type O2: One FP/Mg coupon with fiber/matrix debonding
- Type O3: One FP/Mg coupon with porosity

- Type 04: One FP/Mg coupon with fiber misalignment
- Type 05: One FP/Mg coupon with fiber fracture
- Type 06: One FP/Mg coupon with nonuniform fiber distribution
- Type 07: One FP/Mg coupon with matrix fracture.

The above listed coupons were 12.7 cm (5 in.) long x 3.8 cm (1.5 in.) wide x 0.6 cm (0.25 in.) thick, with a 0.50 fiber volume ratio. A description of the defect generation proceaures, including selected coupon schematics, appears in the Appendix of this report.

2.2 NONDESTRUCTIVE EVALUATION METHODS

During the course of the program, each of the 27 test coupons was evaluated using each of the three NDE methods investigated in the program. The three NDE methods applied were:

- Ultrasonic scanning inspections, including A-scans and analog C-scans
- Ultrasonic attenuation, including contact transducer and water delay line
- Wave propagation velocity.

Each of these methods is described in detail in the following sections.

2.2.1 Ultrasonic Scanning

Figure 1 shows the ultrasonic scanning and recording system used on this program. The ultrasonic transducers were driven by a Panametrics Model 5052 UA pulser-receiver, which is capable of operating the transducers in either pulse-echo or through-transmission mode.[2,3] The pulser-receiver was a broadband device that could readily drive transducers in the range of 1 to 20 MHz. It had independent controls for input energy, signal repetition rate, high pass filter gain, and attenuation, all of which shape the transducer output signal. The pulser-receiver provided a time domain output for viewing the RF signal on an oscilloscope or spectrum analyzer. It also had a gated peak output detector, which could operate one axis of an X-Y recorder for plotting the ultrasonic information from the variable peak output signals.

The pulser-receiver was used to drive transducers of 15 and 20 MHz frequency. The transducers were of the focused, immersion type, 1.3 cm (0.5 in.)
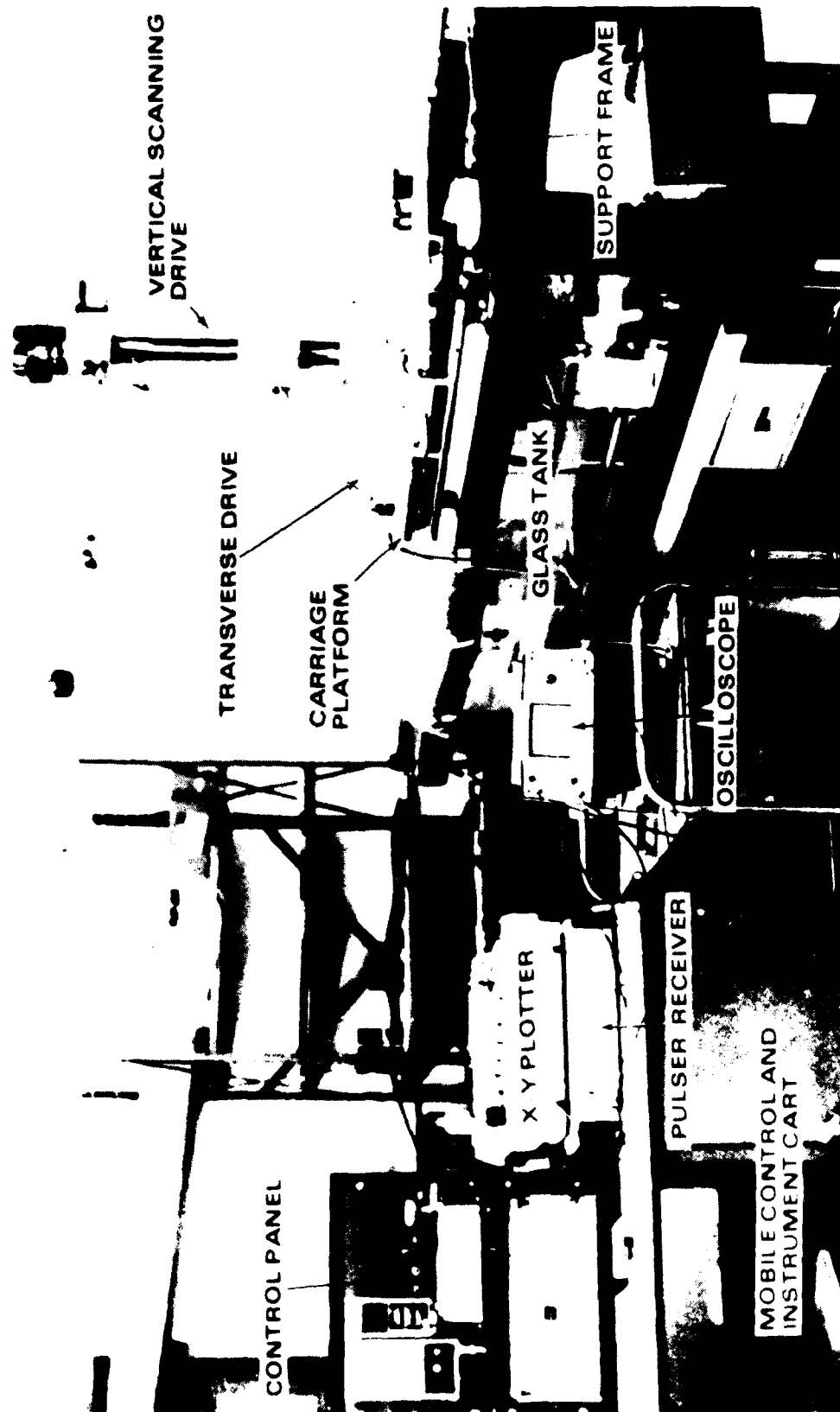
Figure 1. Ultrasonic scanning and recording system for nondestructive flaw detection in composite laminates.

5

in diameter. The requirements for determining the transducer selection were: the results and recommendations in the final report of AMMRC Contract No. DAAG46-80-C-0070,[11] a standoff distance of at least 5.4 cm (2 in.) to clear hardware associated with coupon mounting, high damping and broad bandwidth to provide resolving power for the detection of subsurface flaws, and a small sound-beam cross-section for good definition of flaw boundaries in the plane of the specimen. The nominal focal length in water was 5.1 cm (2 in.). The focal spot size was 1.3 mm (0.05 in.) diameter, which made it possible to outline the boundary of a flaw in the plane of the coupon to within ±0.64 mm (±0.025 in.).

In addition to the transducers and pulser receiver, three pieces of equipment were required to determine specimen integrity. They were an X-Y recorder, an oscilloscope, and an oscilloscope camera. The X-Y plotter was a Hewlett-Packard Model 7044A X-Y recorder. The X and Y control sensitivities ranged from 0.25 mV/cm to 5 V/cm. The C-scan could be smaller, equal to, or larger than the actual specimen up to a size of 25 cm (10 in.) x 38 cm (15 in.). The X-Y recorder could plot either pen-lift or analog C-scans. In the pen-lift mode, the output from the voltage peak detector was channeled through an electronic alarm unit into the pen-lift control of the recorder. The alarm unit was set to trigger the pen-lift whenever the signal amplitude through the peak detector fell below a prescribed level, indicating a flaw; otherwise, the pen stayed in contact with the paper tracing a line. This gave detailed flaw locations in the plane of the specimen with definite outlines of flaw boundaries. The analog mode gives a continuous record of the amplitude of the gated pulse. An analog C-scan is obtained by scanning the specimen with the alarm bypassed. The horizontal and vertical motion of the pen was controlled by signals relayed to the X-Y recorder from displacement transducers mounted on the scanning drive mechanism. The scanning drive mechanism, like the X-Y recorder, was used exclusively for generating C-scans.

The oscilloscope used was a Tektronix Model 445/A2/B2. This was a 50 MHz, dual channel, portable oscilloscope with deflection factors calibrated from 5 mV to 5 V per division. The horizontal deflection system provided stable triggering over the full bandwidth capabilities of the vertical system. The oscilloscope displayed signals processed by the pulser-receiver.

The system shown in Figure 1 consisted of an all-glass immersion tank 45.7 cm (18 in.) wide, 45.7 cm (18 in.) high, and 183 cm (72 in.) long, resting on a support table. The transparent glass tank afforded distortion-free visual observation through the tank sides during specimen and transducer alignment before scanning. A structural steel frame rested on the support table and surrounded the glass tank, which was positioned relative to the frame. The frame supported the mechanical system for transducer motion.

The mechanical system had a scanning carriage platform with three precision screw drives which moved the ultrasonic transducers along three mutually perpendicular axis. The carriage platform was guided along the tank length on steel shafts attached to the support frame. The platform was elevated above the tank and could be positioned at any tank location.

Figure 2 shows the motorized screw drive for vertical motion and the vertical arm holding the ultrasonic transducer at the lower end. The drive was capable of moving the arm in vertical strokes of up to 35.6 cm (14 in.) at rates up to 127 cm/min (50 in./min). The stroke was monitored by a cable-type electromechanical position transducer attached to the vertical drive. Figure 2 also shows the horizontal, transverse screw drive. This was manually operated to locate or focus an ultrasonic transducer before each coupon was scanned.

2.2.2 Ultrasonic Attenuation

A method of specimen inspection complementary to the determination of wave propagation velocity is the calculation of ultrasonic attenuation coefficients. The attenuation results from geometric dispersion due to material heterogeneity (such as the porosity of the Type N1 specimens), geometric attenuation due to internal defects such as fiber fracture (Type N4), fiber debonding (Type N5), and energy dissipation due to viscoelastic or other dissipative natures of the material.

The objective of the attenuation measurements was to correlate, if possible, the calculated attenuation with the condition of the material being evaluated. Since it was important to make the amplitude measurements in a reliable, quantitative, and reproducible manner, a special specimen holder was used. Absolute measurements of attenuation were difficult because the amplitude of a reflected or transmitted pulse depends on both material attenuation

7

DRIVE MOTOR

POSITION TRANSDUCER

CABLE

VERTICAL SCANNING DRIVE

ULTRASONIC TRANSDUCER SCANNING ARM

TUBE SCANNING STEPPER MOTOR

TRANSVERSE DRIVE

COMPOSITE TUBE

TUBE HOLDER
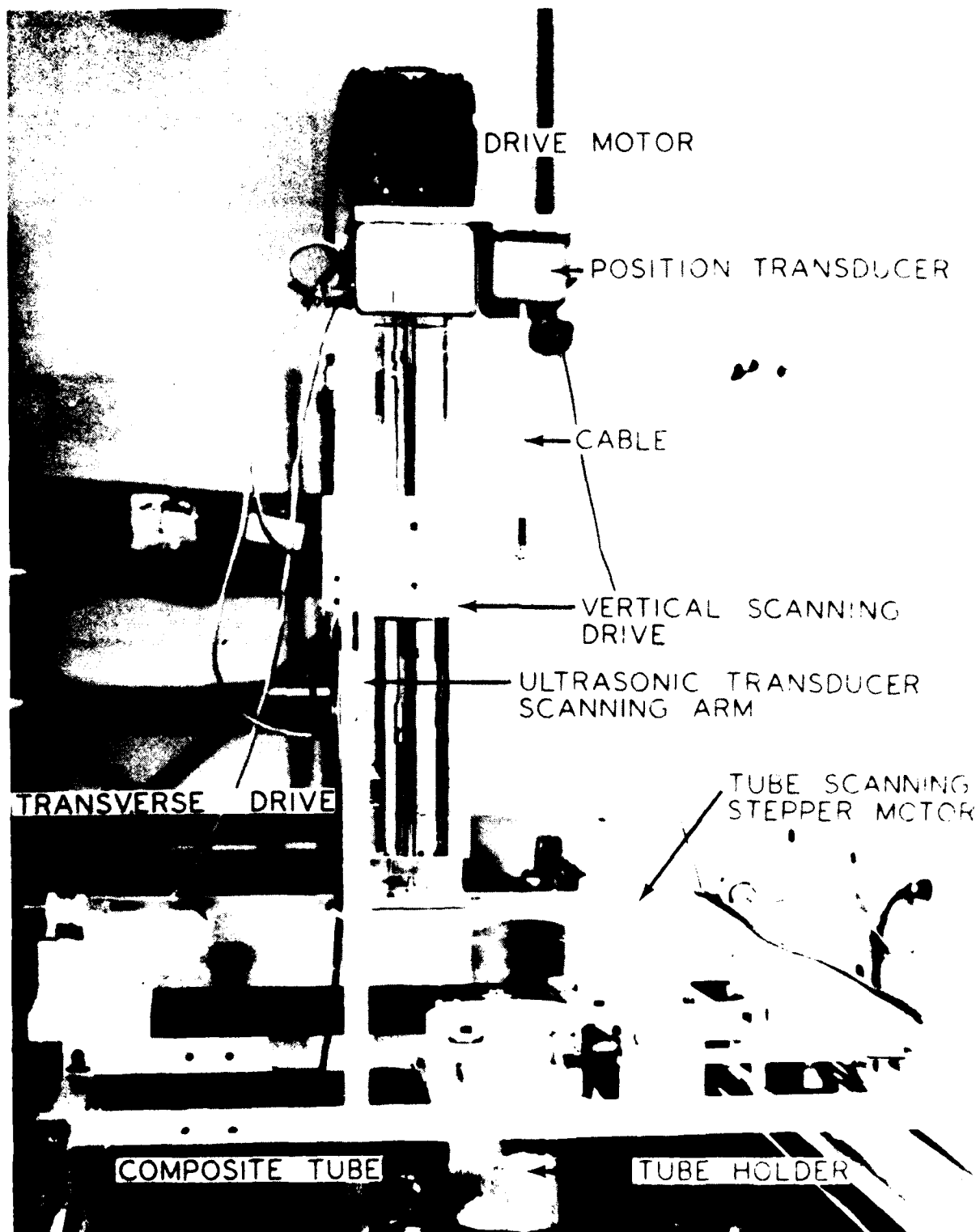
Figure 2. Motorized drive system for vertical motion of transducers.

and the energy dissipation in the couplant between the transducer and the specimen. The specimen holder shown in Figure 3 was designed[11] to minimize ultrasonic wave energy losses associated with the transmission of ultrasound to the water through the back face of the coupon during immersed ultrasonic inspection. The specimen holder had a watertight seal which formed an air pocket adjacent to the back face of the coupon. Since the impedance mismatch was greater between FP/Mg and air than between FP/Mg and water, less wave energy was lost through the back face to the air than would occur if the coupon was totally surrounded by water.

Figure 4 schematically shows the pulses received by the transducer where:

t_2 = travel time in water delay line

t_1 = travel time in specimen

$R_{21} = \dfrac{Z_1 - Z_2}{Z_1 + Z_2}$ reflection coefficent at water/specimen interface

$R_{12} = \dfrac{Z_2 - Z_1}{Z_1 + Z_2}$ reflection coefficient at specimen/water interface

$T_{12} = \dfrac{2Z_2}{Z_1 + Z_2}$ transmission coefficient from specimen to water

$T_{21} = \dfrac{2Z_1}{Z_1 + Z_2}$ transmission coefficient from water to specimen

Z_1, Z_2 = acoustic impedances of specimen and water, respectively (product of material density and wave propagation velocity)

R_{10} = reflection coefficient from dry specimen surface ($\cong 1$)

$10^{\alpha 1}$, $10^{\alpha 2}$ = attenuation per echo for specimen and water, respectively.

Air
Space

Specimen

Watertight seal
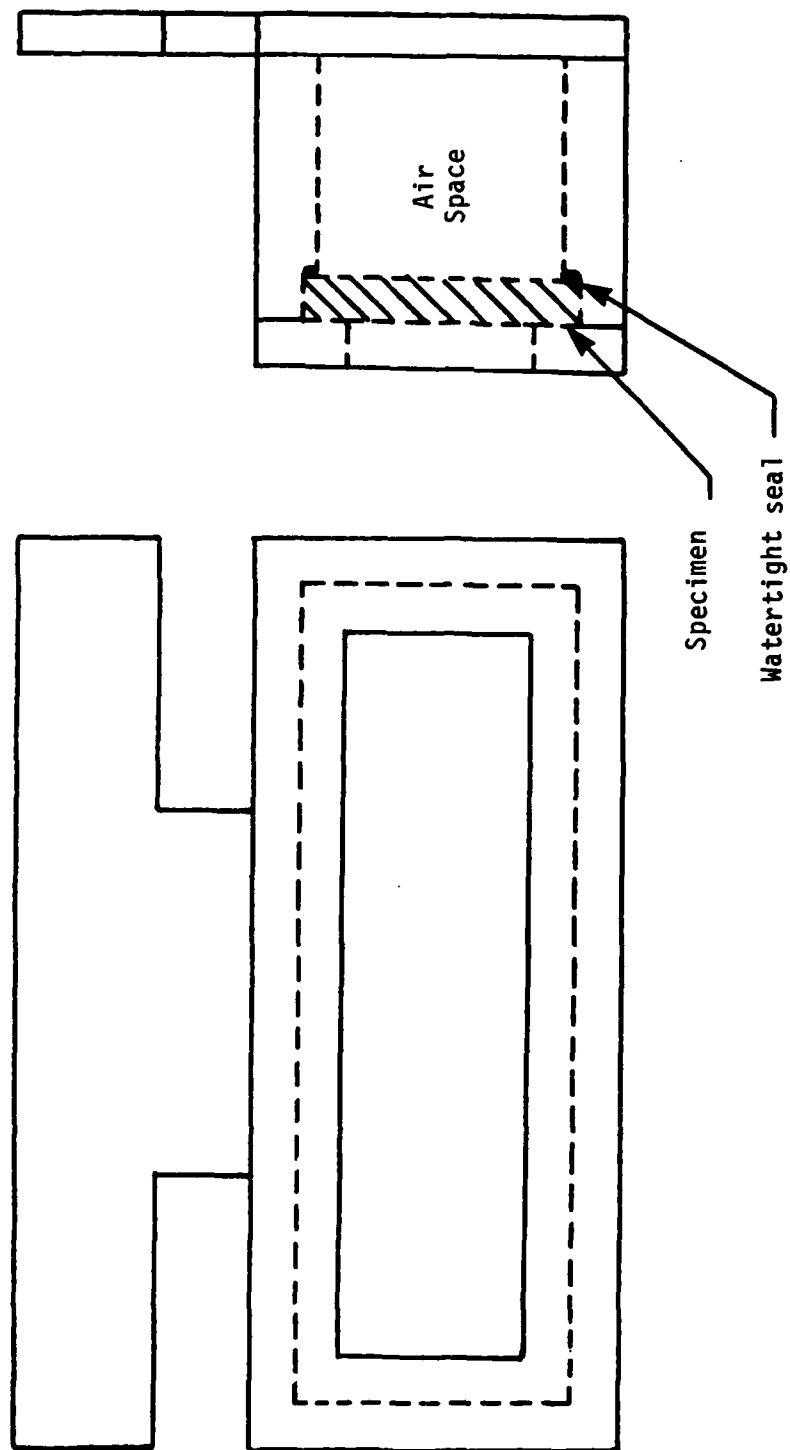
Figure 3. Specimen holder for determination of ultrasonic wave attenuation of FP/Mg specimens.
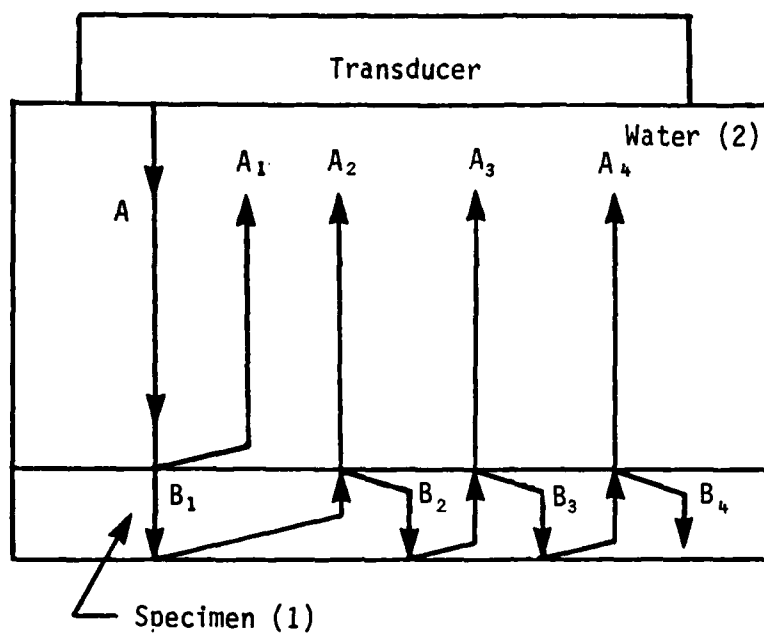
Time After Initial Pulse	Pulse	Magnitude
0	A	A
$2t_2$	A_1	$AR_{21}10^{-\alpha_2}$
$2t_2 + 2t_1$	A_2	$AT_{21}T_{12}R_{10}10^{-\alpha_2-\alpha_1}$
$2t_2 + 4t_1$	A_3	$AT_{21}T_{12}R_{10}^2R_{12}10^{-\alpha_2 2-\alpha_1}$
$2t_2 + 6t_1$	A_4	$AT_{21}T_{12}R_{10}^3R_{12}^2 10^{-\alpha_2-3\alpha_1}$

Figure 4. Schematic of echoes received by transducer.

11

The attenuation of the specimen material in decibels per unit length is then expressed as:

$$\alpha = \frac{20}{2d_1} \alpha_1 = \frac{10}{d_1} \alpha_1$$

where d_1 is the specimen thickness.

Taking the logarithms of the amplitude ratios of the various echoes shown in Figure 4 and setting $R_{10} = 1$, we obtain:

$$\log \frac{A_1}{A_2} = \alpha_1 + \log |R_{21}| - \log (T_{12} T_{21})$$

$$\log \frac{A_1}{A_3} = 2\alpha_1 + \log |\frac{R_{21}}{R_{12}}| - \log (T_{12} T_{21})$$

$$\log \frac{A_1}{A_4} = 3\alpha_1 + \log |R_{21}| - 2 \log |R_{12}| - \log (T_{12} T_{21})$$

The equations above can be simplified by noting that:

$$|R_{21}| = |R_{12}| = R$$

$$T_{12} T_{21} = 1 - R^2$$

Then, any two of the equations above can be solved for R and α_1, the only two unknowns.

The acoustic impedance for water is considered constant at $Z_2 = 1.5 \times 10^6$ kg/m^{2}s. The acoustic impedance for each specimen was calculated using measuring density and wave propagation velocity values.

Figure 5 shows a typical ultrasonic measurement record (A-scan) and corresponding amplitudes. The amplitudes were determined using a digital voltmeter, variable voltage power supply, and a dual beam oscilloscope. The amplitude voltages were determined by using one beam of the oscilloscope as a

12
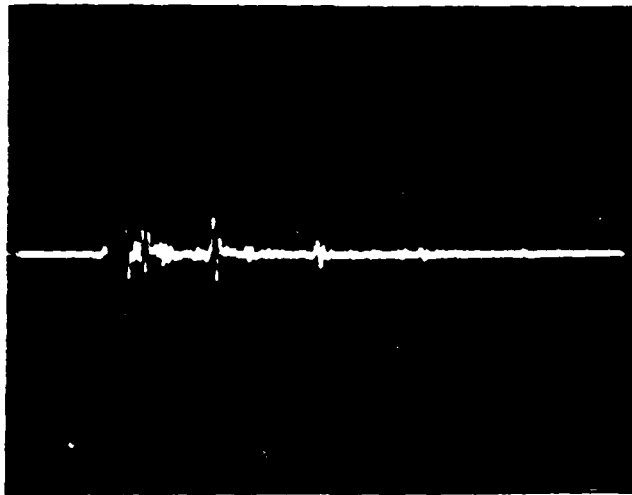
Inspection Location	Amplitude (Volts)	Time $(10^{-6}$ s)
1	1.90	0.00
2	0.49	1.75
3	0.10	3.50
4	0.05	5.25

Figure 5. Ultrasonic attenuation record for ᵀP/Mg specimen at an unflawed location.

cursor and moving it with the power supply to pass through the peak of each pulse. The voltages were recorded on the digital voltmeter.

A second method of determining the ultrasonic attenuation used a 10 MHz, shear wave, contact transducer operated in the pulse-echo mode. Ultrasonic attenuation records similar to that shown in Figure 5 were generated and reduced using the equations previously presented. Propylene glycol (Z_2 = 2.5 x 10^6 kg/m^{2}s) was used as the acoustic couplant.

2.2.3 Wave Propagation Velocity

The wave propagation velocities were determined using a Panametrics Model 5221 ultrasonic thickness gage. This could be used to determine wave propagation velocity, since any deviation between the thickness measured

ultrasonically and that measured with a micrometer is related to the difference between the assumed and actual wave propagation velocity.

The longitudinal wave propagation velocities along the three principal material axes of an anisotropic material are given by:

$$C_{11} = \sqrt{\frac{Q_{11}}{\rho}}$$

$$C_{22} = \sqrt{\frac{Q_{22}}{\rho}}$$

$$C_{33} = \sqrt{\frac{Q_{33}}{\rho}}$$

where Q_{ij} are stiffnesses and ρ is the material density. Any change in propagation velocity is related to changes in modulus and/or density. For thin composite plates, two of the above equations are simplified to:

$$C_{11} = \sqrt{\frac{Q_{11}}{\rho}} = \sqrt{\frac{E_{11}}{\rho(1 - \nu_{12}\nu_{21})}}$$

$$C_{22} = \sqrt{\frac{Q_{22}}{\rho}} = \sqrt{\frac{E_{22}}{\rho(1 - \nu_{12}\nu_{21})}}$$

where subscripts 1 and 2 denote parallel and transverse to the fiber directions, respectively, and ν is Poisson's ratio. Subscript 3 denotes the normal-to-the-plate direction. For the FP/Mg specimens used in this program, with a 0.50 fiber volume ratio, the following properties:[12]

$$E_{11} = 207 \text{ GPa } (30 \times 10^6 \text{ psi})$$

$$E_{22} = 103 \text{ GPa } (15 \times 10^6 \text{ psi})$$

$$\nu_{12} = 0.28$$

$$\nu_{21} = 0.14$$

$$\rho = 2.85 \text{ kg/m}^3$$

14

were used to compute:

$$C_{11} = 8,690 \text{ ms}^{-1} \ (342,125 \text{ in./s})$$

$$C_{22} = 6,145 \text{ ms}^{-1} \ (241,930 \text{ in./s})$$

An approximate velocity across the thickness is:

$$C_{33} = 6,400 \text{ ms}^{-1} \ (251,840 \text{ in./s})$$

This then implies that any major deviation of the wave propagation velocity, as indicated by the ultrasonic thickness gage and the C_{33} value shown above, can be attributed to variations in modulus and/or density. A change in modulus could be due to fiber debonding (Type N5) or fiber fracture (Type N4). A change in density could be due to porosity (Type N1) or a nonuniform fiber volume ratio (Type N2).

2.3 MECHANICAL TESTING

2.3.1 Specimen Selection

The coupons chosen for fabrication of destructive test specimens consisted of the unflawed coupon, 01-3, from the previous contract (No. DAAG46-80-C-0070), and representative coupons from each of the five flaw types from the present contract. The unflawed coupon, 01-3, was machined into three 0° tensile specimens consuming all of the parent coupon.

The following test specimens were machined from the complement of twenty coupons fabricated for the subject contract: from the Type 1 coupons with porosity, five 90° three-point bend specimens were tested across the fiber axis; and five 90° three-point bend specimens were tested parallel to the fiber axis. The bend specimens were nominally 2.54 mm (0.10 in.) x 6.35 mm (0.25 in.) x 38.10 mm (1.50 in.) from both defective and defect-free areas of the parent coupon. From the Type 2 coupons with nonuniform fiber volume ratio, five 0° tensile specimens were machined. From the Type 3 coupons with fiber misalignment, three 0° tensile specimens with ±10° off-axis fibers and three 0° tensile specimens with ±20° off-axis fibers were machined. From the Type 4 coupons with fiber fracture, three 0° tensile specimens with "butted together" fiber fracture and three 0° tensile specimens with 2.54 mm (0.10 in.) gap fiber fracture were machined. From the Type 5 coupons with fiber/

matrix debonding, six 0° three-point bend specimens from the same parent coupon were machined. Four of the six specimens were from defective areas and two of the six were from defect-free areas. In addition to the bend specimens from the Type 5 coupons, two 0° tensile specimens were machined from another Type 5 parent coupon.

2.3.1.1 Flexure Specimens

The specific coupons for specimen machining were chosen to include the intentional flaw type within the gage section of the specimen. In the case of the three-point bend specimens, the width of the parent coupon dictated the 38.1 mm (1.5 in.) length of the bend specimen. Final specimen locations were based on the indicated flaw locations in the parent coupons, as determined by the results of the optimized 20 MHz C-scans.

Parent coupon N1-3, Type 1 porosity, was initially chosen for machining the ten required 90° three-point bend specimens. The bend specimen locations, N1-3-1 through N1-3-10, are shown in Figure 6. Specimens N1-3-1 through N1-3-6 were machined consecutively from the left (flawed) end of the parent coupon, which had an indicated area of uniform porosity extending approximately 18 mm (0.71 in.) in from the left edge. Unflawed specimens N1-3-7 through N1-3-10 were machined consecutively from the right end of parent coupon N1-3. The specimens were rough cut approximately 0.5 mm (0.020 in.) over final dimensions with a 0.5 mm (0.020 in.) wide diamond saw blade, and the sides were ground parallel to the final nominal width of 2.54 mm (0.10 in.).

Upon initiation of the 90° three-point bending tests of specimens from coupon N1-3, failure loads for the first specimens, N1-3-1 and N1-3-2, were noted to be an order of magnitude lower than calculated. Further visual examination of the remaining specimens from parent coupon N1-3 revealed the presence of a tight crack in the parent coupon and in all six of the "flawed" bending specimens. The crack extended approximately 75% through the 6.35 mm (0.25 in.) thickness of the parent coupon. Upon examination, a portion of the unflawed remainder of the parent coupon adjacent to the area from which the flawed specimens were removed also exhibited this crack. The crack was undetected by the ultrasonic scan series used to determine area of porosity. The first three specimens (N1-3-1, N1-3-2, and N1-3-3) were oriented and loaded perpendicular to the fiber direction, with the 6.35 mm (0.25 in.)
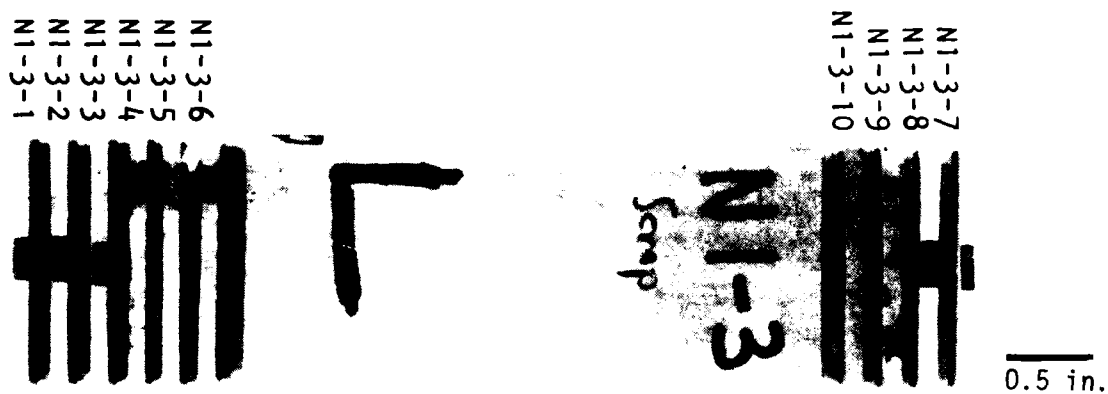
16

Figure 6.   90° 3-point bend specimen locations
from parent coupon N1-3 (porosity).

Figure 7.   90° 3-point bend specimen No. N1-3-3 from the flawed
(porous) area of parent coupon N1-3 showing the vertical
crack 12.7 mm (0.5 in.) from the right end of the specimen.

dimension as the beam depth and the front surface of the parent coupon as the tensile surface of the bend specimen. This surface contained the opening of the crack approximately 12.7 mm (0.5 in.) from the edge of the bend specimen (see Figure 7).

Because of the crack present in the flawed specimens of coupon N1-3, a different Type 1 porosity coupon, N1-4, was chosen for ten 90° three-point bend specimens. Coupon N1-4 had an area of indicated porosity at the right end of the coupon approximately 22 mm (0.866 in.) wide and relatively uniform in distribution. Four unflawed specimens (N1-4-1, N1-4-2, N1-4-3, and N1-4-4) were removed from the left side and six flawed specimens (N1-4-5, N1-4-6, N1-4-7, N1-4-8, N1-4-9, and N1-4-10) were removed from the right (porous) side of the parent coupon (N1-4). The specimens were machined consecutively from the free edges of the parent coupon approximately 0.5 mm (0.020 in.) over final dimension to allow for grinding the sides parallel and with a 0.5 mm (0.020 in.) notch between each specimen. The relative locations of the ten 90° bend specimens are shown in Figure 8. Two of the unflawed specimens and three of the flawed specimens were tested in bending with load applied perpendicular to the fiber direction. The two remaining unflawed specimens and the three remaining flawed specimens were tested in bending with the load applied parallel to the fiber direction.

Parent coupon N5-3, Type 5 fiber/matrix debonding, was chosen to provide the six required 0° three-point bend specimens. The bend specimen locations are shown in Figure 9. All bend specimens were removed from the center 38.1 mm (1.5 in.) of the parent coupon. Specimen N5-3-1, unflawed, was removed from the top edge of the parent coupon. Flawed specimens, N5-3-2 and N5-3-3, were cut consecutively, with the top edge of specimen N5-3-2 being located 6.35 mm (0.25 in.) down from the top edge of the parent coupon. Unflawed specimen, N5-3-4, was cut from the center of the parent coupon with the top edge located 19.05 mm (0.75 in.) down from the top edge of the parent coupon. The remaining two flawed specimens, N5-3-5 and N5-3-6, were cut consecutively from the center of the parent coupon with the top edge of specimen N5-3-5 located 28.58 mm (1.125 in.) down from the top edge of the parent coupon.

Unflawed

Porosity

0.5 in.

Figure 8. 90° 3-point bend flawed and unflawed specimen locations from parent coupon N1-4.

0.5 in.

Figure 9. 0° 3-point bend specimen locations from parent coupon N5-3 (fiber/matrix debonding).

O1-3-1   O1-3-1

O1-3-2   O1-3-2

O1-3-3   O1-3-3

Figure 10. 0° tensile specimen locations from parent coupon O1-3 (unflawed).

19

2.3.1.2 Tensile Specimens

The parent coupons chosen for machining of the tensile specimens were chosen such that the intentional flaw type would be located within the gage section of the tensile specimen.

Unflawed coupon 01-3 was machined into three 0° tensile specimens consuming the entire coupon. Specimen 01-3-1 was located in the top one-third, specimen 01-3-2 the center third, and specimen 01-3-3 was located in the bottom third of the parent coupon. Figure 10 shows the relative orientation of the tensile specimens from coupon 01-3.

Nonuniform fiber volume ratio coupons N2-2 and N2-3 were machined into six 0° tensile specimens consuming both coupons. Specimen N2-2-1 was located in the top one-third of the parent coupon (N2-2). Specimen N2-2-2 was located in the center of the parent coupon (N2-2) and was held in reserve as a spare specimen. Specimen N2-2-3 was located in the bottom third of the parent coupon (N2-2). Figure 11 shows the relative orientation of the three tensile specimens from coupon N2-2. Figure 12 shows the relative orientation of the three tensile specimens from coupon N2-3 (similar to N2-2). The interface of the 35% and the 55% fiber volume ratios for all six of the Type 2 tensile specimens was contained within the gage section.

Coupon N3-1, with internal ±10° off-axis plies, was machined into three 0° tensile specimens consuming the entire coupon. Figure 13 shows the relative orientation of the three tensile specimens from coupon N3-1. Coupon N3-3, with internal ±20° off-axis plies, was machined into three 0° tensile specimens consuming the entire coupon. The specimen orientation is shown in Figure 14.

Coupon N4-1, with a "butted" internal fiber fracture, one ply thick, was machined into three shortened 0° tensile specimens. The overall length of the specimens was 88.9 mm (3.5 in.). The specimens were removed from the left side of coupon N4-1 leaving a 38.1 mm (1.5 in.) wide portion of the right side of the parent coupon. The shortened specimen geometry was necessary to ensure that the indicated flaw would be located within the gage section of the specimen. The flaw position, as indicated by the 20 MHz C-scan, was approximately 43.7 mm (1.72 in.) from the left end of the parent coupon. Using the full 127 mm (5.0 in.) specimen geometry would place this flaw in the transition section

Figure 11. 0° tensile specimen locations from parent coupon N2-2
(nonuniform fiber volume ratio).
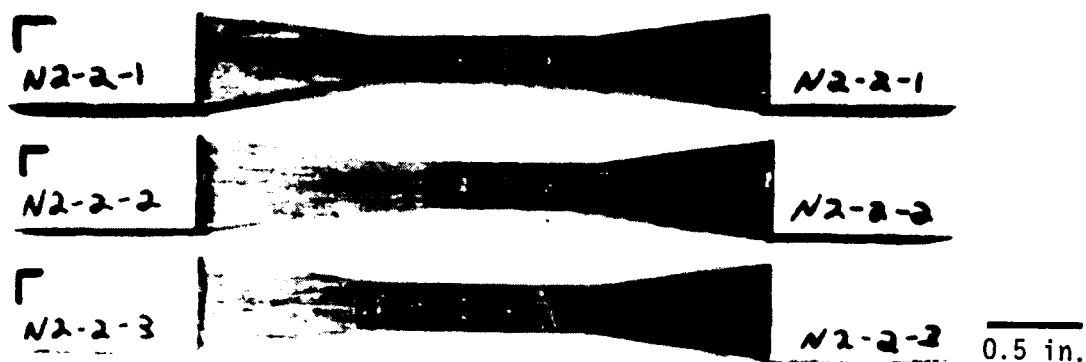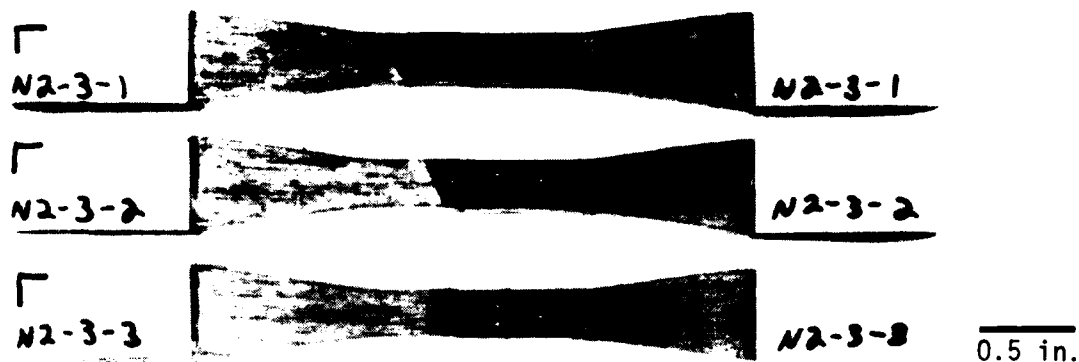

Figure 12. 0° tensile specimen locations from parent coupon N2-3
(nonuniform fiber volume ratio).
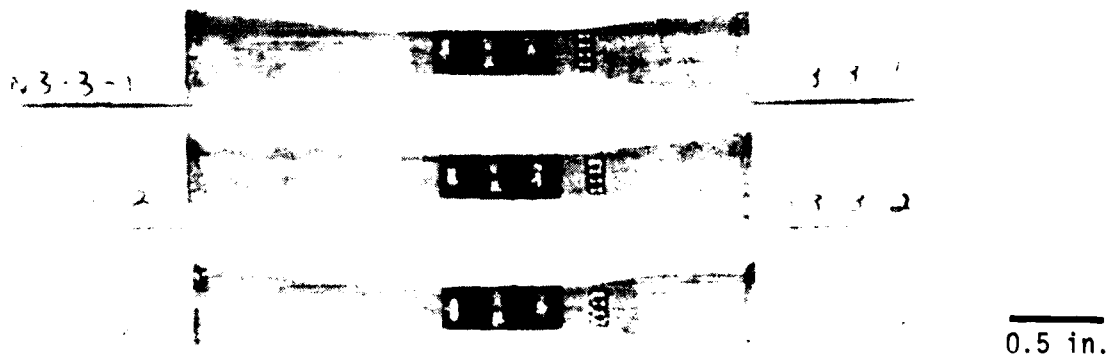

Figure 13. 0° tensile specimen locations from parent coupon N3-3
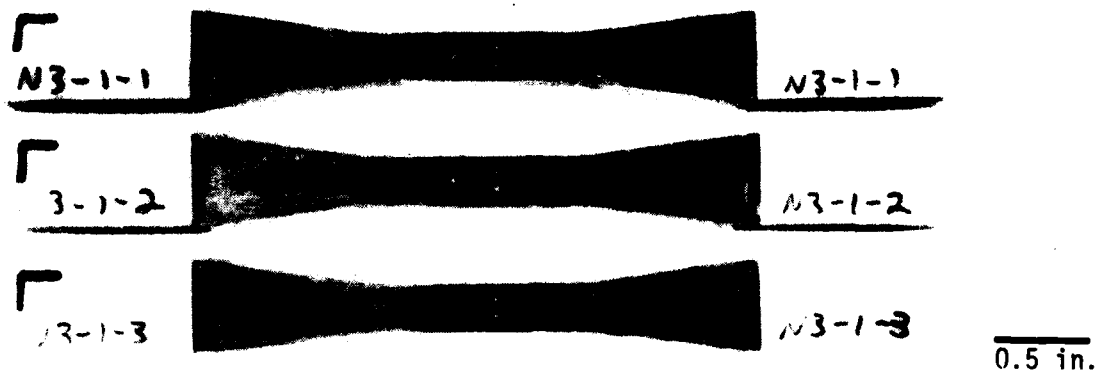(+10° off-axis fibers).

21

Figure 14. *0° tensile specimen locations from parent coupon N3-1 (±20° off-axis fibers).*
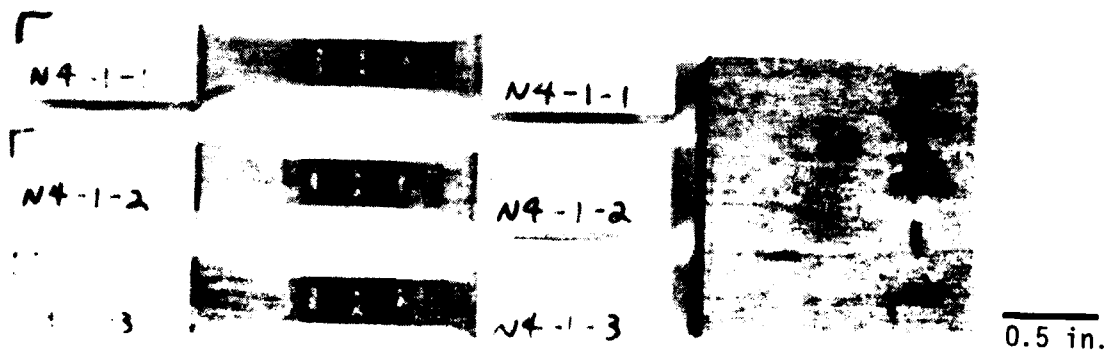

Figure 15. *0° tensile specimen locations from parent coupon N4-1 (butted fiber fracture).*

between the gage section and tab section. Specimen N4-1-1 was located in the top one-third of the parent coupon (N4-1). Specimen N4-1-2 was located in the center and specimen N4-1-3 was located in the bottom third of the parent coupon (N4-1). Figure 15 shows the relative orientation of the three specimens.

Coupon N4-3, with a 2.54 mm (0.10 in.) wide internal fiber fracture, one ply thick, also supplied three 0° tensile specimens. Specimen N4-3-1 was located in the top one-third, specimen N4-3-2 was located in the center third, and specimen N4-3-3 was located in the bottom third of the parent coupon (N4-3). Figure 16 shows the relative orientation of the three tensile specimens from coupon N4-3. The intentional flaw of all three of the gap fiber fracture specimens from coupon N4-3 was within the gage section.

Coupon N5-1, Type 5 fiber/matrix debonding, was machined into two 0° tensile specimens containing defects in the gage section. Specimen N5-1-1 was located in the top portion of the parent coupon 3.17 mm (0.125 in.) down from the top edge. Specimen N5-1-2 was removed from the bottom third of the parent coupon (N5-1). Figure 17 shows the relative orientation of the two tensile specimens from coupon N5-1.

2.3.2 Specimen Preparation and Testing Procedures

The 90° three-point bend specimens were removed from their parent coupons with a diamond saw blade. The as-cut specimens were approximately 0.5 mm (0.020 in.) over the nominal width of 2.54 mm (0.10 in.) to allow for grinding the cut sides parallel. The narrow dimension of the specimens was produced by grinding the saw-cut sides parallel. This produced a rectangular beam of nominal dimensions 2.54 mm (0.10 in.) x 6.35 mm (0.25 in.) x 38.10 mm (1.50 in.) long. The 90° bend specimens tested perpendicular to the fiber direction were oriented such that their width was 2.54 mm (0.10 in.) and their depth was 6.35 mm (0.25 in.). The 90° bend specimens tested parallel to the fiber direction were oriented such that their width was 6.35 mm (0.25 in.) and their depth was 2.54 mm (0.10 in.). The length of the bottom span was 25.4 mm (1.00 in.). All of the 90° three-point bend specimens were oriented such that the top face of the parent coupon was the tensile surface in the bend tests for the specimens loaded perpendicular to the fiber direction. The orientations are illustrated in the following sketches.
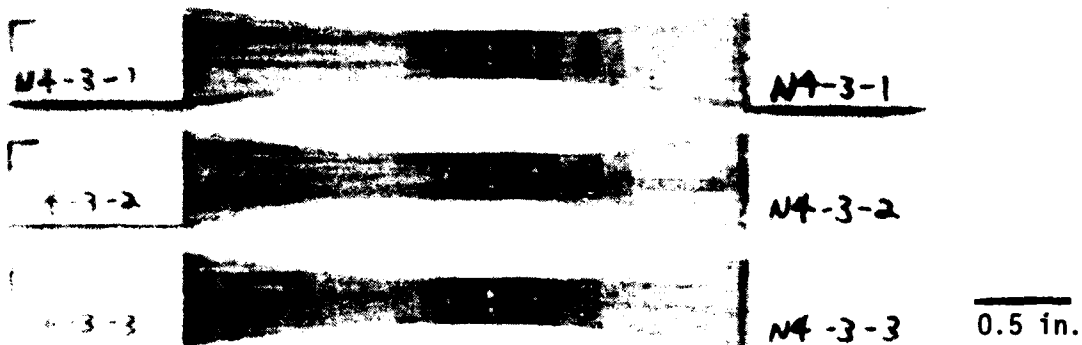
Figure 16. *0° tensile specimen locations from parent coupon N4-3 (1/10 in. gap fiber fracture).*

Figure 17. *0° tensile specimen locations from parent coupon N5-1 (fiber/matrix debonding).*

90° 3-point bend specimens, loaded perpendicular to fiber direction:

Fiber Axis

P

d = 6.35 mm
(0.25 in.)

Top Surface of
Parent Coupon

ℓ = 38.10 mm
(1.50 in.)

w = 2.54 mm
(0.10 in.)
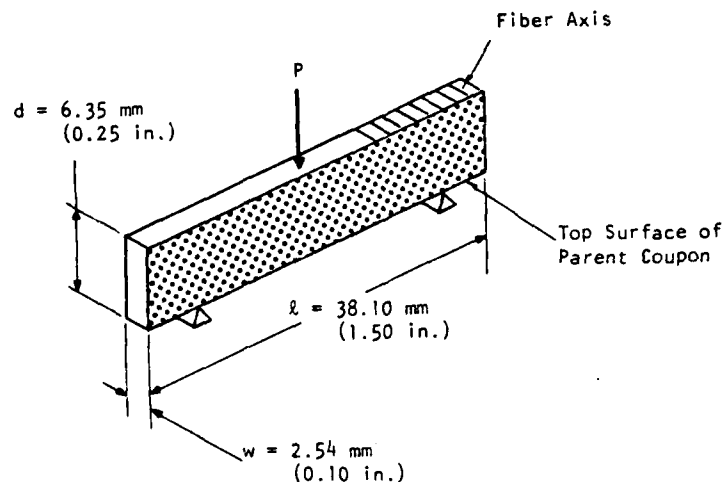
90° 3-point bend specimens, loaded parallel to fiber direction:

P

d = 2.54 mm
(0.10 in.)

Fiber Axis

ℓ = 38.10 mm
(1.50 in.)

w = 6.35 mm
(0.25 in.)
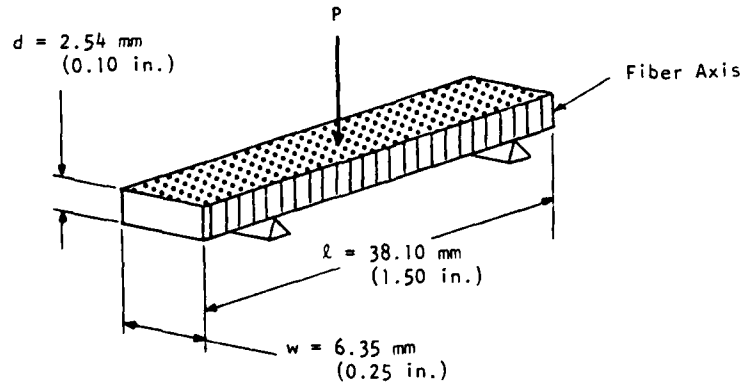
The 0° three-point bend specimens from coupon N5-3 were removed with the length of the bend specimen parallel to the fiber direction. The specimens were rough cut with a diamond saw blade approximately 0.5 mm (0.020 in.) over the nominal width of 2.54 mm (0.10 in.) and were ground parallel to the final width. The depth of the specimens was equal to the thickness of the parent coupon, nominally 6.35 mm (0.25 in.) thick. The length of the specimens was

38.10 mm (1.50 in.). The bottom span for the specimens was 25.4 mm (1.00 in.). All six of the 0° three-point bend specimens were oriented such that the front face of the parent coupon was the tensile surface in the bend tests.

The 0° tensile specimens were removed from the parent coupons by slicing the parent coupon into thirds along its length of 127 mm (5.0 in.) using electric discharge machining (EDM). This method was used rather than diamond sawing in order to remove as little material as possible between specimens. EDM was used to rough out the approximate specimen geometry in both the gage section and the transition section between the tab area and gage section. Final tensile specimen geometry was obtained by diamond wheel grinding to the specimen profile as recommended by ASTM D-3552, "Standard Test Method for Tensile Properties of Fiber-Reinforced Metal Matrix Composites."[13] All of the 0° tensile specimens, except those from coupon N4-1, were machined to the specifications of ASTM D-3552 flat tension specimen design "A" with the following modification: specimen design "A" calls for a tab width, W_t, of 2T + W_G, where T = specimen thickness 6.35 mm (0.25 in.), and W_G = width of the gage section 6.35 mm (0.25 in.). This would require a tab width of 19.05 mm (0.75 in.). The 38.10 mm (1.50 in.) width of the parent coupons limited the tab width of the tensile specimens to less than 12.70 (0.5 in.). Flat tension specimen geometry for design "A" is shown in Figure 18a.

Because of the indicated location of the intentional flaw in coupon N4-1, a shortened tension specimen geometry was used. A modified version of ASTM D-3552 flat tension specimen design "E" was used for the tension specimens from coupon N4-1. The modification consisted of narrowing the tab width, W_t, in order to obtain three tensile specimens from the parent coupon and lengthening the gripping area, L_t, by 6.35 mm (0.25 in.) to compensate for the narrowed width. The necked-in gage section for the 0° tensile specimens N4-1-1, N4-1-2, and N4-1-3, was formed by diamond wheel grinding to the final profile. The modified flat tension specimen geometry for design "E" is shown in Figure 18b.

Fiberglass/epoxy tabs were bonded to the tab areas of all the 0° tensile specimens. The tab dimensions were nominally 25.4 mm (1.00 in.) x 12.7 mm (0.5 in.) x 1.75 mm (0.070 in.) thick.

Surface preparation procedures, prior to bonding the strain gages to the specimens, were the same for both the three-point bend specimens and the
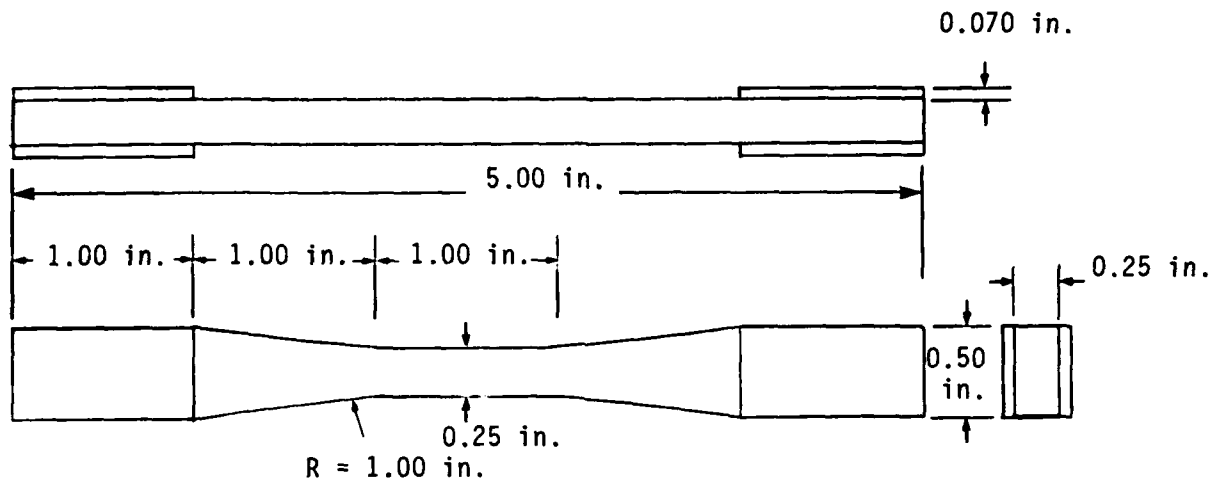
(a) Design A configuration used for 01-3, N2-2, N2-3, N3-1, N3-3, N4-3, and N5-1 tensile specimens.
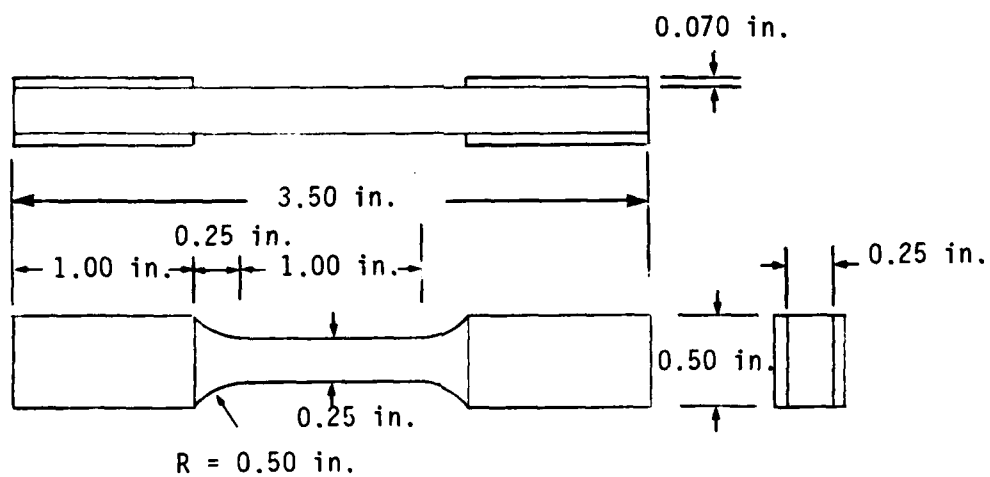
(ʋ) Design E specimen configuration used for N4-1 tensile specimens

Figure 18. Tensile specimen geometries recommended in ASTM D-3552.[13]

tensile specimens. Surface preparation consisted of scraping the gage location area with a sharp knife edge, followed by degreasing with a cotton swab moistened with Chlorothene degreaser. After degreasing, the gage location area was wet sanded with 220 grit abrasive paper moistened with Micro Measurements M-Prep-B Neutralizer, and swabbed with neutralizer until a clean dry swab would not show any discoloration.

The three-point bend specimens were instrumented with a single strain gage (Micro Measurements Type EA-15-062DF-120) at the center of the tensile face to monitor the tensile strains. The strain gage was bonded to the specimen with M-bond Type 200, methyl-2-cyanoacrylate adhesive. After lead wires were soldered to the gage, the gage assembly was coated with M-Coat-A, air-drying polyurethane, for both moisture and mechanical protection. Specimens were tested in an Instron testing machine at a crosshead rate of 0.008 cm/min (0.02 in./min). The applied load and tensile strain were recorded at several intervals to failure. Figure 19 shows the three-point bend test fixture set up in the Instron test machine with a bend specimen in place.

The 0° tensile specimens were instrumented with a two-gage rosette (Micro Measurements Type EA-15-125VB-120) on both the front surface of the gage area and the back surface of the gage area. Each two-gage rosette consists of a longitudinal gage and a transverse gage. The rosette was located such that the longitudinal gage was positioned at the center of the gage section. The longitudinal (0°) gages monitored axial tensile strains in the specimen. The opposite side positioning of the longitudinal gages also monitored the presence of any bending which may have occurred during axial loading. The transverse (90°) gages were used to monitor the transverse contraction of the gage section due to Poisson's strain of the material. The two types of gages permitted the calculation of the elastic modulus, E_{11}, for the material and Poisson's ratio, ν_{12}, as well as strain-to-failure. The strain gages were bonded to the tensile specimens after surface preparation with M-bond Type 200, methyl-2-cyanoacrylate adhesive. After lead wires were soldered onto the gages, the entire gage assemblies were coated with M-coat-A, air-drying polyurethane, for both moisture and mechanical protection. The tensile specimens were tested to failure in an Instron testing machine at a crosshead extension rate of 0.008 cm/min (0.02 in./min). The applied load and corresponding strains were recorded at several intervals to failure. Figure 20 shows the
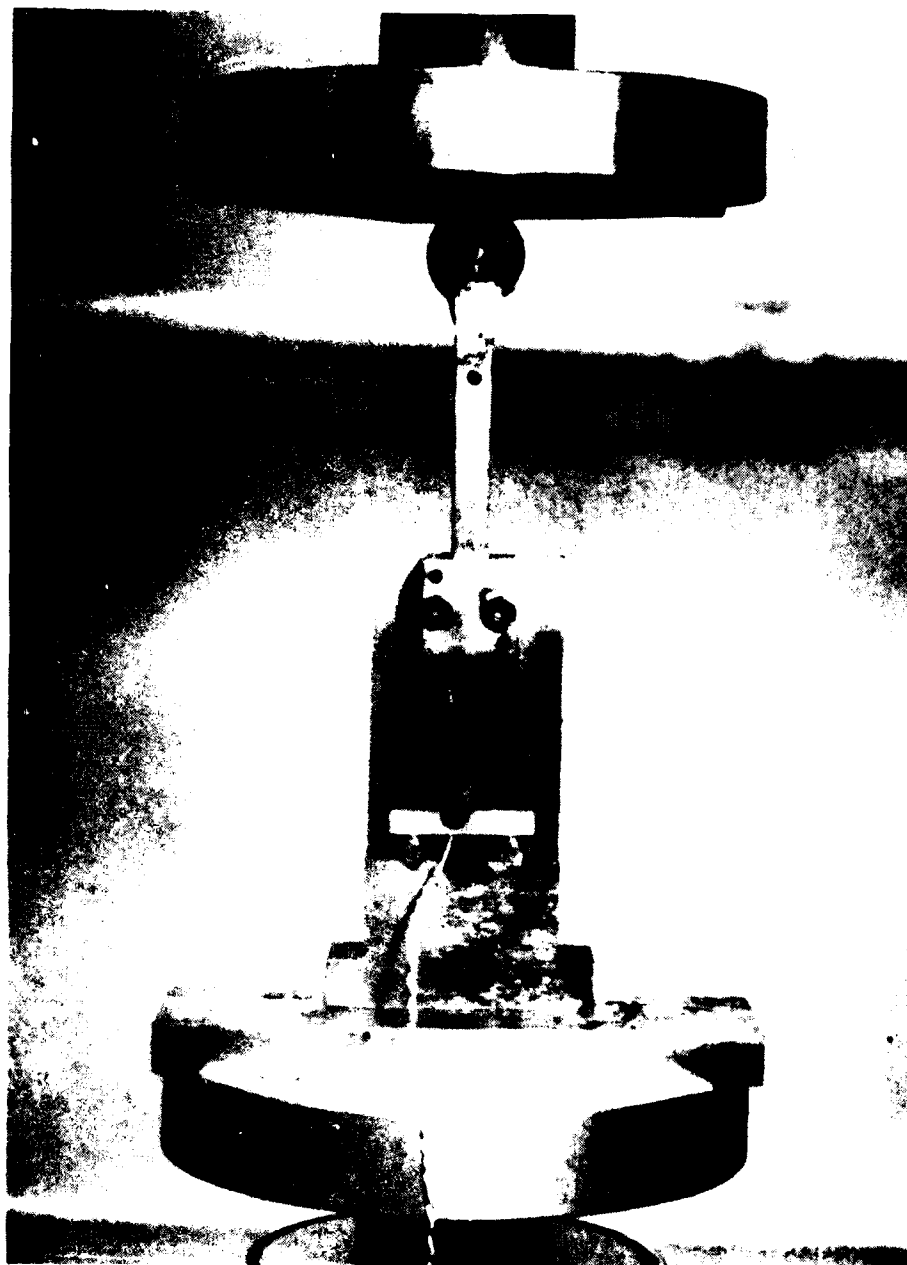
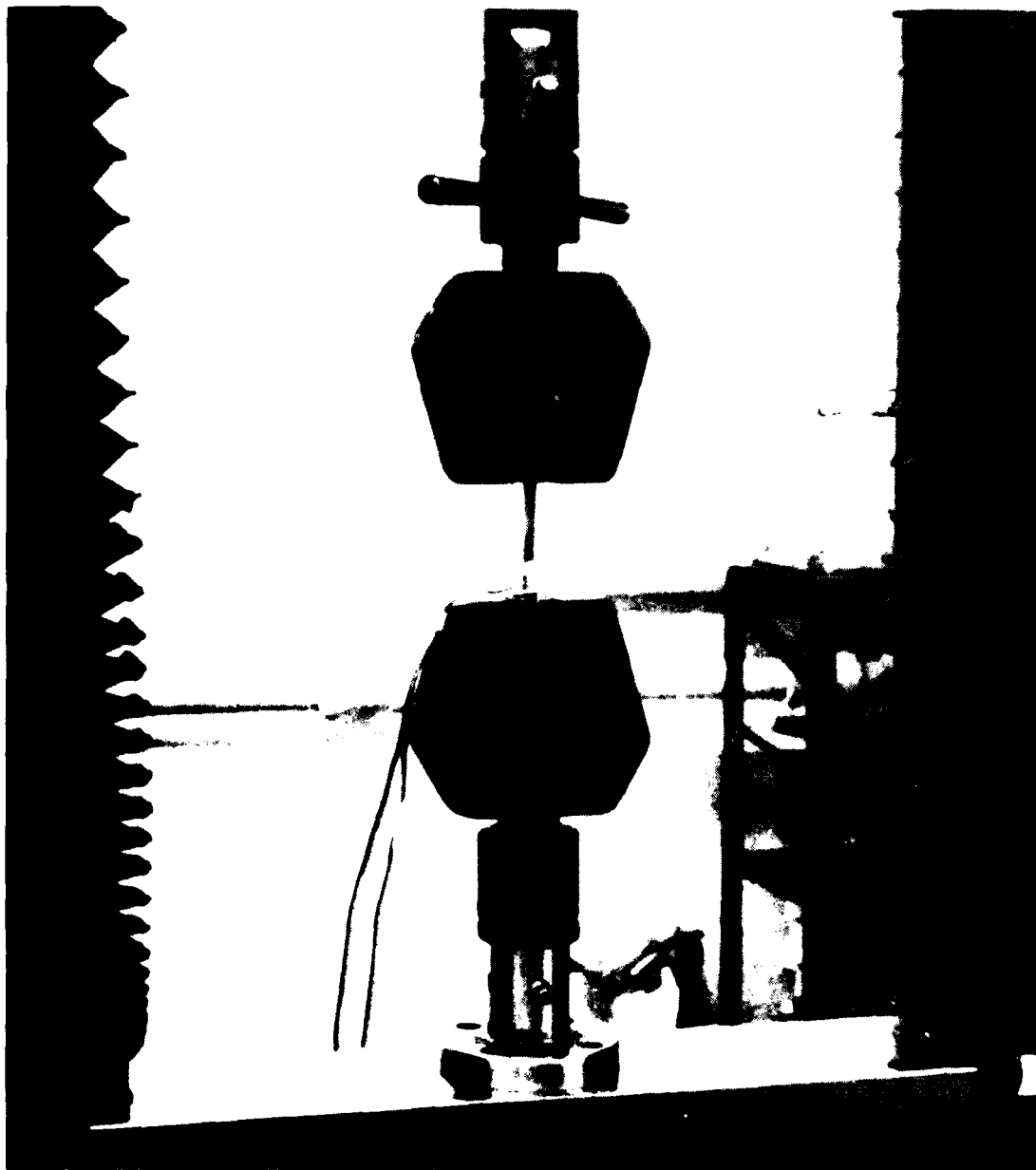*Figure 19. 4-point flexure fixture with specimen in place in an Instron test machine.*

*Figure 20. An instrumented tensile specimen illustrating the gripping
arrangement for tensile testing in an Instron test machine.*

instrumented tensile specimen as set up in the Instron test machine. Load and strain were monitored with a Kaye datalogger.

2.4 MICROSCOPY

Standard optical microscopy, metallographic, and SEM techniques were used on test bars to validate the nondestructive inspection results. Metallographic samples were removed from bulk material such that flaw orientation was maintained and traceable throughout sample preparation. Samples were mounted, ground, and polished with precautions taken to avoid distortion of the intentional flaw, e.g., from fiber "pull-out" or fracture, or from matrix plastic deformation. The polishing procedure consisted of grinding on 240, 360, and 600 grit silicon carbide papers using kerosene or alcohol as lubricants, followed by polishing with 9, 6, and 1 μm diamond paste on Buehler napped microcloth with kerosene. A final polish with 0.5 μm alumina slurry completed the procedure. The microstructure was studied by reflected light microscopy.

The fracture surface of each mechanically tested sample was observed to determine the type and size of the flaw causing fracture. Microstructural issues of interest included the fiber/matrix interface, delaminations, fiber breakage, porosity, and fiber size and distribution.

3. RESULTS

3.1 NONDESTRUCTIVE EVALUATION

3.1.1 Ultrasonic Scanning

There were two objectives to be met during this phase of the program.
The first was to determine the detectability limits of ultrasonic scanning in
defining the presence and geometry of intentionally generated material de-
fects. The second was to determine the reproducibility limits of ultrasonic
scanning by the repeated inspection of intentionally flawed coupons.

To expedite the ultrasonic inspection phase, ultrasonic inspection was
considered to be a basic research tool and not a point for primary investiga-
tion within the project. The basic parameters of the ultrasonic inspection
(transducer type, operating mode, frequency, recording mode, etc.) were se-
lected based on the results of Contract No. DAAG46-80-C-0070.[11] Refinements
to the above were made for individual defect groups, but all coupons within a
defect group were inspected under identical conditions so as not to treat each
coupon as a unique representative of a defect. The inspection refinements
were limited to changes in pulser-receiver settings to improve the graphic
quality of the analog C-scans generated by the plotter through the pulser-
receiver.

The two parameters which resulted in the greatest changes in defect
definition clarity were the transducer excitation energy and the pulser-
receiver attenuation limits. This is understandable and expected since the
analog C-scan is basically a graphical representation of the effect of mate-
rial attenuation on ultrasonic wave energy. Any subtle parametric variations
imparted by the pulser-receiver onto the material-induced attenuation effects
will tend to increase the definition of the presence of a defect because of
differential effects on the reflected/attenuated ultrasound. Because the
strength (amplitude) of an ultrasonic wave is greater after passing through
unflawed (low material attenuation) than through flawed (higher material
attenuation), the effect of attenuation filtering imparted by the pulser-
receiver has a relatively greater effect on the ultrasound reflected from a

flawed area because the pulser-receiver induced attenuation represents a greater proportion of the wave energy reaching the receiving transducer.

Each of the twenty new coupons and seven coupons from Contract No. DAAG46-80-C-0070 were inspected a minimum of three times each. The order the inspections was double blind randomized: each coupon received a random variable, and the inspection sequence was determined by a computer-generated random number table.

The randomizing of the inspection sequence was considered a necessary part of the program for two reasons. First, the randomizing would provide an indication of the effect of time on changes of flaw detectability or definition reproducibility. Second, the randomizing would require that each specimen be inserted and removed from the specimen holder a minimum of three times so the effects of specimen/transducer alignment could be determined.

Time between inspections was considered to be important since moisture retention and matrix erosion were shown to have an effect on inspection sensitivity during the previous program. After long periods without immersion, air bubbles would form on the faces of the specimen, which if not removed would cause excessive attenuation of the ultrasound passing into and through the coupon. Conversely, long periods of immersion or closely time spaced immersions would promote erosion of the surface matrix material. An irregular surface causes scattering of the penetrating ultrasound resulting in a lower detectability sensitivity. The numbered spots which appear on the analog C-scans are the inspection locations where wave attenuation coefficient and wave velocity measurements were recorded. The following coupons were selected as representatives of each of the defect group types, with coupon 01-3 being the unflawed control coupon from the previous program.
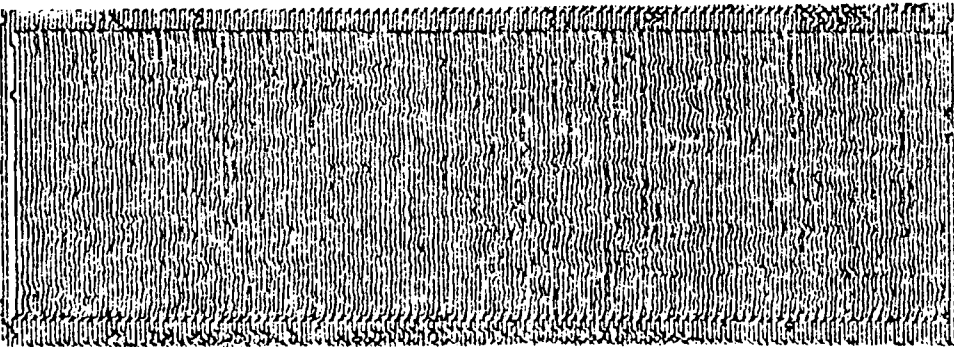
Coupon 01-3

Figure 21 shows the detectability/reproducibility analog C-scans for coupon 01-3 with no intentional flaws. As would be expected from an unflawed coupon, the C-scans show uniformly and regularly spaced scan lines with no horizontal deflections indicating the presence of flaws or defects.
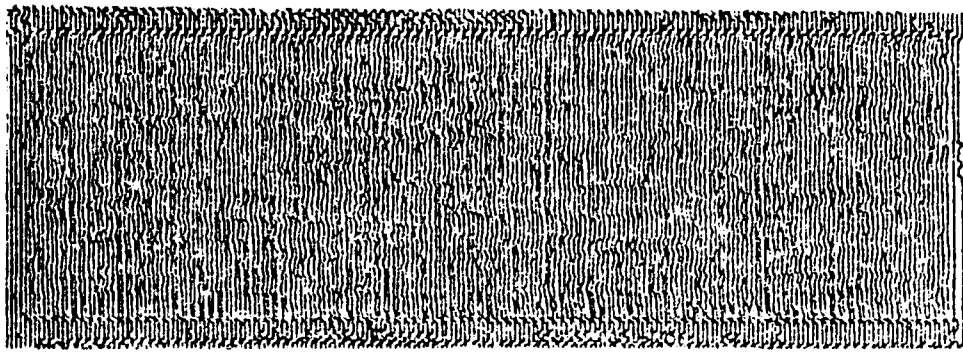
(a)
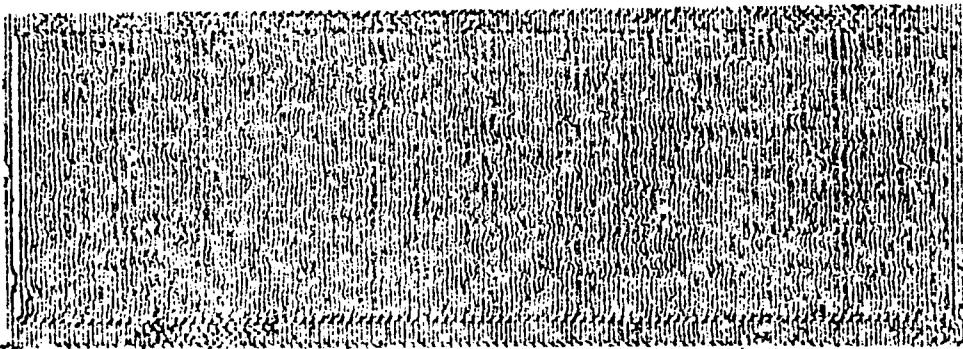
(b)

(c)

*Figure 21. Detectability/reproducibility analog C-scans
of FP/Mg coupon Ol-3 with no intentional flaws.*

Coupon N1-4

Figure 22 shows the detectability/reproducibility analog C-scans for coupon N1-4 with porosity. All three C-scans show the presence of a well-defined, highly attenuative defect area attached to the right vertical edge of the coupon. The defect ranges from approximately 16% of the coupon length for the upper half of the coupon to approximately 25% of the length for the lower half of the coupon. The three C-scans agree in definition, extent, and location of the defect area. The extreme attenuation of the reflected signal by the defect is of the nature that would be anticipated from porosity. Porosity causes internal wave scatter and increased wave travel paths, both of which result in a lower reflected wave energy (amplitude) which appears on a C-scan such as the defect area at the right side of specimen N1-4. For FP/Mg coupon N1-4 porosity, the ultrasonic inspection clearly and reproducibly shows the presence of a defect which has the attenuation characteristics of porosity.
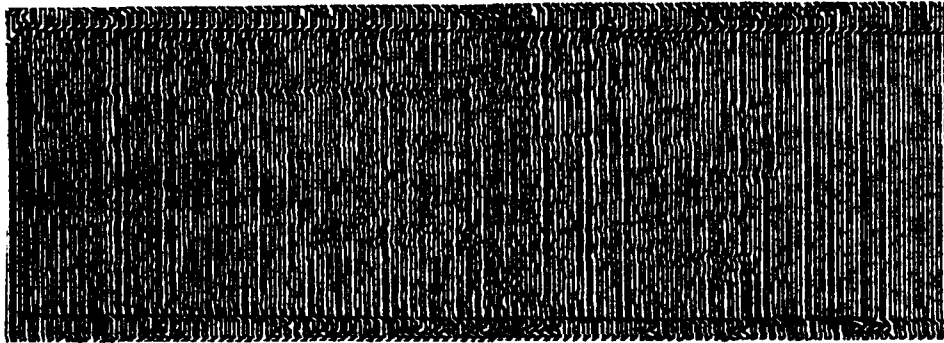
Coupon N2-2

Figure 23 shows the detectability/reproducibility analog C-scans for coupon N2-2 with nonuniform fiber volume ratio. The three C-scans clearly show the transition from the portion of the coupon with the 35% fiber volume ratio (left) to the portion with the 55% fiber volume ratio (right). The transverse diagonal appears on the C-scans because there is a difference in the attenuation of the ultrasound in each half of the coupon because of the relative percentages of fibers in the coupon. In the right side of the coupon (55% fiber volume), there is a greater percentage of fibers to scatter the ultrasound than on the left side, where there are less fibers to affect the passage of the ultrasound. These C-scans show that a 20% difference in fiber volume ratio across a closely controlled and well-defined boundary can be detected, but they do not give an indication of the sensitivity limit corresponding to a finite fiber volume ratio difference that ultrasonic inspection can detect. For FP/Mg coupon N2-2 with nonuniform fiber volume ratio, the ultrasonic inspection clearly and reproducibly shows the difference between the two areas of differing fiber volume ratio.
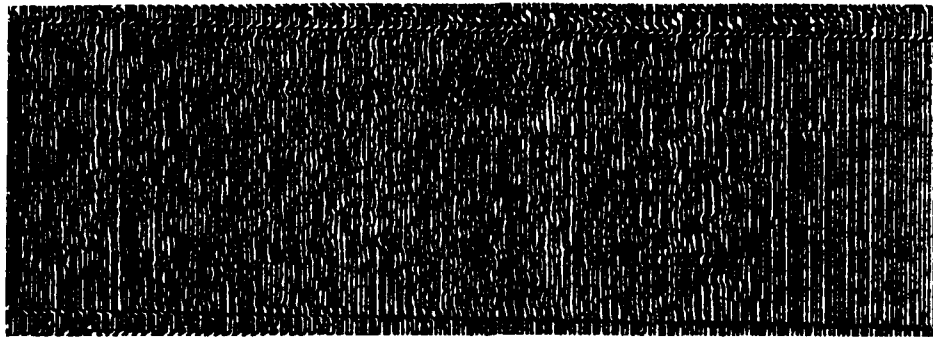
Coupon N3-1

Figure 24 shows the detectability/reproducibility analog C-scans for coupon N3-1 with ±20° off-axis fibers. The three C-scans indicate a distinct,
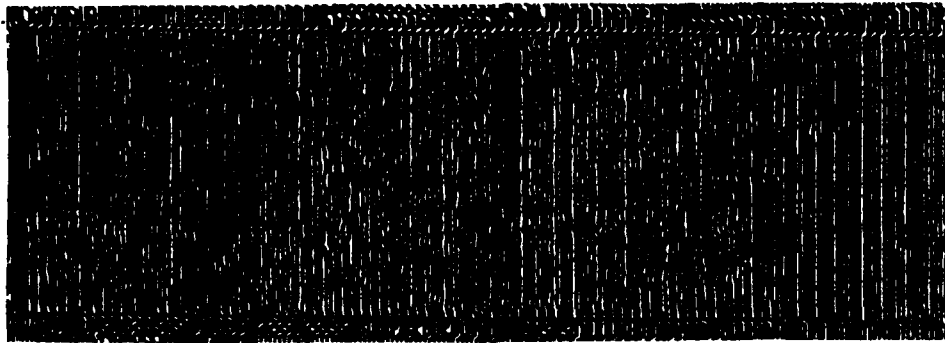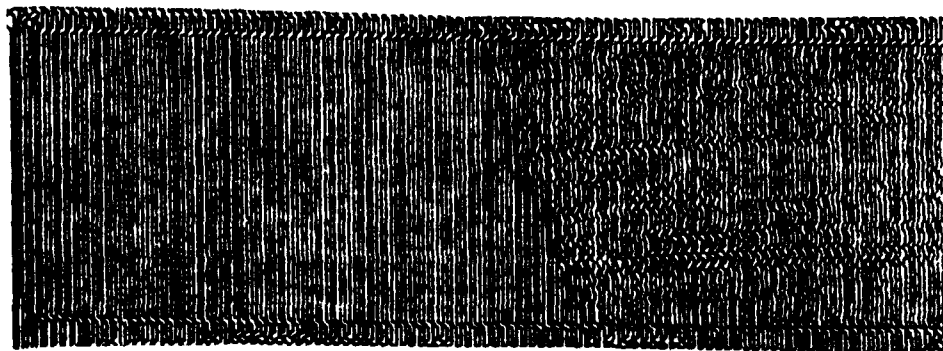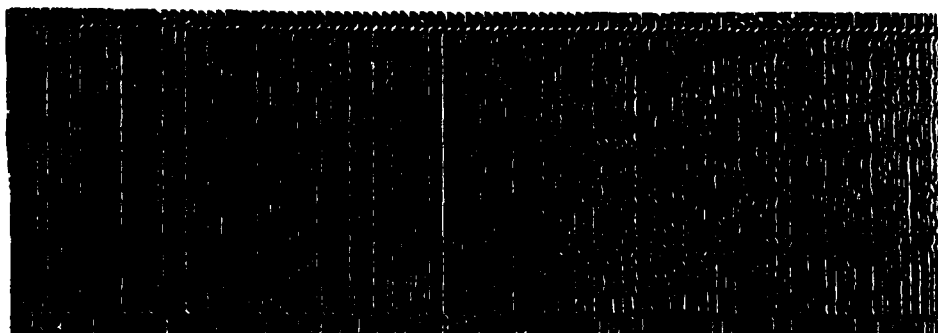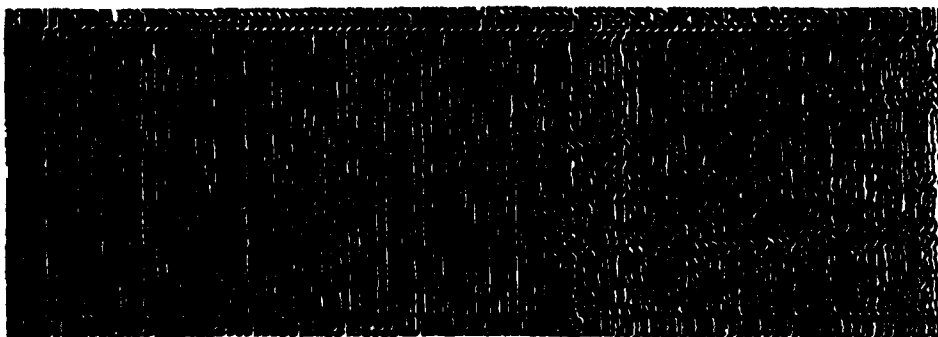
(a)

(b)

(c)

*Figure 22. Detectability/reproducibility analog C-scans
of FP/Mg coupon N1-4 with porosity.*
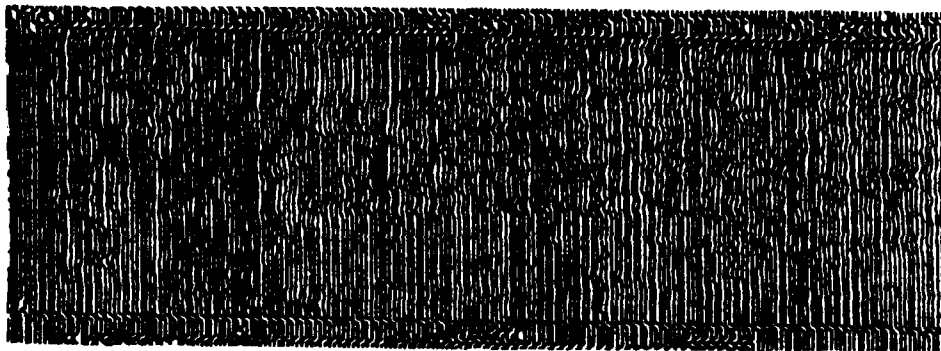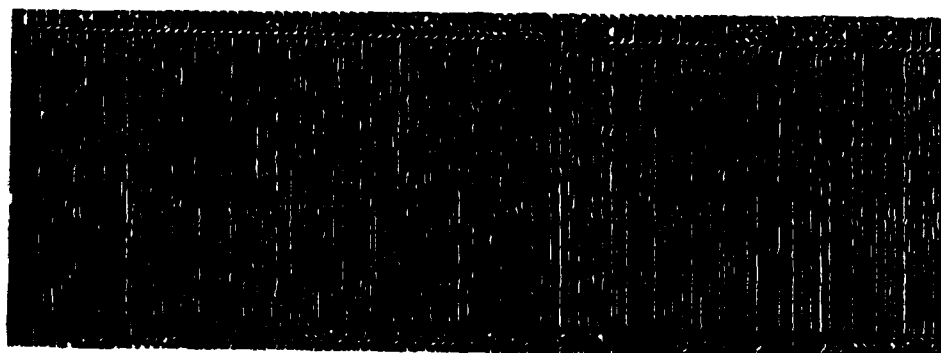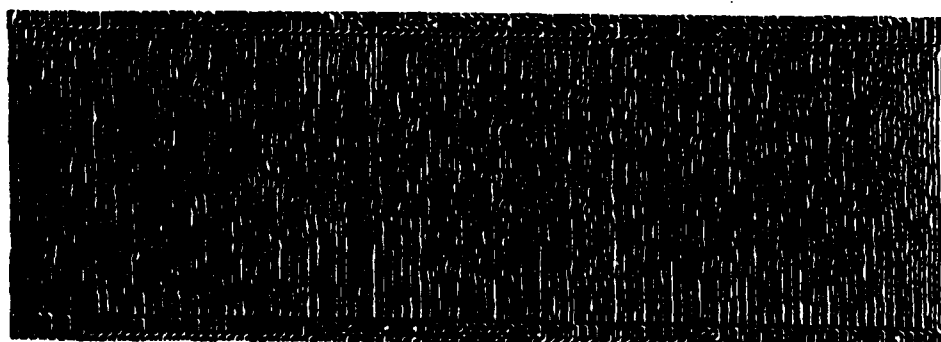
(a)

(b)

(c)

Figure 23. Detectability/reproducibility analog C-scans for FP/Mg coupon N2-1 with nonuniform fiber volume ratio.

(a)

(b)

(c)

*Figure 24.   Detectability/reproducibility analog C-scans
of FP/Mg coupon N3-1 with ±20° off-axis fibers.*

if somewhat muted, chevron pattern (mottling) which represents the off-axis fibers. The chevroning is caused by the fact that the third ply is oriented at +20°, and the fifth ply at -20° to the remaining six 0° plies, respectively. Because the off-axis plies are buried within the laminate, the definition of the fiber plies is not as sharp as it would be if the off-axis fibers were adjacent to a free surface or if ultrasound was focused on the ply containing the off-axis fibers. Similarly, the -20° fibers (running lower left to upper right) are not as well defined as the +20° fibers because the -20° fibers are shadowed by the +20° fibers, with respect to the path of the ultrasound from transducer to back face reflection. When the coupon was inspected from the opposite orientation, the -20° fibers predominated over the +20° fibers. This indicates that the greater the number of off-axis plies within a laminate, the less well defined subsequent off-axis plies on a C-scan will be. A corollary is that as the off-axis ply(s) are further along the ultrasound path (deeper into the specimen as viewed from the transducer) and/or if the angle of the off-axis fibers is small (less than 5°), the off-axis fibers are less clearly defined. For the FP/Mg coupon N3-1 with ±20° off-axis fibers, the ultrasonic inspection clearly and reproducibly shows the presence and orientation of each of the off-axis fiber plies.
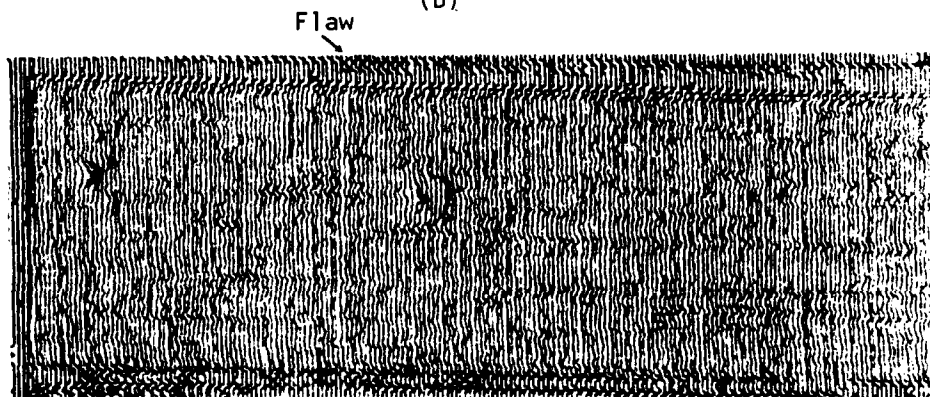
Coupon N4-1

Figure 25 shows the detectability/reproducibility analog C-scans for coupon N4-1 with butted fiber fracture. The three C-scans clearly define the position and extent of the butted fiber fracture which appears as a vertical stripe at the left center of the coupon. The defect appears to be as a skip of the pen in tracing the parallel, vertical scanning lines, but this is purely a function of the very localized nature of the defect. This defect helps to establish a detectability limit to the ultrasonic inspection procedure since the defect does not affect a large area of the coupon (like porosity) or its fundamental composition (like nonuniform fiber volume ratio). Additionally, the defect involves only one ply of the laminate at the coupon mid-thickness where it is most difficult to detect. It can be concluded that the ultrasonic inspection detectability limit for the butted fracture was within one fiber diameter or 0.01 mm (0.0005 in.). For FP/Mg coupon N4-1 with butted fiber fracture, the ultrasonic inspection clearly and reproducibly showed the presence, extent, and location of the fiber fracture.
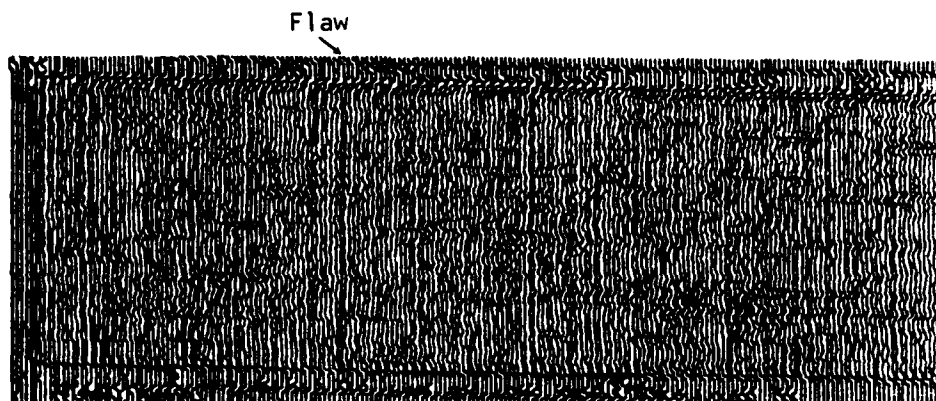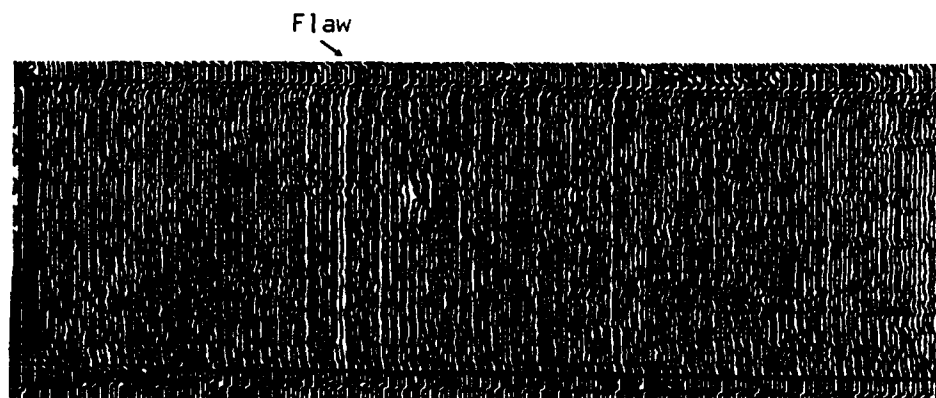
Figure 25. Detectability/reproducibility analog C-scans of FP/Mg coupons N4-1 with butted fiber fracture.
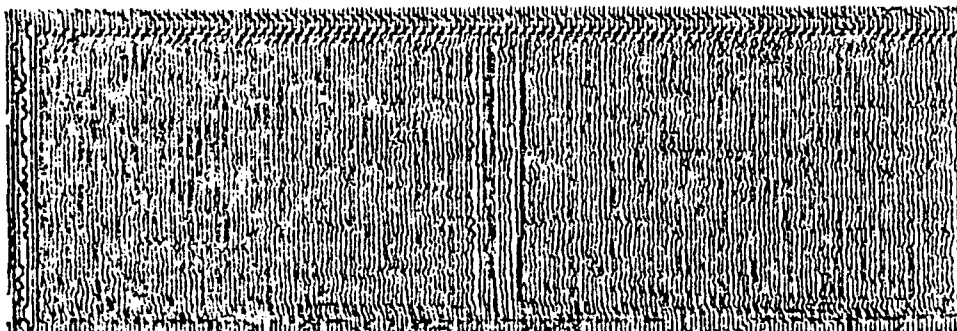
Coupon N4-3

Figure 26 shows the detectability/reproducibility analog C-scans for coupon N4-3 with 2.54 mm (0.1 in.) gap fiber fracture. The three C-scans clearly show the position and extent of the gapped fiber fracture which appears as a vertical band at the center of the coupon. The C-scans show that the gap is slightly wider, approximately 6.4 mm (0.25 in.), than specified for fabrication. It appears that one or both of the gap fiber plies migrated during the casting process causing the change in the gap separation dimension. Again, the defect was easily detected by ultrasonic inspection even though the fiber gap was located at the mid-thickness of the coupon. For FP/Mg coupon N4-3 with a gapped fiber fracture, the ultrasonic inspection reproducibly showed the presence, extent, and location of the fiber fracture.
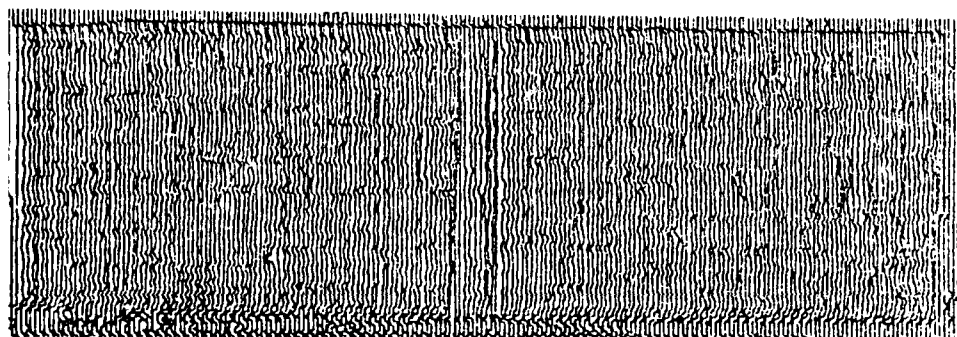
Coupon N5-1

Figure 27 shows the detectability/reproducibility analog C-scans for coupon N5-1 with fiber/matrix debonding. The three C-scans clearly display the position and extent of the four defect areas within the coupon. The defect areas are defined by the significantly higher signal attenuation which appears as vertical, parallel scan lines as compared to the more irregular lines of the unflawed surrounding material. Although the location, extent, and attenuative nature of the defect are obvious, and representative of fiber/matrix debonding, the ultrasonic C-scan cannot give any additional information to characterize the exact type of defect present. Without further characterization, this defect could be considered to be porosity, or, conversely, the defect indicated for coupon N1-4 could be considered to be fiber/matrix debonding. For FP/Mg coupon N5-1 with fiber/matrix debonding, the ultrasonic inspection clearly and reproducibly showed the presence, extent, and locations of four defect areas which have the attenuation characteristics of fiber/matrix debonding.

3.1.2 Wave Velocity/Attenuation Inspections

In addition to the ultrasonic scanning, each specimen was inspected point-to-point to determine wave propagation velocities and wave attenuation coefficients, since these were shown to be positive indicators of the presence, extent, and nature of flaws in the preceding project.

(a)

(b)
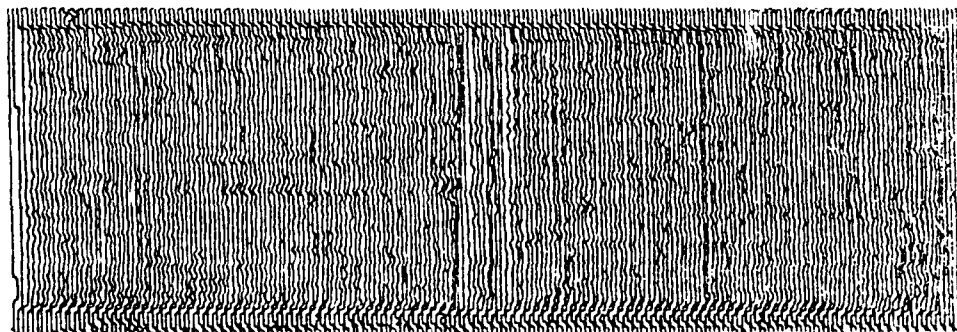
(c)

Figure 26. Detectability/reproducibility analog C-scans of FP/Mg coupon N4-3 with 2.54 mm (0.1 in.) gap fiber fracture.

(a)

(b)

(c)

Figure 27. Detectability/reproducibility analog C-scans of FP/Mg coupon N5-1 with fiber/matrix debonding.

Both the wave propagation velocity and the wave attenuation coefficient values were determined using a 10 MHz shear wave contact transducer external to the immersion tank. External measurements were found to be more reproducible and verifiable than immersion/water delay line techniques. The data presented in Tables 1 through 7 are the averages of a minimum of three measurement replications recorded at 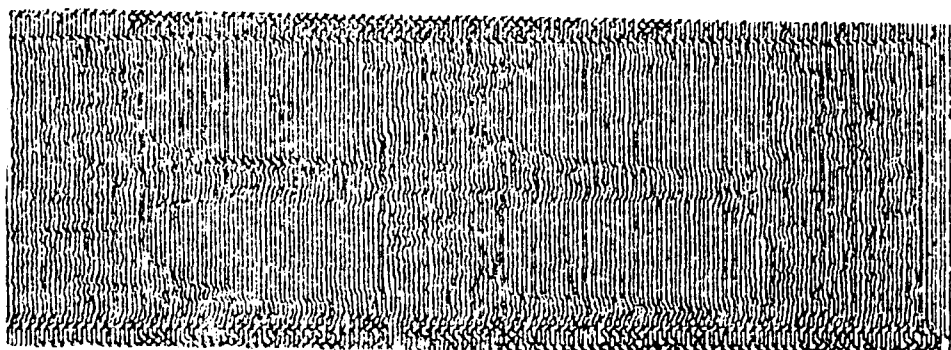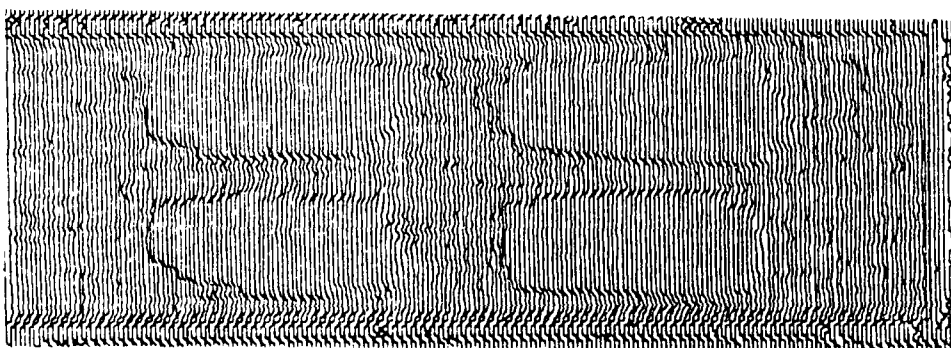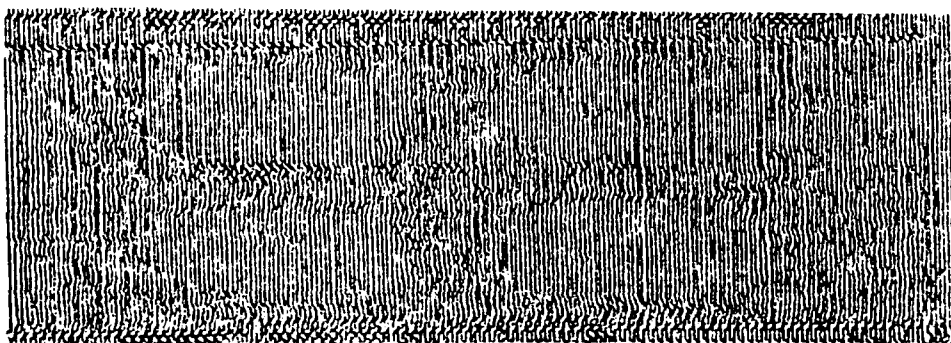each inspection location. The maximum allowable standard deviation for inclusion in the tables was 0.5% over the measurement population at each inspection location. The data presented in the tables correspond directly to the ultrasonically inspected representative coupons presented in the preceding section.

Coupon 01-3

Table 1 shows the wave propagation velocities and wave attenuation coefficients for FP/Mg coupon 01-3 with no intentional flaws (see Figure 28). Again, as would be expected of an unflawed coupon, both the wave velocity and wave attenuation show good stability and reproducibility across the coupon. The wave velocity varies by less than 1.5% by direct measurement. There is no clear explanation for the high wave attenuation coefficient at inspection location 3. The data were reproducible but inconsistent with the other locations on the coupon. One possible explanation is that the coupon surface condition was poor, with matrix material eroded; hence, the contact between transducer and coupon was poor, resulting in the unexpectedly high attenuation coefficient.

Coupon N1-4

Table 2 shows the wave propagation velocities and wave attenuation coefficients for FP-Mg coupon N1-4 with porosity. There is excellent correlation between the increase in the velocity and attenuation coefficient values and the defect area defined ultrasonically in Figure 29. Of principal interest is the attenuation coefficient, which increased on the average by 110% for the defect area over the unflawed area. This verifies that the defect is highly attenuative and dispersive, further indicating that the defect was, in fact, porosity. For coupon N1-4 with porosity, the wave velocity and attenuation coefficient values supported the ultrasonic inspections as to location and extent of the indicated defect, and were of a magnitude to corroborate that the defect was porosity.

Figure 28.   Ultrasonic attenuation inspection locations for specimen 01-3, control specimen (20 MHz C-scan).

TABLE 1.   WAVE PROPAGATION VELOCITIES AND WAVE ATTENUATION
COEFFICIENTS FOR FP/Mg SPECIMEN 01-3
WITH NO INTENTIONAL FLAWS

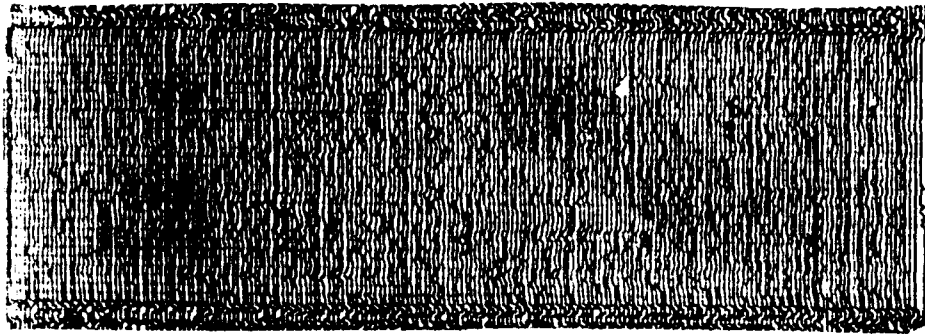| Inspection Location	Wave Propagation Velocities		Wave Attenuation Coefficients	
	m/s	10^5 in./s	dB/cm	dB/in.
1	6830	2.69	0.26	0.66
2	6850	2.70	0.21	0.53
3	6850	2.70	0.67	1.71
4	6870	2.70	0.11	0.28
5	6930	2.73	0.18	0.45
6	6900	2.72	0.19	0.49
7	6910	2.72	0.18	0.47
8	6890	2.71	0.21	0.53
9	6900	2.72	0.23	0.57
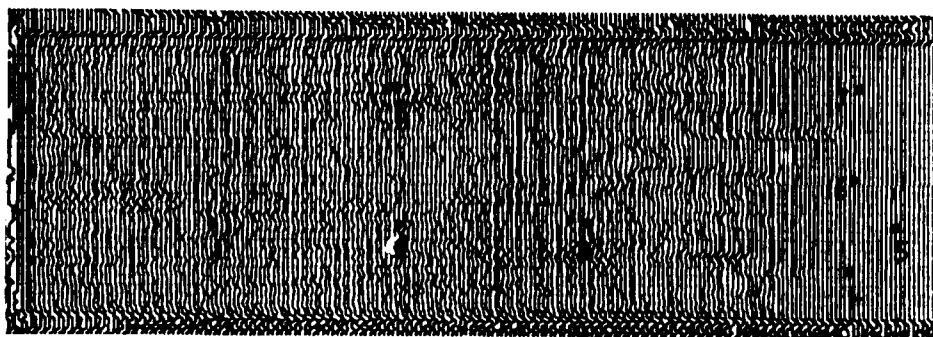
Figure 29.   Ultrasonic attenuation inspection locations for specimen N1-4, induced porosity (20 MHz C-scan).

TABLE 2.   WAVE PROPAGATION VELOCITIES AND WAVE ATTENUATION
COEFFICIENTS FOR FP/Mg SPECIMEN N1-4
WITH POROSITY

Inspection Location	Wave Propagation Velocities		Wave Attenuation Coefficients	
	m/s	10^5 in./s	dB/cm	dB/in.
1	6,625	2.61	0.11	0.27
2	6,620	2.61	0.18	0.44
3	6,660	2.62	0.22	0.55
4	25,400	10.00	0.35	0.88
5	17,225	6.78	0.38	0.96
6	20,200	7.95	0.41	1.05
7	17,100	6.73	0.38	0.96
8	6,620	2.61	0.21	0.52

Coupon N2-2

Table 3 shows the wave propagation velocities and wave attenuation co-
efficients for FP/Mg coupon N2-2 with nonuniform fiber volume ratio. Once
again, there is excellent correlation between the changes in wave velocity and
attenuation values and the definition in the ultrasonic C-scans of Figure 30.
The wave velocity for the 55% area is within 1%, on the average, of that of
the similar fiber volume percentage of the control coupon 01-3. Similarly,
there is an average 12% decre_se in the wave velocity between the 55% area
(inspection locations 3 through 6) and the 35% area (inspection locations 1,
2, 7, and 8).

Since wave velocity is not a direct function of fiber volume ratio, the
changes in velocity represent only the overall effect of the difference in
fiber volume ratio and do not represent magnitude differences in fiber volume
ratio directly. Similarly, the difference in wave attenuation coefficients
between the 55% and 35% areas is a drop of 47%. This also is merely a reflec-
tion of the effect of the change in fiber volume ratio and does not indicate
the magnitude differences of the ratios. The 35% area attenuation coeffi-
cients are lower than the 55% area because of the lower number of fibers pres-
ent to scatter and increase the path length of the ultrasound. For coupon N2-
2 with nonuniform fiber volume ratio, the wave velocity and attenuation values
support the ultrasonic inspection as to location and extent of the material
inhomogeneity and provide significant and consistent changes in magnitude to
quantify the variations in fiber volume ratio.

Coupon N3-1

Table 4 and Figure 31 show wave propagation velocities and wave attenu-
ation coefficients for FP/Mg coupon N3-1 with ±20° off-axis fibers. Since
this "defect" is homogeneous throughout the coupon, there is no basis for a
point-to-point comparison of the data for this coupon alone. Comparing the
average wave velocities of coupons 01-3 and N3-1 also shows an insignificant
difference of approximately 3%, which could be as easily attributed to mea-
surement error. This relationship also holds for the wave attenuation co-
efficients where there is a difference of 4% on the average between coupons
01-3 and N3-1. For coupon N3-1 with ±20° off-axis fibers, neither the wave
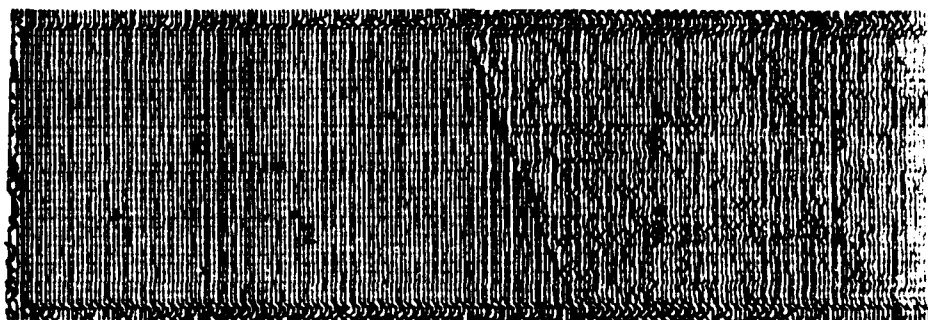
47

Figure 30. Ultrasonic attenuation inspection locations for specimen N2-2, nonuniform fiber volume ratio (20 MHz C-scan).

TABLE 3. WAVE PROPAGATION VELOCITIES AND WAVE ATTENUATION COEFFICIENTS FOR FP/Mg SPECIMEN N2-2 WITH NONUNIFORM FIBER VOLUME RATIO

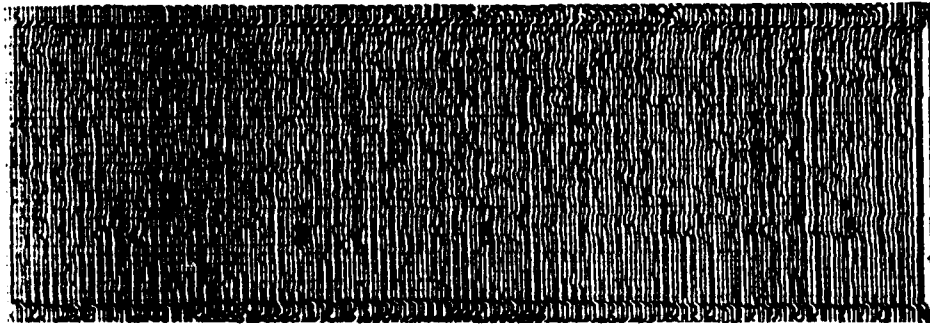| Inspection Location	Wave Propagation Velocities		Wave Attenuation Coefficients	
	m/s	10^5 in./s	dB/cm	dB/in.
1	6240	2.46	0.10	0.25
2	6220	2.45	0.12	0.31
3	6990	2.75	0.18	0.46
4	6910	2.72	0.26	0.66
5	6930	2.73	0.23	0.58
6	6960	2.74	0.39	0.99
7	6200	2.44	0.16	0.41
8	6210	2.44	0.18	0.46

Figure 31. Ultrasonic attenuation inspection locations for specimen N3-1, ±20° off-axis fibers (20 MHz C-scan).

TABLE 4.   WAVE PROPAGATION VELOCITIES AND WAVE ATTENUATION
COEFFICIENTS FOR FP/Mg SPECIMEN N3-1
WITH ±20° OFF-AXIS FIBERS

Inspection Location	Wave Propagation Velocities		Wave Attenuation Coefficients	
	m/s	10^5 in./s	dB/cm	dB/in.
1	6610	2.60	0.23	0.58
2	6610	2.60	0.15	0.38
3	6620	2.61	0.18	0.47
4	6610	2.60	0.17	0.44
5	6620	2.61	0.14	0.36
6	6720	2.64	0.19	0.47
7	6690	2.63	0.23	0.59
8	6690	2.63	0.39	0.99
9	6680	2.63	0.15	0.39

velocity nor attenuation coefficient values give any meaningful indication to the presence of the off-axis fibers.

Coupon N4-1

Table 5 and Figure 32 show wave propagation velocities and wave attenuation coefficients for FP/Mg coupon N4-1 with butted gap fiber. Because the size (width) of the gap defect was infinitesimally small compared to the contact area of the pulsing/receiving transducer, there was little expectation that the defect would be apparent as a change in either wave velocity or attenuation. The data in Table 5 show a slight change in wave velocity at inspection location 4 which coincides with the defect shown by ultrasonic inspection, but is not of the magnitude to be solely attributed to the butted fracture. Additionally, since the wave attenuation coefficient could not be calculated because of insufficient amplitudes (less than 3), there is no basis to use inspection location 4 as proof of the presence of the defect. For coupon N4-1 with butted fiber fracture, neither the wave propagation velocity or wave attenuation coefficient values give an unequivocal indication of the presence of the butted fracture.

Coupon N4-3

Table 6 shows wave propagation velocities and wave attenuation coefficients for FP/Mg coupon N4-3 with 2.54 mm (0.1 in.) gap fracture (refer to Figure 33). The wave propagation velocity values correspond with the ultrasonic scanning inspection in showing the extent and presence of the gap fracture. The wave velocity values at inspection locations 3, 4, and 5 average 5% lower than the surrounding unflawed material. This in itself is not a very dramatic difference in wave velocity, but it must be taken within the context that the gap is at the mid-thickness of the coupon and involves only one of the eight fiber plies. The wave attenuation values are conflicting and inconsistent with respect to the wave velocity measurements and ultrasonic inspection C-scans. For coupon N4-3 with gapped fiber fracture, the wave propagation velocity data reservedly indicate the presence of the defect, but the wave attenuation coefficients do not give any consistent, reliable evidence for the presence of the gapped fiber fracture.
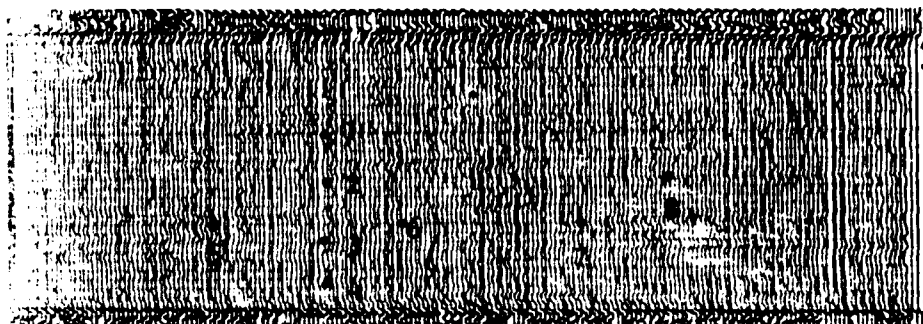
*Figure 32.   Ultrasonic attenuation inspection locations for specimen N4-1,
butted fiber fracture (20 MHz C-scan).*

TABLE 5.   WAVE PROPAGATION VELOCITIES AND WAVE ATTENUATION
COEFFICIENTS FOR FP/Mg SPECIMEN N4-1
WITH BUTTED FIBER FRACTURE

Inspection Location	Wave Propagation Velocities		Wave Attenuation Coefficients	
	m/s	10^5 in./s	dB/cm	dB/in.
1	6740	2.65	0.20	0.52
2	6740	2.65	0.20	0.51
3	6700	2.64	0.13	0.33
4	6670	2.63	*	*
5	6690	2.63	0.22	0.56
6	6710	2.64	0.20	0.50
7	6730	2.65	0.27	0.69
8	6780	2.67	0.18	0.45

*Amplitudes recorded were insufficient to calculate
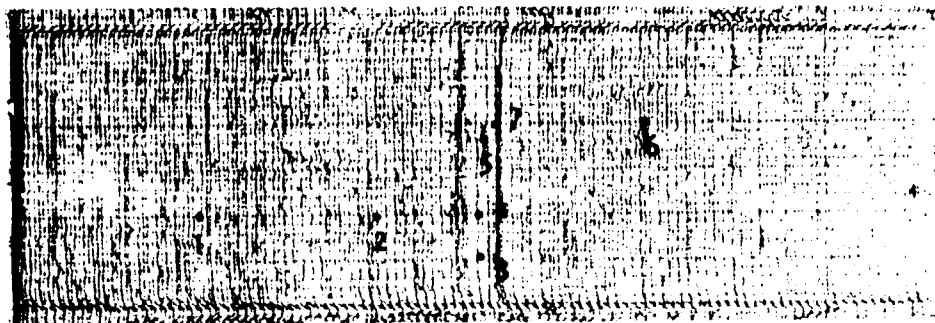attenuation coefficient.

51

Figure 33. *Ultrasonic attenuation inspection locations for specimen N4-3, 1/10 in. gap fiber fracture (20 MHz C-scan).*

TABLE 6. WAVE PROPAGATION VELOCITIES AND WAVE ATTENUATION
COEFFICIENTS FOR FP/Mg SPECIMEN N4-3
WITH 2.54 mm (0.1 in.) GAP FIBER FRACTURE

Inspection Location	Wave Propagation Velocities		Wave Attenuation Coefficients	
	m/s	10⁵ in./s	dB/cm	dB/in.
1	6750	2.66	0.17	0.42
2	6760	2.66	0.10	0.26
3	6480	2.55	0.30	0.77
4	6520	2.57	0.17	0.44
5	6490	2.55	0.33	0.85
6	6800	2.68	0.25	0.64
7	6840	2.69	0.51	1.29

Coupon N5-1

Table 7 shows wave propagation velocities and wave attenuation coefficients for FP/Mg coupon N5-1 with fiber/matrix debonding. Both the velocity and attenuation values show clear correlation with the ultrasonic C-scans shown in Figure 34. At the indicated defects, the apparent wave velocity increases an average of 171% over the surrounding unflawed material, while similarly the wave attenuation coefficient increases an average of 425% over the surrounding unflawed material. The wave propagation is considered to be an apparent increase within the context of the defect type and measurement procedure. Because the debonding is at the mid-thickness of the coupon, it appears to have the characteristics of a tight delamination in that it presents a reflective surface for the ultrasound to return from towards the contact transducer. When the thickness gage is calibrated to the mechanical thickness of the coupon and an internal defect reduces the path length of the ultrasound, the result is an apparent drastic increase in the wave propagation velocity. Alternatively, a tight delamination significantly dissipates the amplitude of the reflected ultrasound which is indicated as a substantial increase in the wave attenuation coefficient. The change in wave attenuation coefficient for the fiber/matrix debonding (425%) is significantly different from that of porosity (110%) to uniquely characterize the difference between the two defects. For coupon N5-1 with fiber/matrix debonding, both wave velocity and attenuation coefficient values correlated with the presence of the defects as shown by ultrasonic inspection, and were of such a magnitude as to clearly qualify the defect as being different from all others evaluated in this program.

3.2 MECHANICAL TEST RESULTS

3.2.1 Flexure Results

90° Three-Point Bending

The six flawed (porous) specimens, N1-3-1 through N1-3-6, from parent coupon N1-3 (Type 1 porosity) were invalid due to the presence of a crack extending approximately 75% through the 6.35 mm (0.25 in.) thickness of the parent coupon. The four unflawed specimens from that parent coupon (N1-3) were tested to failure and provided valid data. The maximum fiber stress
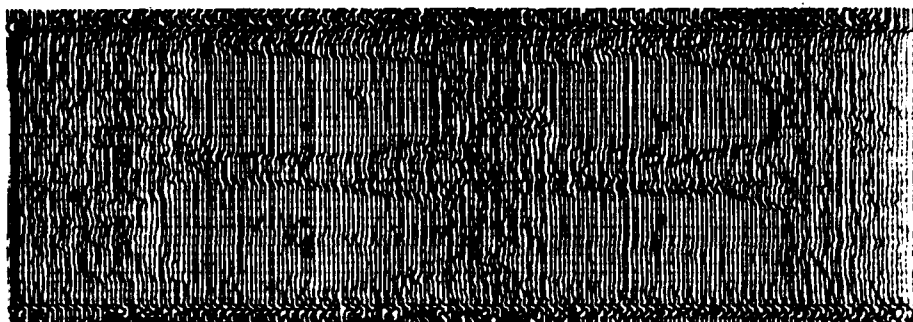
Figure 34. Ultrasonic attenuation inspection locations for specimen N5-1, fiber/matrix debonding (20 MHz C-scan).

TABLE 7. WAVE PROPAGATION VELOCITIES AND WAVE ATTENUATION COEFFICIENTS FOR FP/Mg SPECIMEN N5-1 WITH FIBER/MATRIX DEBONDING

Inspection Location	Wave Propagation Velocities		Wave Attenuation Coefficients	
	m/s	10^5 in./s	dB/cm	dB/in.
1	6,620	2.61	0.16	0.40
2	17,250	6.79	1.01	2.56
3	6,660	2.62	0.21	0.53
4	17,550	6.91	1.00	2.54
5	18,420	7.25	1.09	2.77
6	6,770	2.66	0.21	0.53
7	19,180	7.55	1.11	2.83
8	6,690	2.63	0.22	0.56

(tension) and average elastic modulus, E, are given in Table 8 for specimens N1-3-7 through N1-3-10.

The four unflawed specimens, N1-4-1 through N1-4-4, from the alternate Type 1 porosity coupon N1-4, as well as the six flawed (porous) specimens, N1-4-5 through N1-4-10, from coupon N1-4 were tested to failure in three-point bending. The maximum fiber stress (tension) and average elastic modulus, E, for the four unflawed and six flawed specimens from Type 1 porosity coupon N1-4 are given in Table 9.

0° Three-Point Bending

Four flawed and two unflawed 0° bending specimens from parent coupon N5-3 (Type 5, fiber/matrix debonding) were tested to failure in three-point bending. The maximum fiber stress (tension) and average elastic modulus, E, are given in Table 10.

3.2.2 Tensile Results

Three 0° tensile specimens from the unflawed coupon, 01-3, along with nineteen 0° tensile specimens from the various flaw types of the present contract, were tested to failure under axial loading in an Instron test machine. The applied load and the corresponding strain values were recorded at various intervals to failure. The load was recorded at the beginning and end of the scan of the four strain gages at each load interval. The two load values were averaged and divided by the nominal cross section of the gage area to compute the average axial tensile stress, σ_{Tavg}. The principal strains, E_{11} and E_{22}, from each gage were averaged because there was no indication of bending during axial loading. The average tensile stress and average principal strains were plotted and were used to calculate the elastic modulus, E_{11}, and the major Poisson's ratio, ν_{12}, as well as the ultimate tensile stress and the strain to failure. Table 11 summarizes the ultimate tensile stress, the average elastic modulus, E_{11}, the major Poisson's ratio, ν_{12}, and the strain to failure, $E_{11_T}^u$.

3.3 MICROSCOPY

Optical and SEM microscopy techniques were used to observe material structure and to correlate the fracture origins with flaws observed by NDE.

55

TABLE 8. MAXIMUM FIBER STRESS AND AVERAGE ELASTIC
MODULUS FOR UNFLAWED 90° 3-POINT BEND SPECIMENS
FROM PARENT COUPON N1-3 (POROSITY)

Specimen No.	Maximum Fiber Stress, MPa (psi)	Average Elastic Modulus, GPa (psi)
N1-3-7[a]	373.5 (54,170)	84.8 (12,290,000)
N1-3-8[a]	342.9 (49,730)	71.4 (10,350,000)
N1-3-9[b]	347.9 (50,460)	69.0 (10,000,000)
N1-3-10[b]	363.1 (52,650)	69.4 (10,060,000)

[a]Loaded perpendicular to fiber direction.

[b]Loaded parallel to fiber direction.

TABLE 9. MAXIMUM FIBER STRESS AND AVERAGE ELASTIC
MODULUS FOR 90° 3-POINT BEND SPECIMENS
FROM PARENT COUPON N1-4 (POROSITY)

Specimen No.	Maximum Fiber Stress, MPa (psi)	Average Elastic Modulus, GPa (psi)
N1-4-1[a]	369.9 (53,650)	75.87 (11,000,000)
N1-4-2[a]	365.9 (53,070)	68.83 (9,976,000)
N1-4-3[b]	368.3 (53,410)	65.65 (9,514,000)
N1-4-4[b]	357.5 (51,840)	64.87 (9,402,000)
N1-4-5[a]	313.9 (45,520)	94.64 (13,720,000)
N1-4-6[a]	278.1 (40,330)	100.90 (14,630,000)
N1-4-7[a]	242.1 (35,110)	97.97 (14,200,000)
N1-4-8[b]	158.9 (23,040)	100.30 (14,540,000)
N1-4-9[b]	148.7 (21,560)	99.48 (14,420,000)
N1-4-10[b]	154.5 (22,400)	96.99 (14,060,000)

Note: Specimens N1-4-1 through N1-4-4 are unflawed;
specimens N1-4-5 through N1-4-10 are flawed (porous).

[a]Loaded perpendicular to fiber direction.

[b]Loaded parallel to fiber direction.

TABLE 10. MAXIMUM FIBER STRESS AND AVERAGE ELASTIC
MODULUS FOR 0° 3-POINT BEND SPECIMENS FROM PARENT
COUPON N5-3 (FIBER/MATRIX DEBONDING)

Specimen No.	Maximum Fiber Stress, MPa (psi)	Average Elastic Modulus, GPa (psi)
N5-3-1[a]	787.2 (114,200)	199.9 (28,980,000)
N5-3-2	726.7 (105,400)	203.1 (29,440,000)
N5-3-3	705.9 (102,400)	196.1 (28,440,000)
N5-3-4[a]	766.0 (111,100)	199.9 (28,990,000)
N5-3-5	792.6 (115,000)	202.2 (29,330,000)
N5-3-6	762.7 (110,600)	209.0 (30,310,000)

[a]Unflawed specimen, all others flawed.

Polished cross sections were viewed with Nikon metallographic and binocular reflected light microscopes. Uncoated fracture surfaces were found to be sufficiently conductive for use in a JEOL 35CF SEM. At extremely high magnifications, the application of a conductive coating becomes necessary to avoid charging at the Al_2O_3 fibers.

3.3.1 Microstructural Analysis

Polished cross sections were not etched. FP fibers appear dark, and the Mg-phase appears light in the micrographs. Porosity appears almost black. Refer to the Appendix for information as to how the defect types were created during manufacturing.

Unflawed Control (Type 01)

Polished cross sections were prepared from material removed from four locations in a type 01 coupon. The locations and corresponding micrographs are shown in Figure 35. The material appeared uniform in all aspects. Fibers were evenly dispersed in the matrix material, and there was no evidence of porosity. This corresponds to results determined by NDE.

TABLE 11. MECHANICAL PROPERTIES OF TENSILE SPECIMENS

Specimen No.	Ultimate Tensile Strength, MPa (psi)	Average Elastic Modulus (E_{11}), GPa (10^6 psi)	Major Poisson's Ratio (ν_{12})	Tensile Strain at Failure ($E_{11}{}^\mu_T$)
01-3-1	344.06 (49,900)	199.27 (28.90)	0.238	0.00178
01-3-2	485.73 (70,447)	205.82 (29.85)	0.246	0.00246
01-3-3	527.19 (76,460)	207.40 (30.08)	0.261	0.00260
N2-2-1	399.22 (57,900)	177.89 (25.80)	0.205	0.00259
N2-2-3	376.74 (54,640)	129.63 (18.80)	0.305	0.00305
N2-3-1	326.62 (47,370)	202.78 (29.41)	0.222	0.00160
N2-3-2	342.10 (49,615)	196.99 (28.57)	0.235	0.00183
N2-3-3	353.87 (51,322)	156.72 (22.73)	0.170	0.00269
N3-1-1	266.40 (38,636)	194.23 (28.17)	0.267	0.00182
N3-1-2	441.90 (64,090)	190.16 (27.58)	0.269	0.00287
N3-1-3	346.72 (50,286)	170.24 (24.69)	0.284	0.00247
N3-3-1	496.94 (72,072)	196.99 (28.57)	0.229	0.00277
N3-3-2	526.43 (76,350)	201.27 (29.19)	0.263	0.00294
N3-3-3	335.32 (48,632)	195.61 (28.37)	0.255	0.00196
N4-1-1	462.88 (67,132)	192.85 (27.97)	0.252	0.00253
N4-1-2	470.36 (68,217)	194.23 (28.17)	0.239	0.00259
N4-1-3	438.93 (63,659)	186.37 (27.03)	0.324	0.00253
N4-3-1	468.27 (67,915)	196.99 (28.57)	0.229	0.00249
N4-3-2	461.87 (66,986)	194.23 (28.17)	0.232	0.00242
N4-3-3	467.36 (67,783)	195.61 (28.37)	0.234	0.00247
N5-1-1	430.05 (62,372)	199.89 (28.99)	0.239	0.00230
N5-1-2	407.63 (59,120)	188.85 (27.39)	0.219	0.00231

Repetition Rate ___2K___ Hz   Gated RF ___Medium / Low___
Damping _Variable/Maximum_ Ohms   Frequency __Greater Than 8_ MHz
Energy _____2_____   Peak Polarity _Negative_
Receiver Attenuation __4__ dB   Gain _____x10_____
High Pass Filter ___1.0__ MHz   Gain _____40_____ dB
Marked RF ____Interface____
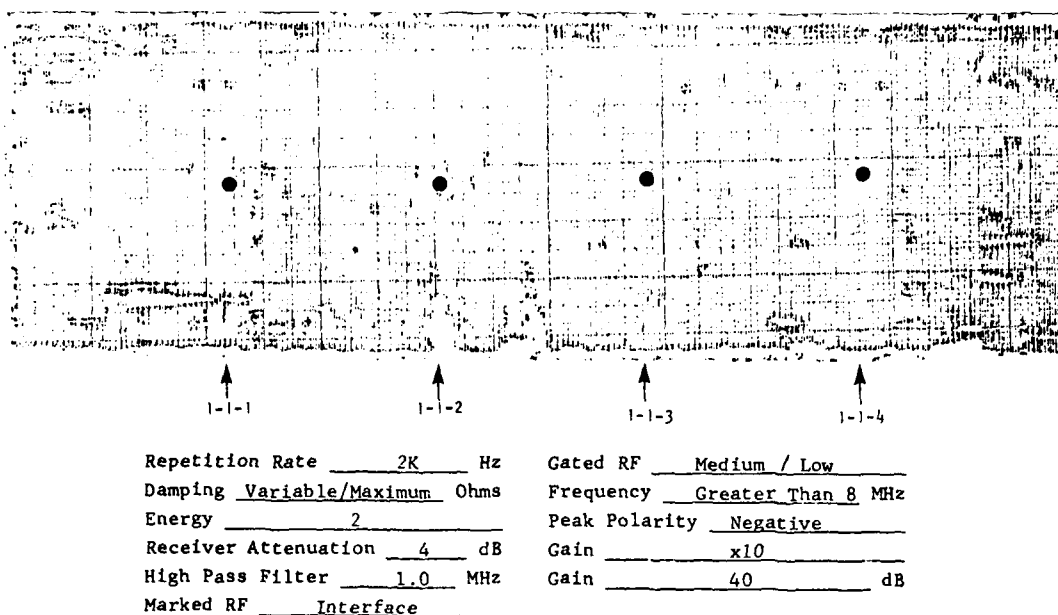
(a) Pen-lift C-scan of coupon 01-1, 15 MHz transducer in pulse-echo mode.

200X   200X
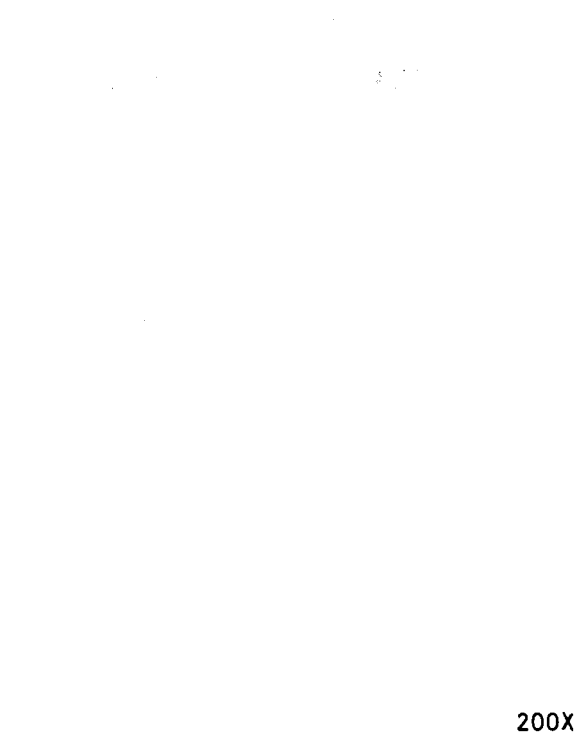
(b) Location 1-1-1.   (c) Location 1-1-2.

*Figure 35. Representative microstructure of type 01
(no intentional flaws) material.*[11]
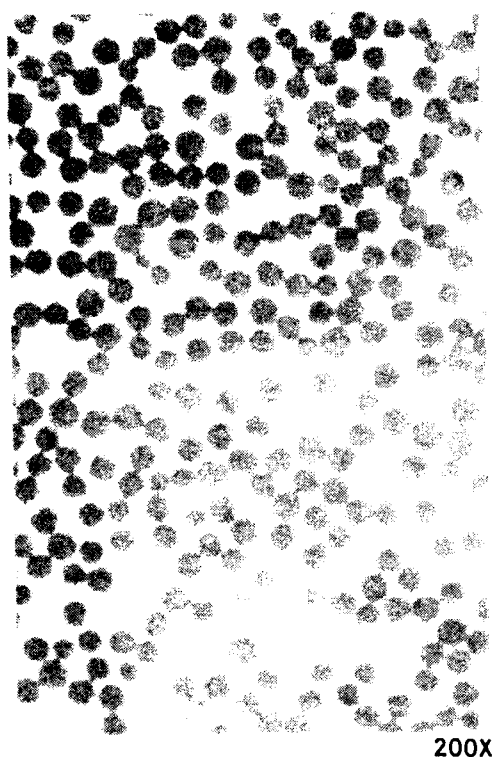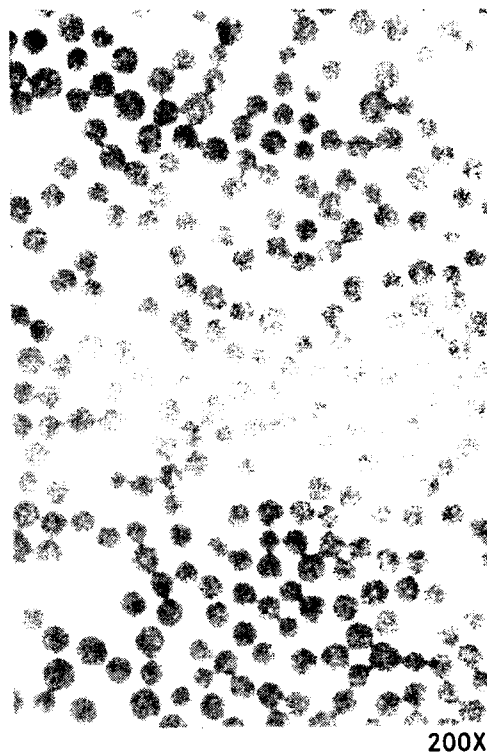
(d) Location 1-1-3.   (e) Location 1-1-4.

Figure 35. (cont.)

Induced Porosity (Type N1)

The porosity observed in various cross-sectional samples of type N1 coupons agreed with NDE results in terms of extent and location of porous regions. Porosity in the cast plate was created by depriving the casting of additional molten metal, which is usually added to fill voids created by metal shrinkage during the cooling process. Accordingly, bands of porosity parallel to the fiber direction were observed in analog C-scans (Figure 22) and wave velocity/attenuation inspection (Figure 29 and Table 2). With the unaided eye, the porous regions appear as dark bands on specimens cut for flexural testing. In a binocular optical microscope (refer to Figure 36a) dark, banded regions on a specimen removed perpendicular to the fiber direction indicate porosity formed in planes parallel to the stacked ply direction. Large pore clusters 0.5 to 5 mm may be seen as having formed along the fiber length (Figure 36b).

Tensile surface
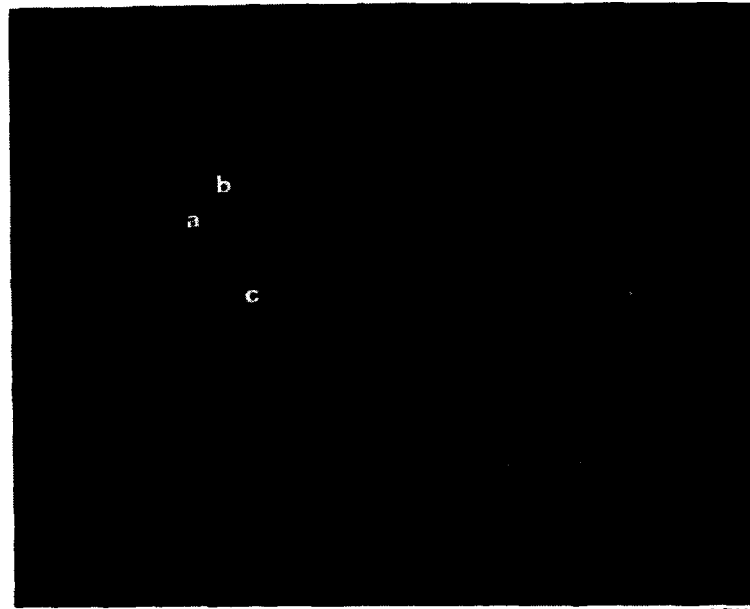
15X

(a) Specimen N1-3-4: dark bands are regions of low
    density and pore clusters of 1-3 mm are seen at
    locations a, b, and c.
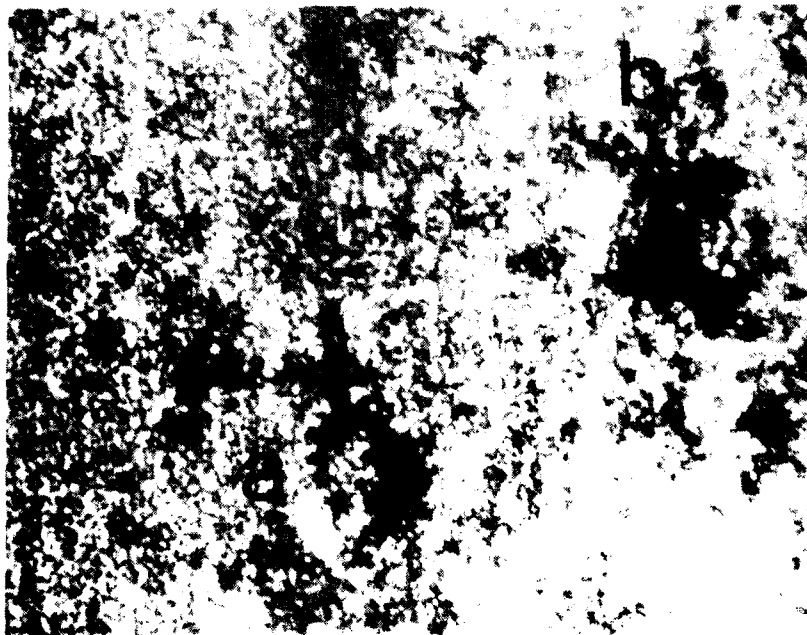
50X

(b) Higher magnification of specimen N1-3-4 with pores at
    a and b corresponding to locations in (a) above.

Figure 36. *Representative microstructure of type N1 (porosity) material.*

61

Nonuniform Fiber Volume Ratio (Type N2)

Polished sections of coupon N2-1 are shown in Figure 37. The induced defect in this type material was easily seen in the as-cast plate because the lower fiber volume region (Mg-rich) was more highly reflective. The micrographs in Figure 37 show a Mg-rich region at the point where fibers were cut out to create the lower density portion of the casting. The NDE techniques, indicating relative fiber volume changes, did not appear to locate the Mg-rich region at the interface, although the interface was well characterized by both NDE methods.

$\pm 10°$ and $\pm 20°$ Off-Axis Fibers (Type N3)

Microstructural analysis of samples containing off-axis fibers proved to be the most definitive technique for locating the material "defect." Transverse sections were removed from tensile samples and polished so as to see fiber diameter cross sections. Accordingly, $\pm 10°$ off-axis fibers (Figure 38c) should form smaller ellipses than $\pm 20°$ off-axis fibers (Figure 39c). Results showed that the 10° ellipses were not definitive by themselves, but only in relation to the 20° ellipses. The $\pm 10°$ and $\pm 20°$ off-axis specimens were then examined normal to the tensile direction. In this case, the longitudinal, uniaxial fibers were seen in lengthwise cross section. The off-axis fibers formed teardrop-shaped cross sections which corresponded to an 80° ellipse for the 10° off-axis fibers (see Figure 38e), and to a 70° ellipse for the 20° off-axis fibers (see Figure 39e). Samples prepared in this direction were fairly difficult to prepare due to fiber fracture along the fiber length.

Butted and 1/10 in. Gap Fiber Fracture (Type N4)

Coupons containing butted fibers in one ply had their defect successfully located by ultrasonic C-scans, but not by wave velocity/attenuation due to the small, localized nature of the defect. The sample chosen for micrographic inspection was tensile specimen N4-1-2, which had not fractured at the defect region. Polishing revealed that the location of the defect as determined ultrasonically was correct (and further confirmed by fractography of the samples which failed at the defect region, see Figure 47 in Section 3.3.2). Figure 40 shows the defect. Two bundles of fibers have been cut and butted together and are slightly offset. At the abutment are fibers which are

55 v/o   35 v/o

12X

(a) Low magnification view of polished coupon N2-1 show-
ing the change in fiber volume.

55 v/o   35 v/o

50X

(b) 35/55 volume percent interface region of
coupon N2-1.

Figure 37. *Representative microstructure of type N2 (nonuniform*
fiber volume ratio) material.
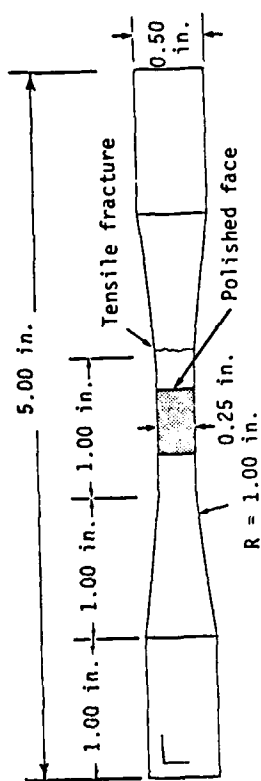
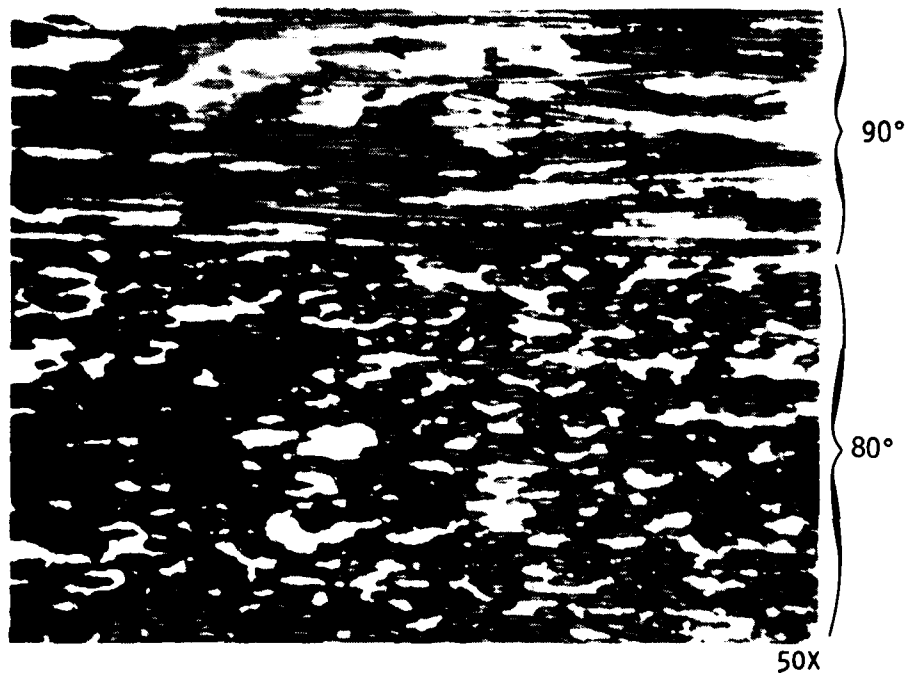(a) Schematic showing the location of the transverse section removed for microstructural analysis from specimen N3-3-3.
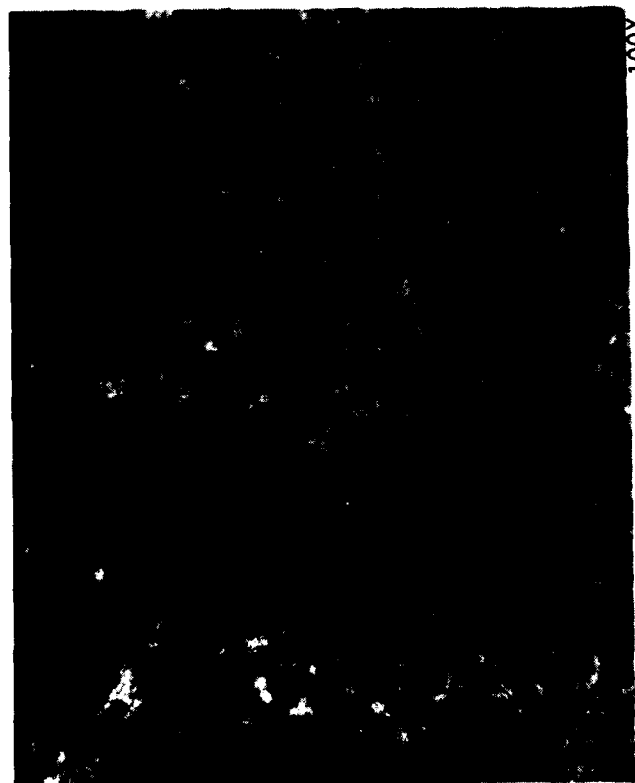
(b) Optical micrograph of polished cross section of sample N3-3-3 showing the uniaxial/10° off-axis fiber interface
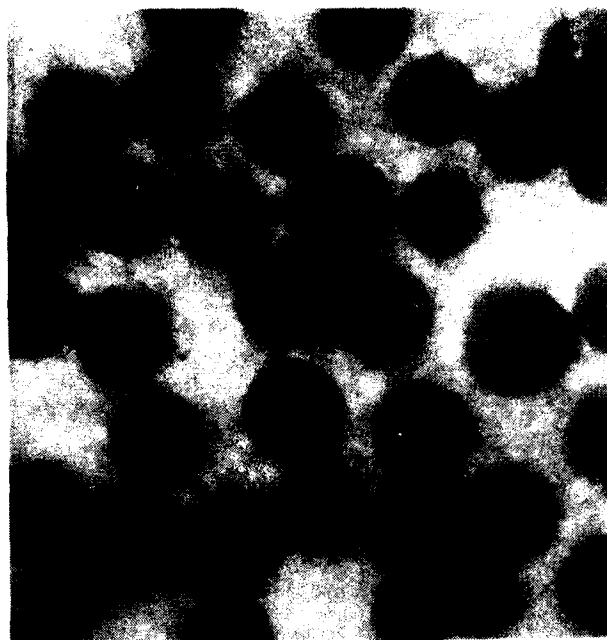
(c) Optical micrograph of fibers oriented 10° off-axis in sample N3-3-3.

Figure 38. Representative microstructure of type N3-3 (±10° off-axis fibers) materials.

64

(d) Polished specimen N3-3-1 showing the uniaxial/10° off-axis interface normal to the tensile direction.
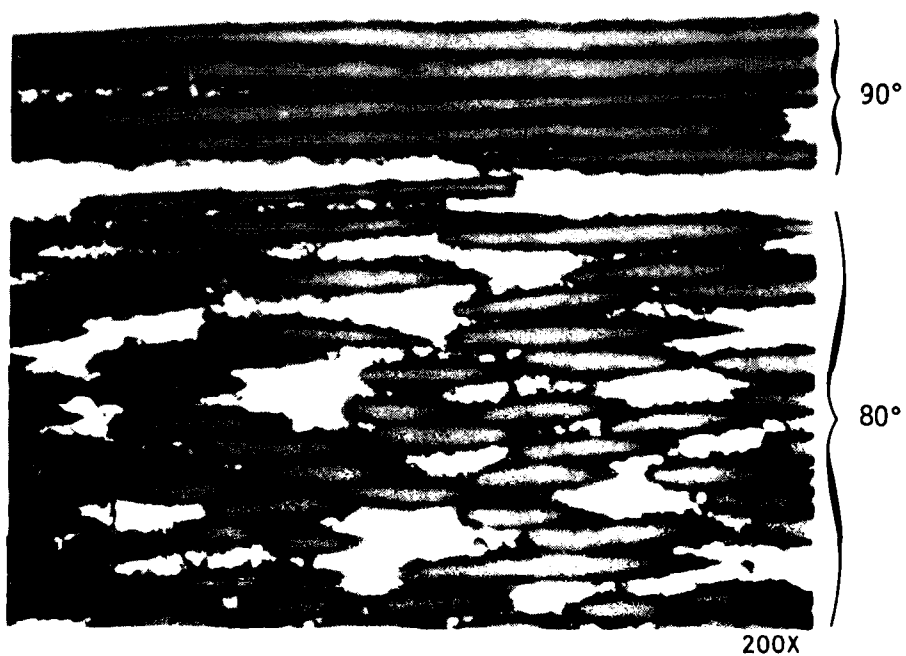
(e) Higher magnification of (d) above.

Figure 38. (cont.)
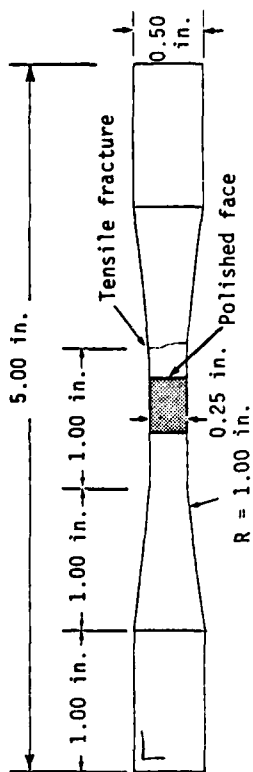
(a) Schematic showing the location of the section removed for microstructural analysis.
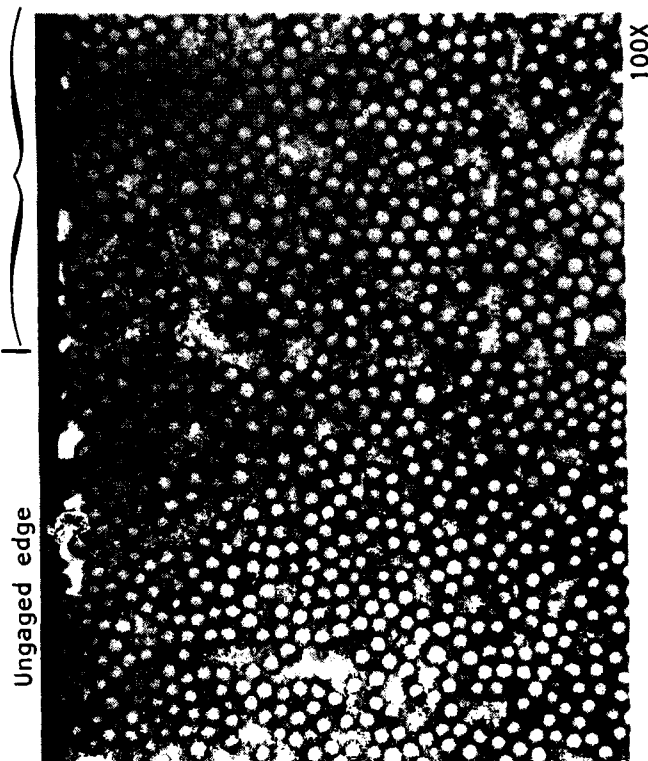
(b) Optical micrograph of polished cross section of sample N3-1-1 section showing the uniaxial/20° off-axis fiber interface.

(c) Optical micrograph of fibers oriented 20° off-axis in sample N3-1-1.

Figure 39. Representative microstructure of type N3-1 (±20° off-axis fibers) material.

90°

70°

50X
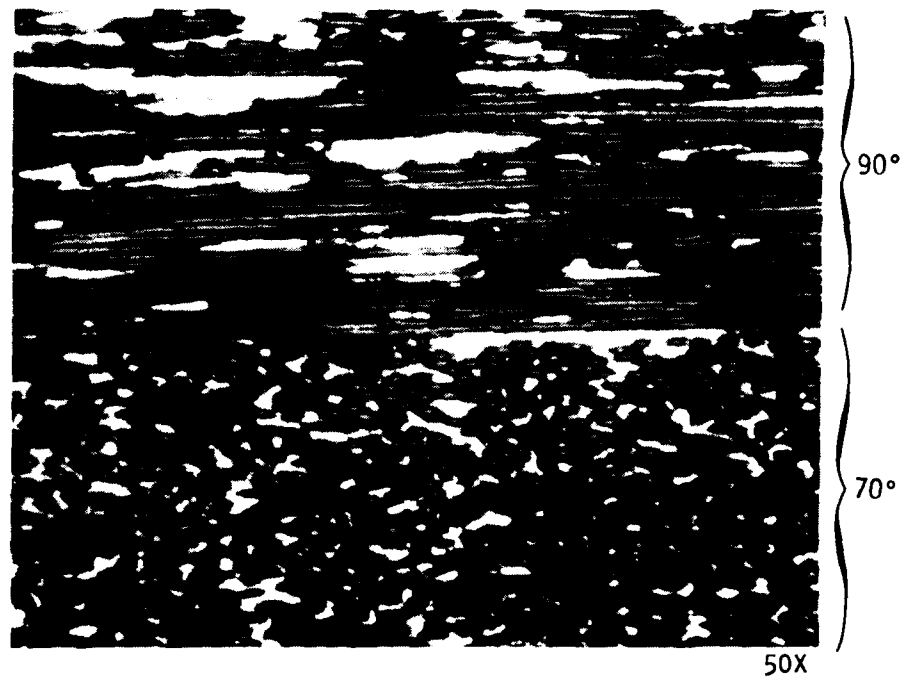
(d) Longitudinal polished section of specimen N3-1-2 showing uniaxial/20° off-axis interface (normal to the tensile direction).

90°

70°
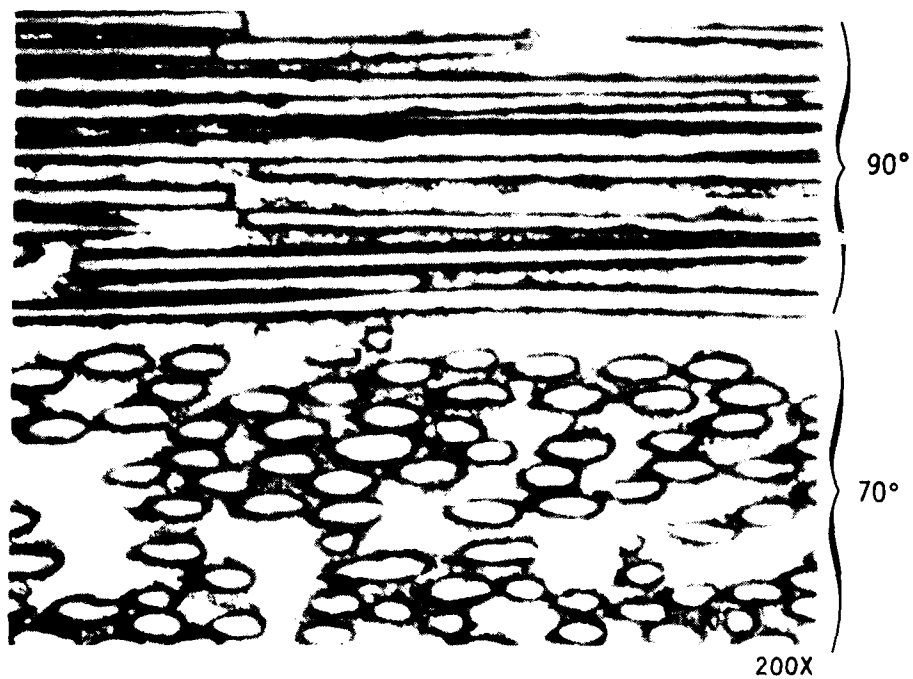
200X

(e) Higher magnification view of (d) above.

Figure 39. (cont.)
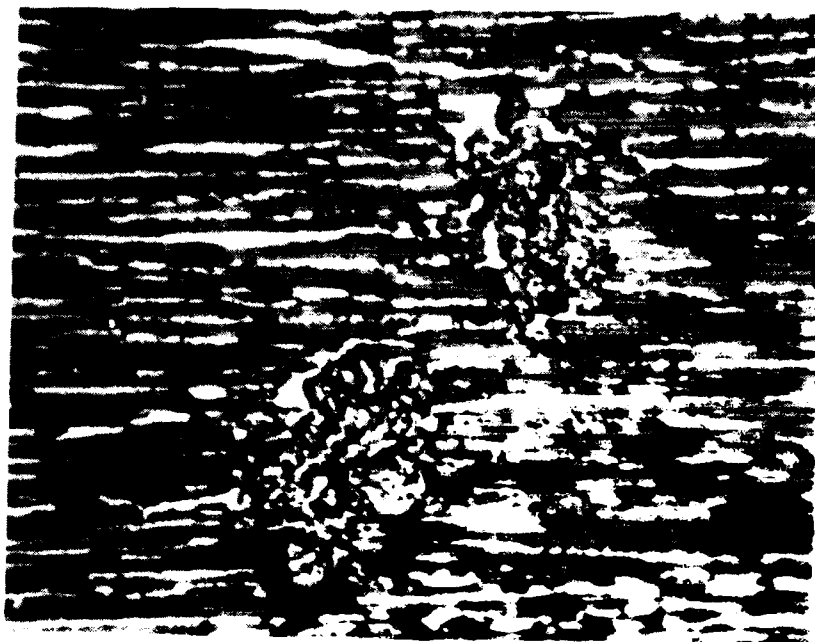
(a) Longitudinal view (normal to the tensile direction) of specimen N4-1-2 showing the two butted fiber plies.

(b) View of transverse fibers and Mg-rich region of one butted ply of specimen N4-1-2.

Figure 40. Representative microstructure of type N4-1 (butted fibers) material.

primarily in plane, but 90° to the uniaxial fibers. Magnesium-rich regions are also evident.

Figure 41 shows the cross section of tensile specimen N4-3-3. The polished section was prepared from the material cut away from the rectangular specimen to form the necked-down gage section (the sample subsequently fractured at the gapped region in the gage section). The gap was easily seen with the unaided eye and consisted of an Mg-rich area approximately 1/32 x 3/16 in. The micrograph shown in Figure 41 at 20X indicates the Mg-rich region is 1/32 in. thick at the center of the gap, and thicker at the ends of the gap.

Fiber/Matrix Debonding (Type N5)

This gross defect type was detected by NDE and confirmed by microscopy. The polished sample shown in Figure 42 was taken from the necked down region of tensile specimen N5-1-2, since the other debonded region was in the gage section and was the failure location. Metallography showed that the debonded areas defined by NDE were of the size and location indicated by those techniques. What the micrograph indicates that was not shown by either ultrasonic or wave velocity/attenuation methods is that two plies and three layers of boron nitride slurry were involved in creating the defect region. Additionally, this defect differs from the porosity seen in type N1 specimens in that the delaminated area is a continuous feature between plies, rather than discrete pores along fiber lengths.

3.3.2 Fracture Surface Analysis

All tensile and 3-point bend samples tested to failure were examined in a binocular microscope for determination of the fracture origin of each sample.

Unflawed Control Specimens (Type 01)

Three unflawed samples were tested in tension. The fracture surfaces were fairly flat, having little fiber pull-out. Features similar to those found in brittle, monolithic materials were observed: a flat region near the origin and lines radiating outward from there. One sample (01-3-1) had an origin (near a corner just below the gaged surface) which appeared to be a large Al_2O_3 fiber. Sample 01-3-2 had a fracture initiating from misaligned fibers on the gaged surface where they intersected a corner. The last sample's origin was unidentified. Fracture surfaces are shown in Figure 43.
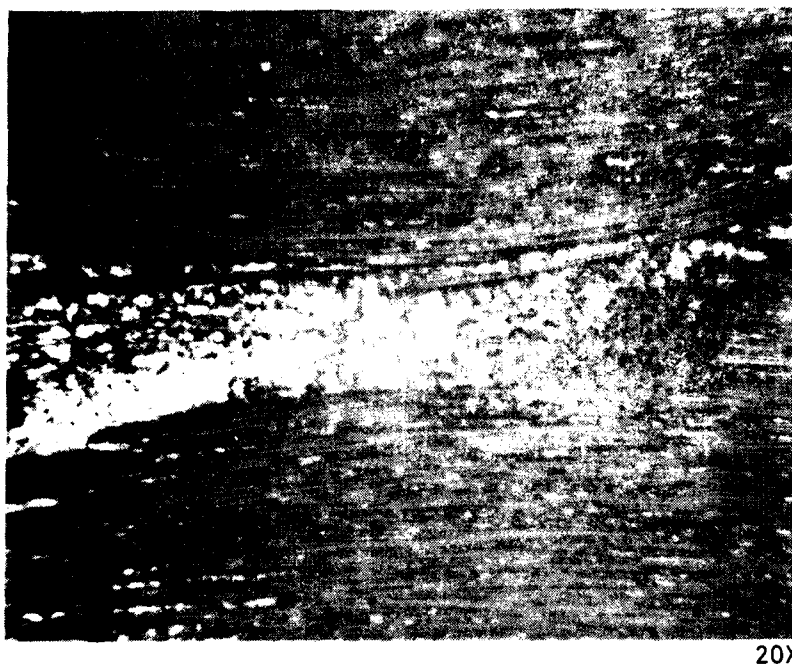
20X

Figure 41. *Representative microstructure of type N4-3 (1/10 in. fiber gap) material showing the Mg-rich region as viewed normal to the tensile direction.*
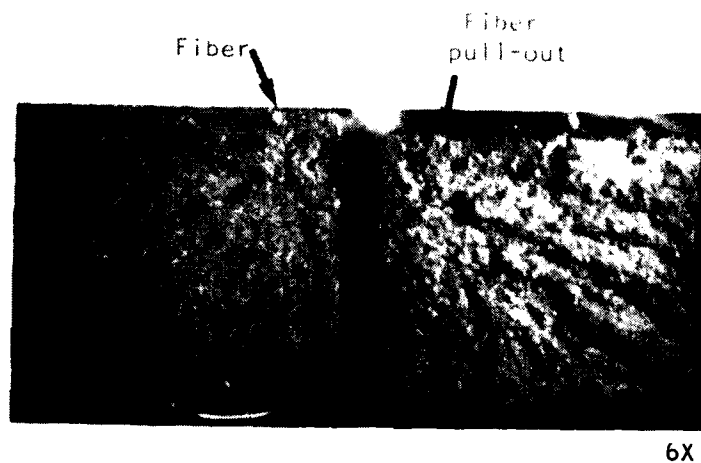

11.5X

Actual specimen thickness: 0.25 in.
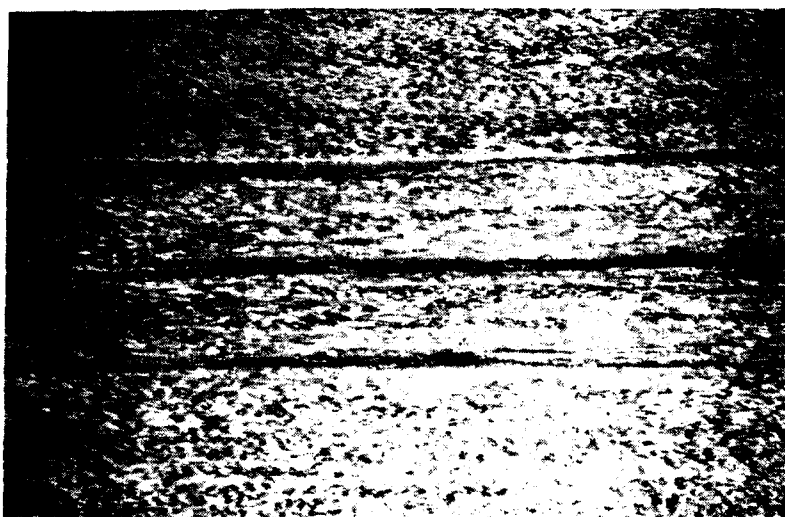
Specimen N5-1-2: longitudinal cross section.

Figure 42. *Representative microstructure of type N5 (fiber/matrix debonding) material.*

(a) Specimen 01-3-1 fracture surface indicating a large Al_2O_3 fiber fracture origin.

(b) Specimen 01-3-2 gage surface showing the misaligned Al_2O_3 fibers which were the fracture origin.

Figure 43. *Representative fractures of Type 01 (unflawed) material tested in uniaxial tension.*

71

Induced Porosity Specimens (Type N1)

The billets of material containing porosity were tested in three-point flexure. Four samples were prepared from billet N1-3's unflawed region. Of these, three fracture origins were undetermined. The other sample contained a large Al_2O_3 fiber fracture origin similar to that of sample 01-3-1. Six samples from the flawed and four samples from the unflawed regions of billet N1-4 were examined after being broken in three-point flexure in two orientations. No fracture origins could be determined for the unflawed samples. Porosity was easily observable in the flawed samples; however, pores or pore clusters did not appear to act as fracture origins. Fracture surfaces of these 90° samples appeared "stepped" as the crack path moved from one region of high porosity to another. An example of a porous flexure specimen is shown in Figure 44.

Nonuniform Fiber Volume Ratio Specimens (Type N2)

Tensile samples were machined from two billets (N2-2 and N2-3) containing nonuniform fiber distributions such that the volume interface boundary was within the gage section. The fracture surface analysis of these samples was straightforward since samples generally failed at the interface. Variation among samples occurred as to the extent of Mg-rich region that was visible on the fracture surface. That is, all samples failed at the transition region which varied in magnesium content somewhat from sample to sample. An example of the fracture surface of this type sample may be seen in Figure 45.

±10° and ±20° Off-Axis Fiber Specimens (Type N3)

Two types of off-axis samples were prepared for tensile testing: ±10° and ±20°. The three ±10° off-axis samples had rough fracture surfaces with some brittle fracture markings. Origins were within off-axis layers--one where the off-axis fibers intersected the corner of the sample, and two within off-axis bands of fibers which intersected the machined, non-gaged edges of the samples. Interestingly, the ±20° off-axis samples also had brittle-type fracture surface features. Origins were on the as-received, gaged surfaces of the samples very close to a corner and consisted of corrosion pits where Mg presumably had been removed during the ultrasonic evaluation due to the reaction of magnesium with water: $Mg_{(s)} + H_2O_{(l)} \rightarrow MgO_{(s)} + H_2(g)$. Figure 46 illustrates off-axis types of fracture surfaces.

72
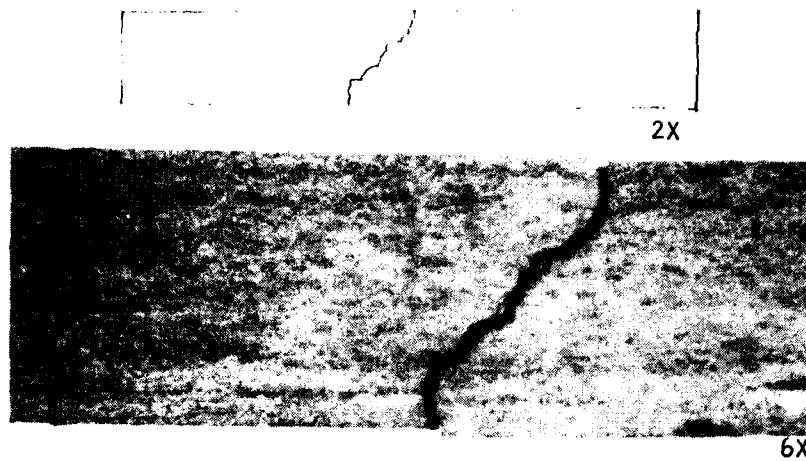
(a) Schematic and micrograph of specimen N1-4-5 cross
section showing the crack path through regions of
porosity.
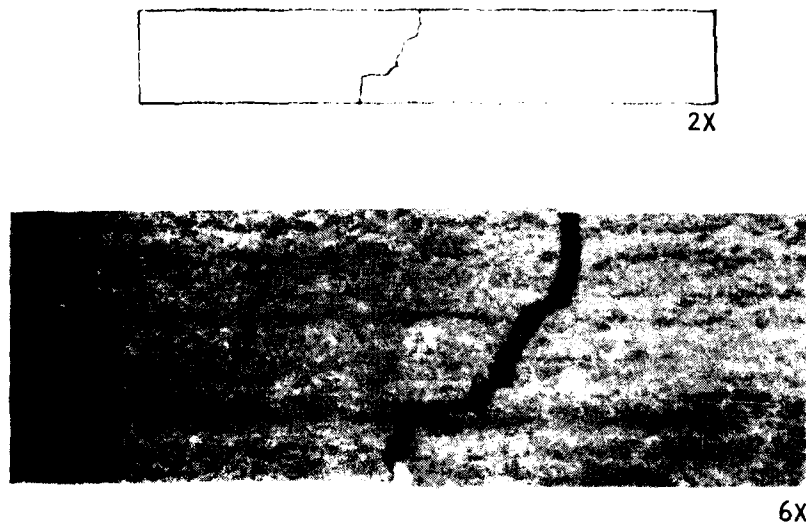
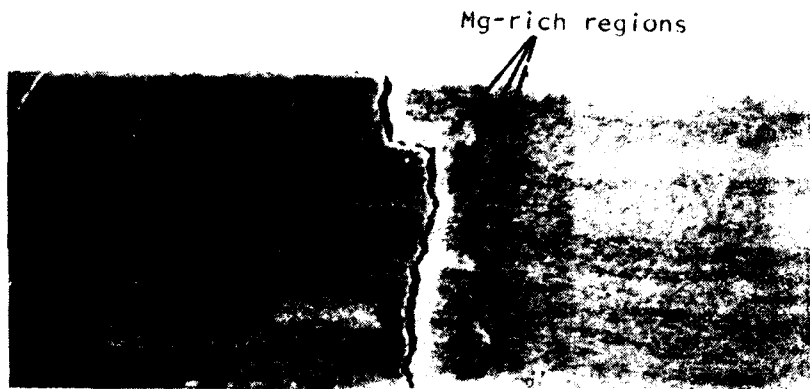(b) Schematic and micrograph of specimen N1-4-6 cross
section showing the crack path deflection at and
subsequent movement along a band of porosity.

*Figure 44. Representative fractures of type N1 (porosity) material
tested at 90° in 3-point flexure.*

55 v/o   35 v/o
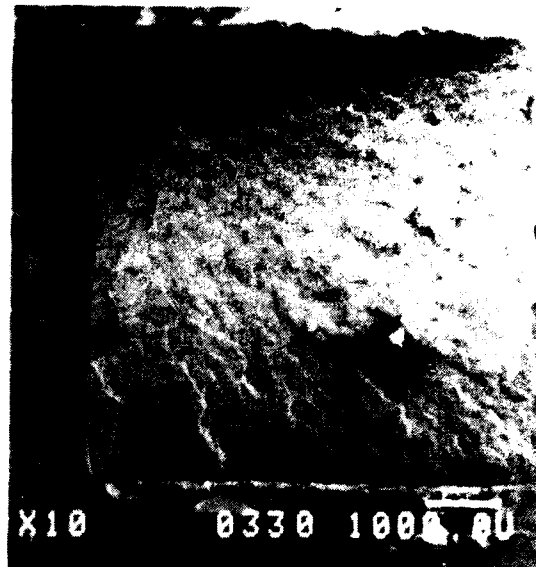
(a) Side view of specimen N2-2-3.

Mg-rich regions

7X

(b) Magnified view of (a) above showing the fracture
    path along the 55/35 volume percent fiber inter-
    face.

7.5X

(c) Fracture surface (gaged surfaces together)
    showing the metal-rich region at the 55/35
    volume percent fiber interface.

*Figure 45. Representative fracture of type N2 material
having nonuniform fiber distribution.*

(a) SEM view of specimen N3-3-3 (±10°
    off-axis fibers): fracture origin
    is in the upper lefthand corner.
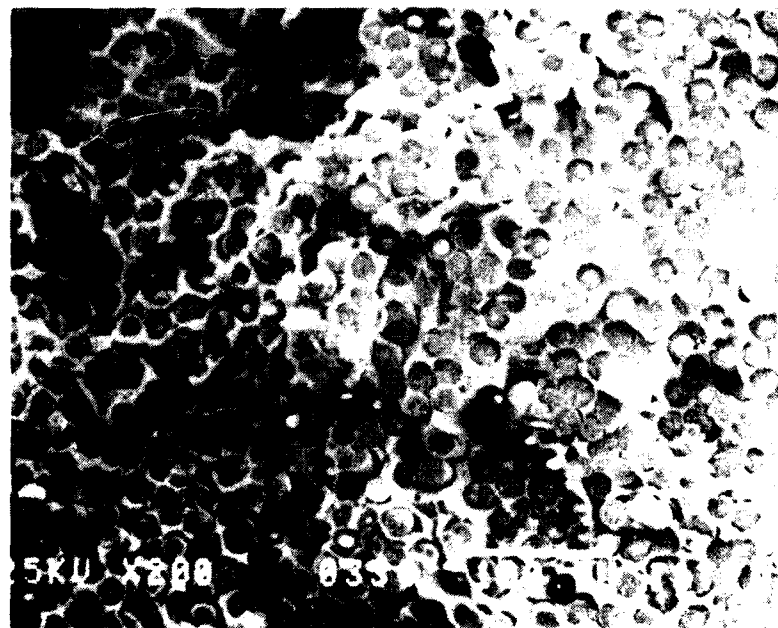
(b) View of specimen N3-3-3 in the 0° fiber portion of
    the fracture surface.

Figure 46. Representative fracture surfaces of type N3-3 and N3-1
(±10° and ±20° off-axis fibers, respectively) material tested in
uniaxial tension.
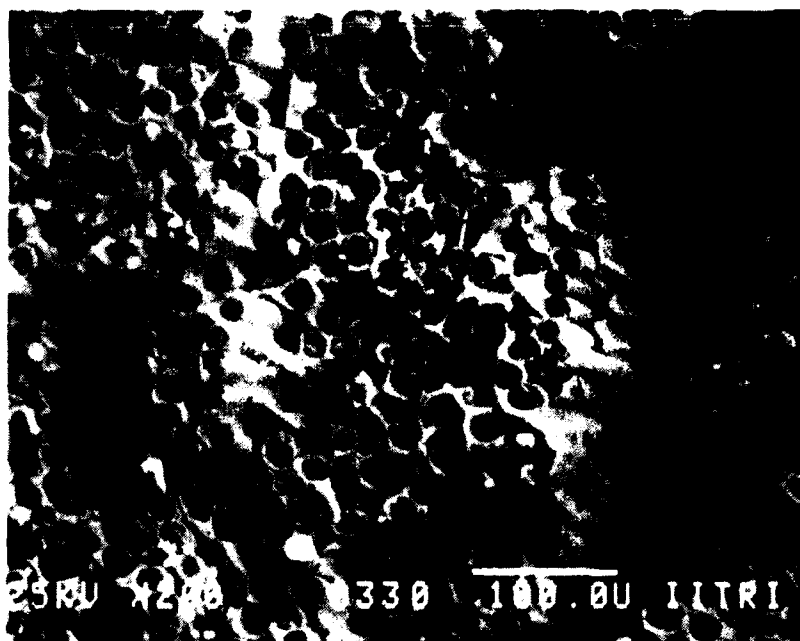
(c) View of specimen N3-3-3 in a 10° off-axis fiber region of the fracture surface.
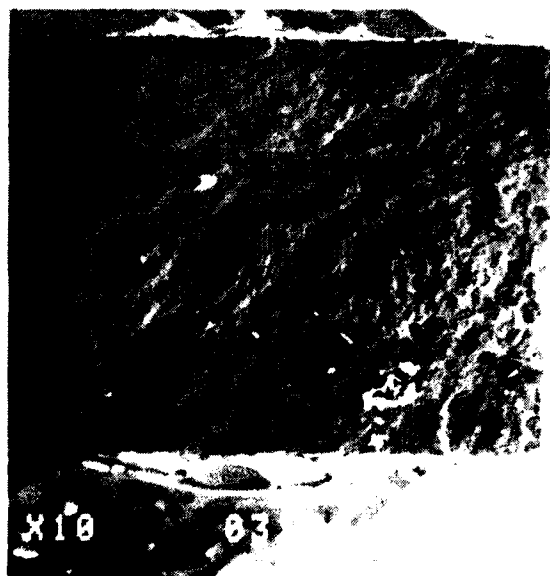
(d) SEM view of specimen N3-1-1 (+20° off-axis fibers) fracture origin $\bar{\text{is}}$ in the upper righthand corner.

Figure 46. (cont.)

(e) View of origin area showing the aligned/off-axis
    fiber interface region (specimen N3-1-1).
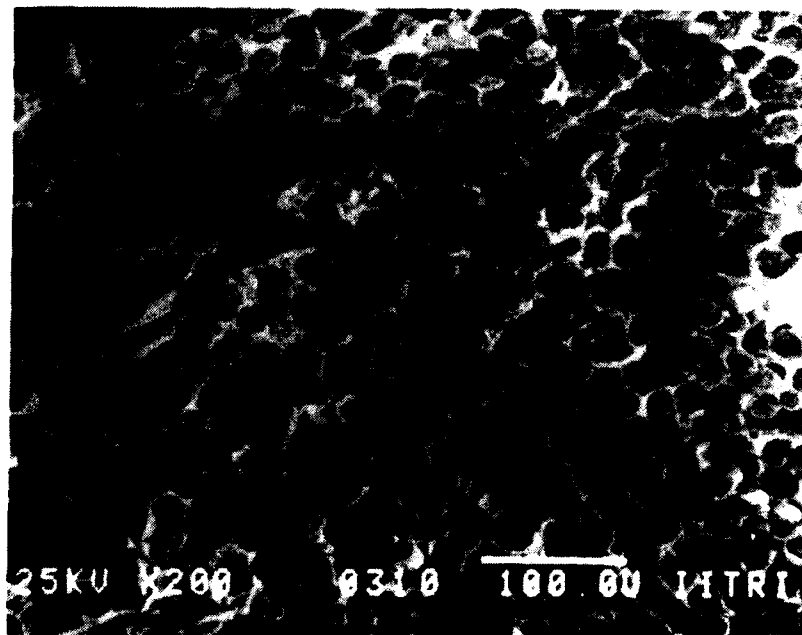
(f) View of specimen N3-1-1 in the 0° fiber portion
    of the fracture surface.

Figure 46. (cont.)
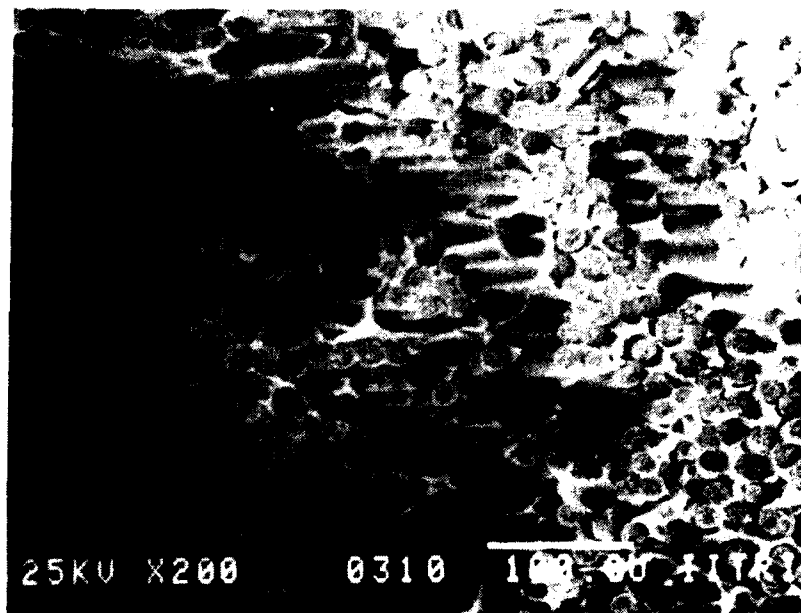
(g) View of specimen N3-1-1 in a 20° off-axis region of the fracture surface.
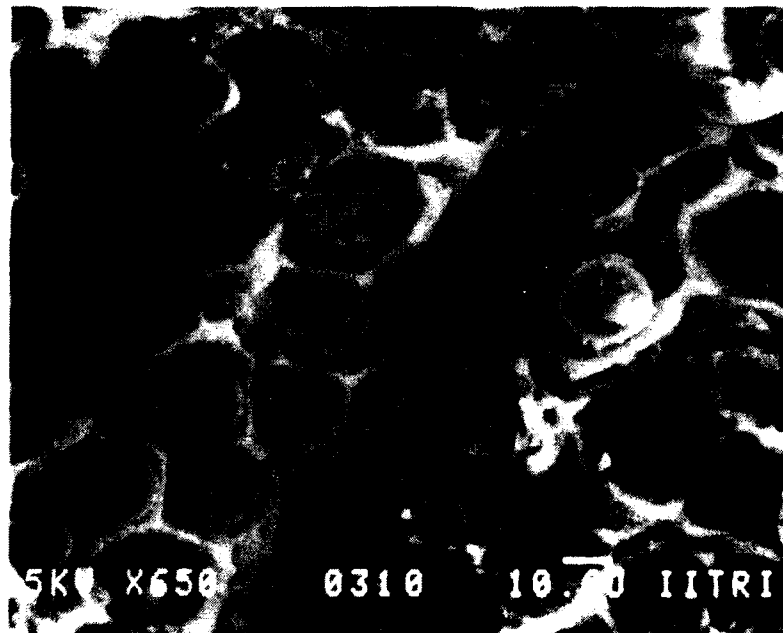
(h) View of specimen N3-1-1 showing the brittle Al_2O_3 fiber fracture and the "cone" portion of the ductile Mg "cup and cone" fracture.

Figure 46.   (cont.)

78

The off-axis portions of the fracture surfaces indicate that the fibers failed in a brittle manner. There is little evidence of fiber pull-out. Figure 46h, photographed in the 0° portion of the fracture surface, indicates the ductile failure of the matrix.

Butted and 1/10 in. Gap Fiber Fracture Specimens (Type N4)

Three tensile samples were prepared from billet N4-3 so as to contain a 1/10 in. fiber gap region in the gage section. This flaw, as-fabricated, was somewhat larger and was the origin for each sample tested. An example is shown in Figure 47. A more discrete form of the same flaw type was fabricated into the N4-1 billet where a fiber fracture was simulated by one butted layer of cut Al_2O_3 fibers. The fracture surfaces of these samples were flatter than those of the 1/10 in. gap samples. Fracture origins were again at the discontinuity formed by the butted fiber layer for specimens N4-1-1 and N4-1-3. A slight Mg-rich region may be seen on the typical fracture surface shown in Figure 48. The region indicates the location of the cut and butted fiber layer. Specimen N4-1-2 fractured at one end of the gage section, not at the centrally located abutment. The fracture surface features were similar to those seen on unflawed tensile specimens, with the fracture origin not identified.

Fiber/Matrix Debonding Specimens (Type N5)

Samples having a region of fiber/matrix debonding within the gage section of a tensile coupon exhibited the most surface irregularity and no evidence of brittle failure. The delaminated region was the fracture origin in each sample tested, as seen in Figure 49.

~1X

(a) Side view of three 1/10 in. gap tensile samples showing fracture at the metal-rich region of the gage section.
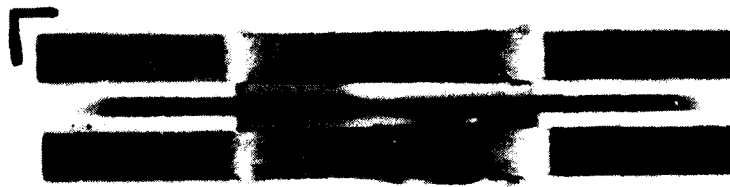

6X
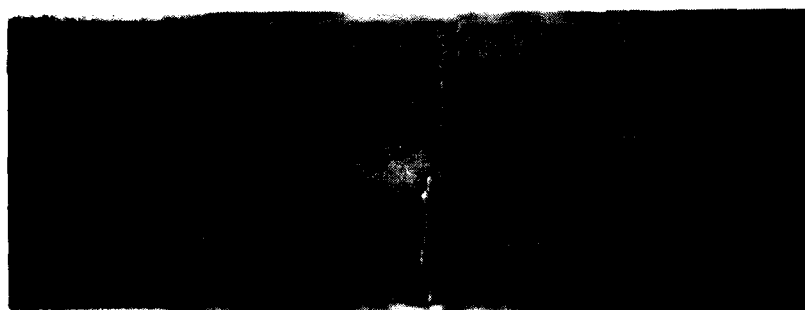
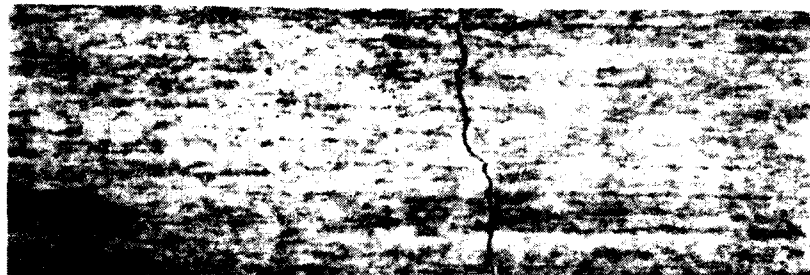(b) Magnified view of specimen N4-3-1 oriented as above.

7X

(c) Fracture surface of specimen N4-3-3.

Figure 47. Fractures of type N4-3 (1/10 in. gap) material showing failure at the metal-rich region of each specimen.
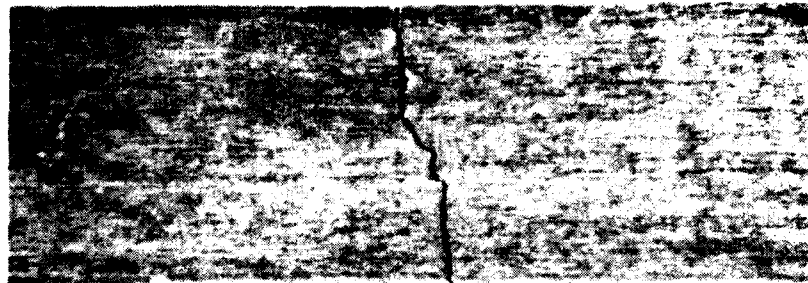
80

1X

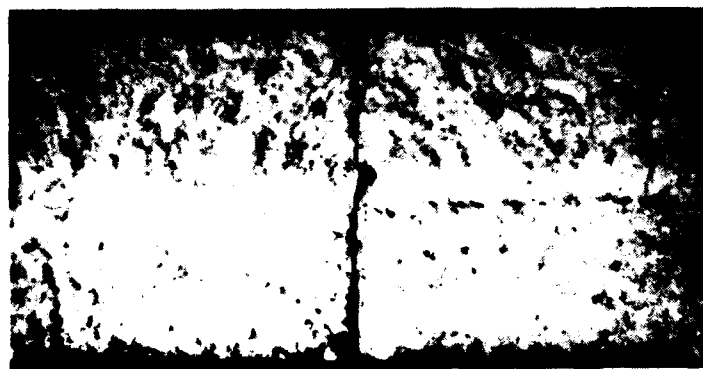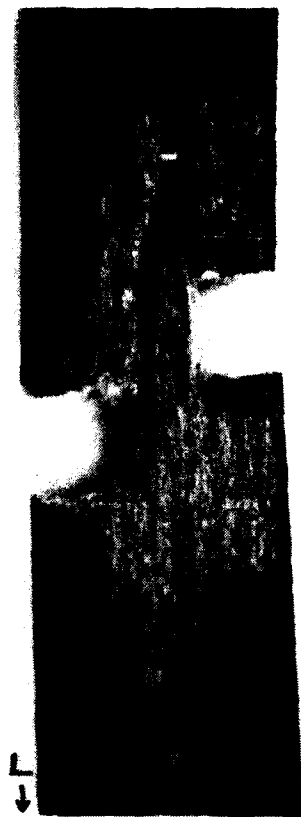(a) Side view of butted fiber tensile specimens showing fracture at the centrally located flaw.

N4-1-1

N4-1-3

6X

(b) Magnified view of specimens oriented as above.

7.5X

(c) Fracture surface of specimen N4-1-1.

Figure 48. *Fractures of type N4-1 (butted fibers) material showing failure at the flaw centrally located in the gage section.*

81

(a) Schematic showing specimen removal location superimposed on coupon analog C-scan.

(b) Top and side views of tested specimens showing failure in the delamination region.

N5-1-1

N5-1-2

~1X

(c) Magnified view of the delamination of specimen N5-1-1.

5.5X

(d) Fracture surface of specimen N5-1-2 showing the separated delamination portion of the sample (edge surfaces together).

5X

Figure 49. *Fracture surfaces of type N5 (fiber/matrix debonding) material showing failure at the delaminated region of the specimen.*

4. SUMMARY

The objective of this program was to apply nondestructive evaluation methods to assess the integrity of FP/magnesium composites containing specified defect types, establish detectability and reproducibility limits of NDE, and establish relationships between detected defects, mechanical properties, and the microstructure. The program was performed using an existing ultrasonic detection and recording system with compression wave transducers operated in the pulse-echo mode at various frequencies up to 20 MHz. The ultrasonic inspection and wave propagation velocity techniques were applicable to all flaw types, although neither could detect misaligned fibers well.

For all of the flaw types investigated, ultrasonic scanning was capable of clearly and reproducibly defining the presence and extent of the intentional defects. These results indicate that a wide range of defect types can be revealed using off-the-shelf NDE hardware operated under conditions representative of field service conditions, even though testing was actually in a research environment. These results must be qualified within the restriction that each coupon contained one defect type exclusively. None of the coupons exhibited a combination of defects. There was no opportunity, therefore, to investigate superposition effects of one defect overlapping one or more other defects. Based on the results of the off-axis fiber coupon which included an overlapped defect, it is questionable whether a low attenuative defect (off-axis fibers) would be detected behind a highly attenuative defect (porosity) using the simple, relatively low-energy scanning inspection techniques applied within this program.

In general terms, the wave propagation and wave attenuation coefficient data supported the ultrasonic inspections. For highly attenuative defects (porosity, fiber/matrix debonding), it is obvious that the data indicate the presence of the gross intentional defects. For defects involving a small surface area, or deep within the laminate plies (butted fiber fracture), the data were inconclusive on a comparative basis ("good" versus "defect" material) within a coupon.

As a mechanism for qualifying the nature of a defect, the data values do not vary from defect to defect sufficiently in magnitude to establish a one-to-one correlation between data value and defect type. Wave velocity and attenuation coefficient data continue to provide an excellent medium to corroborate ultrasonic inspection as to the severity of a defect, or the possible presence of multiple or overlapping defects. As an example, this method distinguished between porosity and delamination defects according to the magnitudes of the wave attenuation coefficient data.

The mechanical properties generally corresponded well with the induced flaws. All unflawed specimens tested in flexure (unflawed coupons and un-flawed specimens taken from N1 porosity coupons based on NDE results) agreed. Flawed and unflawed fiber/matrix debonding (N5) 0° flexure specimens exhibited the same strength and modulus values because the flawed, debonded region fell along the neutral axis of the flexure sample. Interestingly, no shear failures were observed in the flawed specimens.

Tensile specimens did not show wide variation in strength with respect to defect type. Lowest values were recorded for specimens with nonuniform fiber volume ratios (Type N2), where failure origins were in the metal-rich regions. As predicted theoretically, the ±20° off-axis specimens had slightly lower strengths than ±10° off-axis specimens.

Microstructural and fracture surface analysis corroborated all previous results, while adding details beyond NDE detectability levels. Specifics such as surface pitting, large diameter fibers, metal-rich regions, off-axis fibers, and defect volume were illuminated by microscopy techniques.

No single NDE technique that was evaluated can provide all the information required to adequately define the state of material integrity of FP/Mg composites. However, reproducibility of NDE techniques was excellent.

An encouraging result of this program is that although the FP/Mg composite is a relatively sophisticated material to fabricate and use, its integrity can be reproducibly determined without using exotic inspection techniques or equipment. Even with gross flaws, its mechanical properties appear fairly uniform. Selected microscopy can enhance NDE evaluation. Future work should perhaps be directed toward NDE determination of multiple defects, and more subtle, property-limiting manufacturing defect.

REFERENCES

1. *Hybrid and Select Metal Matrix Composite*, Ed. by W. J. Renton, American Institute of Aeronautics and Astronautics, New York, 1977.

2. McMaster, R. C., Ed., *Nondestructive Testing Handbook*, The Ronald Press, New York, 1963.

3. Krautkramer, J. and Krautkramer, H., *Ultrasonic Testing of Materials*, Springer-Verlag, Inc., New York, 1969.

4. Fredric, J. R., *Ultrasonic Engineering*, John Wiley & Sons, Inc., New York, 1965.

5. Rose, J. L., Carson, J. M., and Leidel, D. J., "Ultrasonic Procedures for Fibers and Composites," ASTM STP 521, pp. 311-325, 1973.

6. Gericke, O. R., "Ultrasonic Spectroscopy," in *Research Techniques in Nondestructive Testing*, Sharpe, R. S., Ed., Academic Press, New York, pp. 31-61, 1970.

7. Chang, F. H., Kline, R. A., and Bell, J. R., "Ultrasonic Evaluation of Adhesive Bond Strength Using Spectroscopic Techniques," General Dynamics, Fort Worth Division, Proceedings ARPA/AFML Review of Progress in Quantitative NDE, Scripps Institution of Oceanography, La Jolla, Calif., July 18-21, 1978.

8. "Interdisciplinary Program for Quantitative Flaw Detection," Rockwell International Science Center, Contract No. F33615-74-C-5180, for ARPA/AFML, September, 1975.

9. Mucciardi, A. N., et al., "Adaptive Nonlinear Signal Processing for Characterization of Ultrasonic NDE Waveforms," Task 2, Measurement of Subsurface Fatigue Crack Size, Technical Report AFML-TR-76-44, April 1976.

10. Blake, R. A., "Computer Aided Ultrasonic Flaw Growth Characterization in Composite Structures," presented at ARPA/AFML Review of Progress in Quantitative NDE, University of California, San Diego, Calif., July 8-13, 1984.

11. Schramm, S. W., and Daniel, I. M., "Nondestructive Evaluation of Metal Matrix Composites," Technical Report AMMRC-TR-82-35, May 1982.

12. Dhingra, A. K., "Inorganic Alumina Fibers for Reinforcement of Metal Castings," E. I. DuPont De Nemours & Co., Inc., p. 19.

13. "Tensile Properties of Fiber-Reinforced Metal Matrix Composites," ASTM Standard D 3552-77, Part 36, 1982

APPENDIX
SPECIMEN FABRICATION AND NDE OF AS-CAST PLATES

A1. NONDESTRUCTIVE EVALUATION OF AS-CAST PLATES

The results of NDE inspections are shown in Figures A1 through A5. All of the C-scans were generated using a 15 MHz, focused, compression wave transducer operated in the pulse-echo mode.

Figure A1 shows the C-scan for the casting plate with porosity. This C-scan indicates "apparent porosity" distributed evenly throughout the specimen. Since the purpose of the preliminary inspections was to determine the positions from which the final coupons are to be machined, and not to quantify the defects indicated, the recommendation given was that the four final coupons be machined from anywhere on the plate.

Figure A2 shows the C-scan for the casting plate with nonuniform volume fraction. The two areas of different fiber volume ratio can be clearly seen in the C-scan. The upper (densely lined) area represents the 55% fiber volume ratio, and the lower (sparsely lined) area represents the 30% fiber volume ratio. The final coupons were machined from the casting plate in such a way that no less than one-third of the coupon contained either of the two fiber volume ratios.

Figure A3 shows the C-scan for the casting plate with fiber misalignment. The C-scan does not give any indication of the presence of the misaligned fibers, but does indicate that the plate lacked any gross defects which would prohibit the final machining of coupons from anywhere on the plate. Two coupons each were machined from the casting plate symmetrically across the centerline which separates the ±10° from ±20° off-axis fibers.

Figure A4 shows the C-scan for the casting plate with fiber fracture. The C-scan gives no indication of the location of the fiber fracture, but again indicates no areas of defects which would prohibit the machining of the final coupons. The through-the-thickness crack (highlighted by arrow) was not in a position to adversely affect the machining of the final coupons. The

Figure A1. Pen-lift C-scan of FP/Mg casting plate 246GP-1 (porosity), 15 MHz transducer in pulse-echo mode.
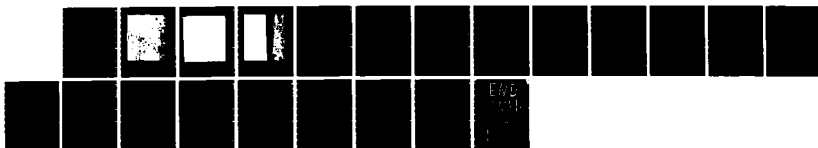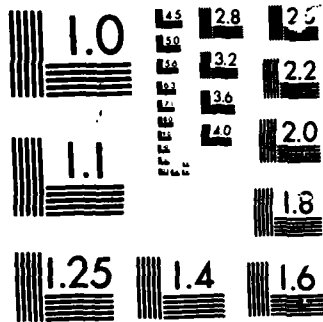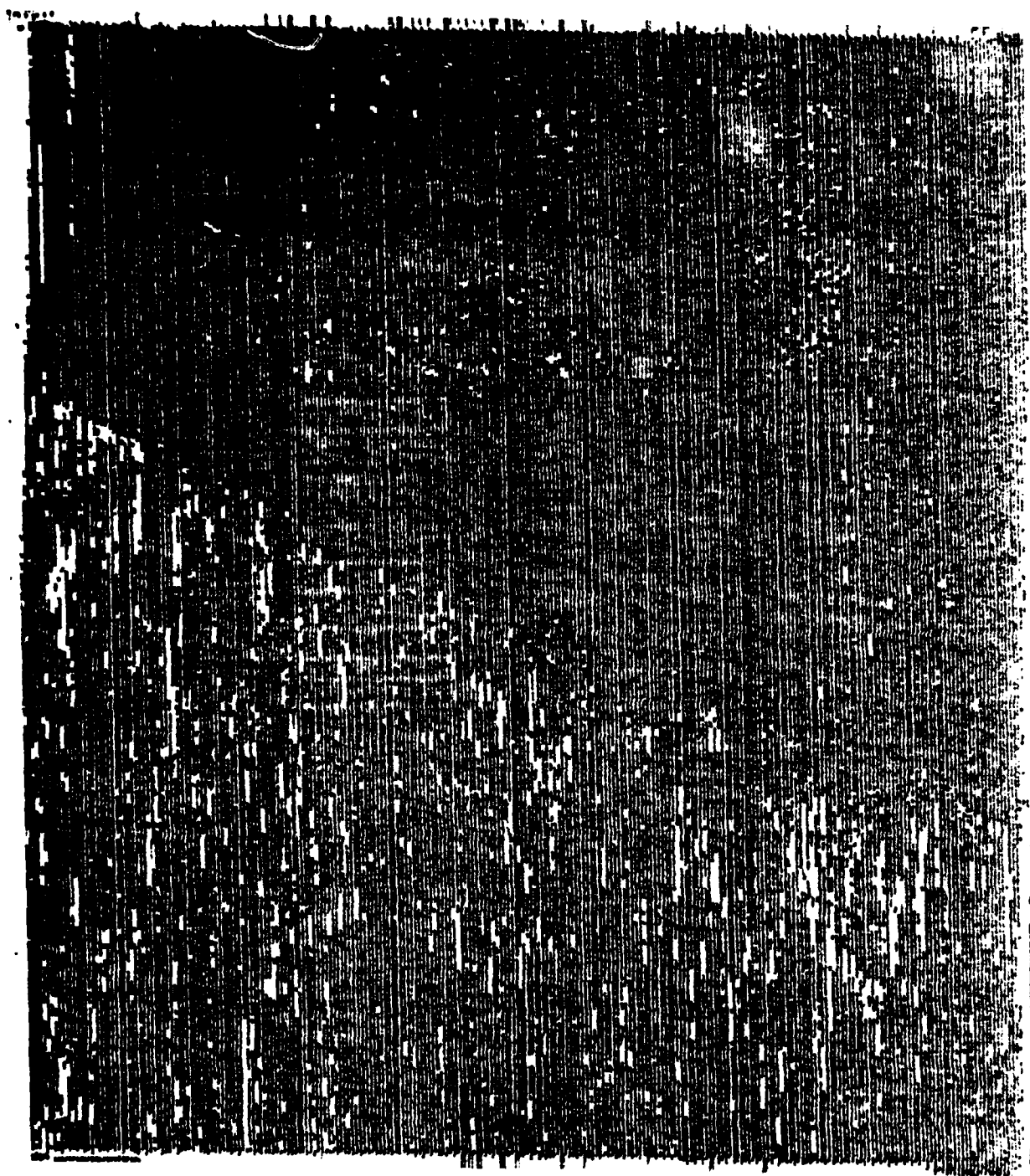
MICROCOPY CHART

Figure A2. Pen-lift C-scan of FP/Mg casting plate 246GP-2 (nonuniform fiber volume), 15 MHz transducer in pulse-echo mode.
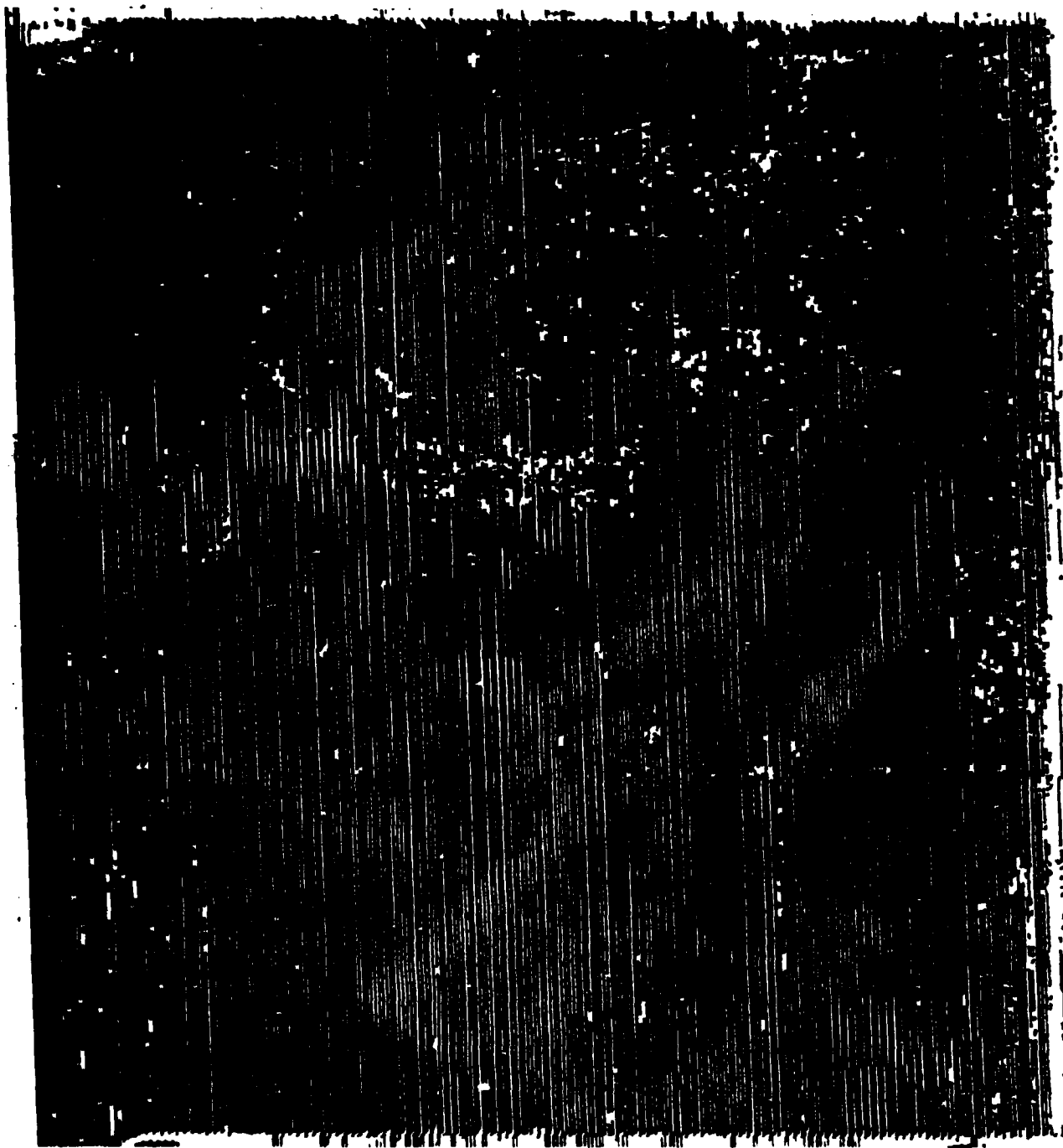
Figure A3.   Pen-lift C-scan of FP/Mg casting plate 246GP-3 (fiber misalignment),
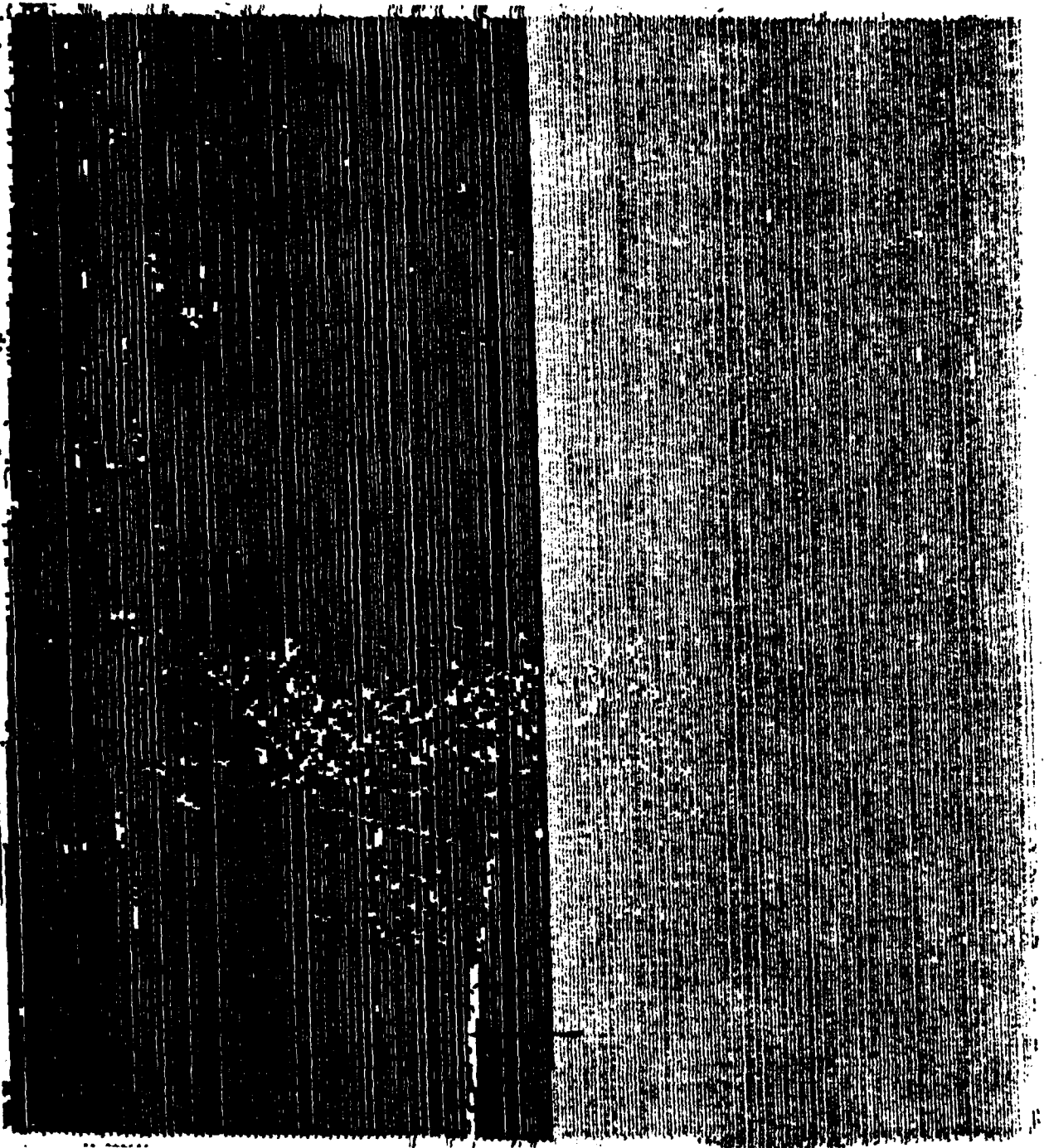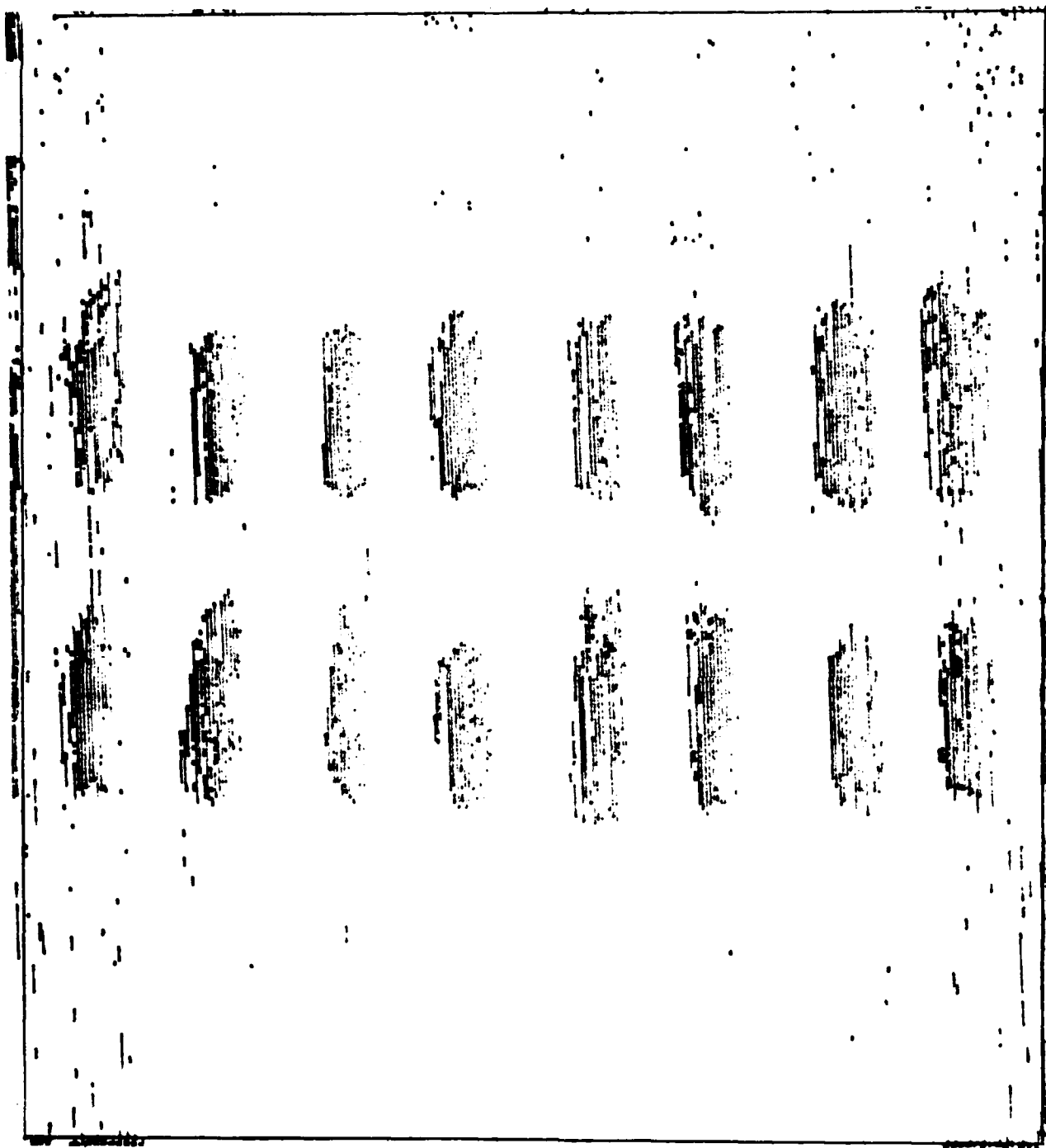15 MHz transducer in pulse-echo mode.

Figure A4. Pen-lift C-scan of FP/Mg casting plate 246GP-4 (fiber fracture), 15 MHz transducer in pulse-echo mode.

Figure A5. *Reverse pen-lift C-scan of FP/Mg casting plate 246GP-5 (fiber/matrix debonding), 15 MHz transducer in pulse-echo mode.*

final coupons were machined based on the layup sheets of the plate residing at DuPont.

Figure A5 shows the "reverse" C-scan for the casting plate with fiber/matrix debonding. In the reverse C-scan, the "defects" are shown as dark areas and the "unflawed" areas are shown as light areas. The 16 areas of fiber/matrix debonding can be clearly seen across the specimen. A-scan inspections indicated that the debonds were at or near the center of the casting plate, through-the-thickness. The coupons were final machined from the casting plate so the debonds are symmetrically centered in the plan (C-scan) view, and at the center of the specimen through-the-thickness.

A2. SPECIMEN FABRICATION

A total of twenty coupons, each 12.7 cm (5 in.) long x 3.8 cm (1.5 in.) wide x 0.6 cm (0.25 in.) thick made from ZE41A magnesium alloy reinforced with FP (aluminum oxide) fibers was fabricated. The coupons were nominally 8-ply laminates. With the exception of the four coupons of nonuniform volume fraction, the coupons had a 50% fiber volume ratio. For the fiber/matrix debonding coupons, a 17.8 x 20.3 cm (7 x 8 in.) ceramic "template" was used to selectively "burn out" the binder from one fiber ply.

The coupons were fabricated as follows:

- Porosity (N1 Type)

    Porosity was produced by depriving the casting plate of "make-up" molten magnesium alloy during the quenching/cooling process. Without the make-up molten matrix alloy there is no material to fill the shrinkage voids caused during cooling and porosity is generated.

- Nonuniform Volume Fraction, Figure A6 (N2 Type)

    Nonuniform volume fraction was produced by dividing the casting plate diagonally into two zones. One zone consisted of a volume fraction of 30% and the other zone a volume fraction of 55%. The final coupons were removed from the casting plate in such a way that a part of each zone was to be represented in each final coupon.
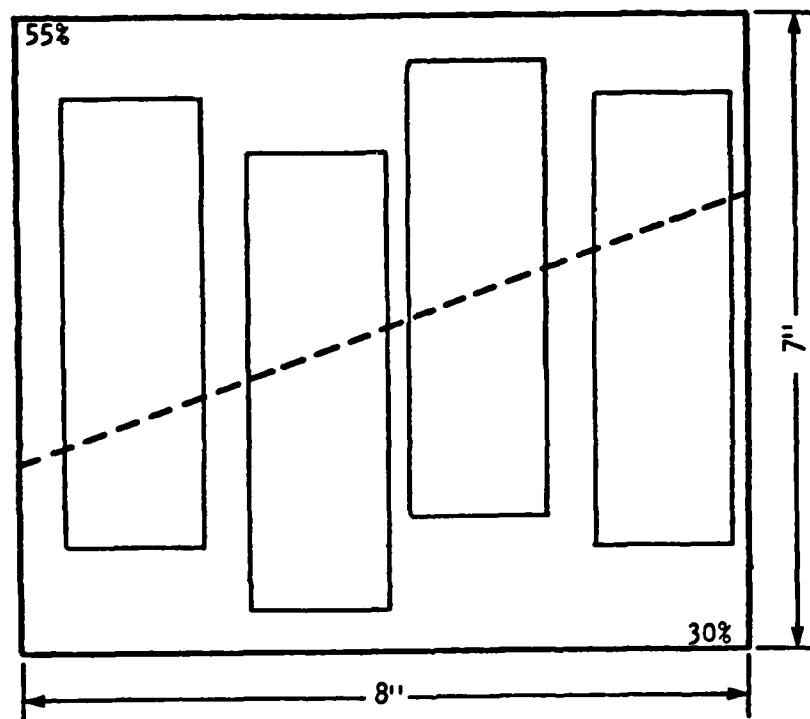
93

Figure A6. **Schematic of FP/Mg casting plate with**
nonuniform volume fraction. Possible locations
of final coupons are shown.

- Fiber Misalignment, Figure A7 (N3 Type)

  Two levels of fiber misalignment were produced in a single casting plate by dividing the casting longitudinally into two equal areas. One half of the casting had 1 ply each off-axis at +10° and -10°, respectively, while the other half of the casting had 1 ply each off-axis at +20° and -20°, respectively. The +10° and +20° off-axis fibers were the third ply while the -10° and -20° off-axis fibers were the sixth ply of the nominally 8-ply laminate, respectively.

- Fiber Fracture, Figure A8 (N4 Type)

  Two coupons each of two configurations were fabricated. Two of the coupons had 1 ply at the mid-thickness cut across the fibers which were then "butted together." The other two coupons had 1 ply at the mid-thickness cut across the fibers, with fibers separated by a 2.54 mm (0.1 in.) gap.

- Fiber Matrix Debonding, Figure A9 (N5 Type)

  On each coupon, four 1/4 in. wide x 1 in. long x 1 ply thick areas of fiber/matrix debonding was produced by burning out the fiber binder with a torch using the IITRI supplied ceramic "template." A boron nitride slurry was applied to the "burned out" areas to inhibit fiber/matrix bonding. The single ply with the "burned out" area was located at the mid-thickness of the coupon, i.e., the fourth or fifth ply of a nominally 8-ply specimen.

Upon receipt, each coupon was visually inspected for surface defects and then measured, weighed, and calculated for density. With the exception of N4-3, none of the coupons showed any surface irregularities. Coupon N4-3 had a small edge abrasion, probably a result of the crack which appeared in the preliminary ultrasonic C-scan. The abrasion was not expected to have any effect on the detectability of the fiber fracture or on any subsequent physical/mechanical tests. The physical properties listed in Table A1 represent the average of a minimum of three readings.
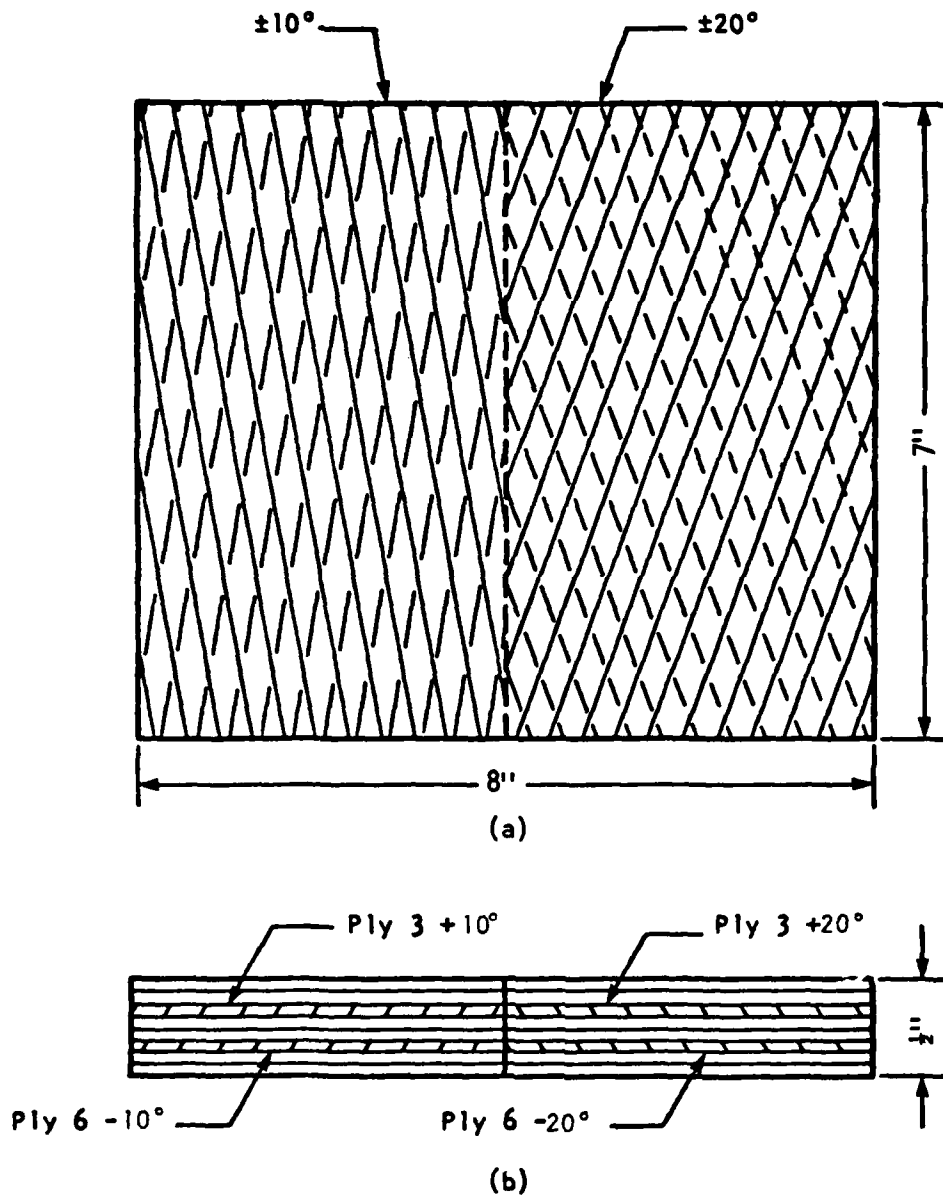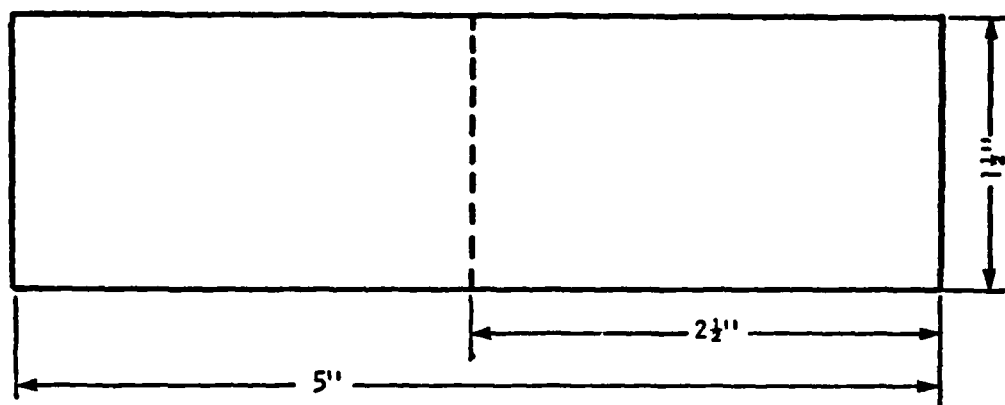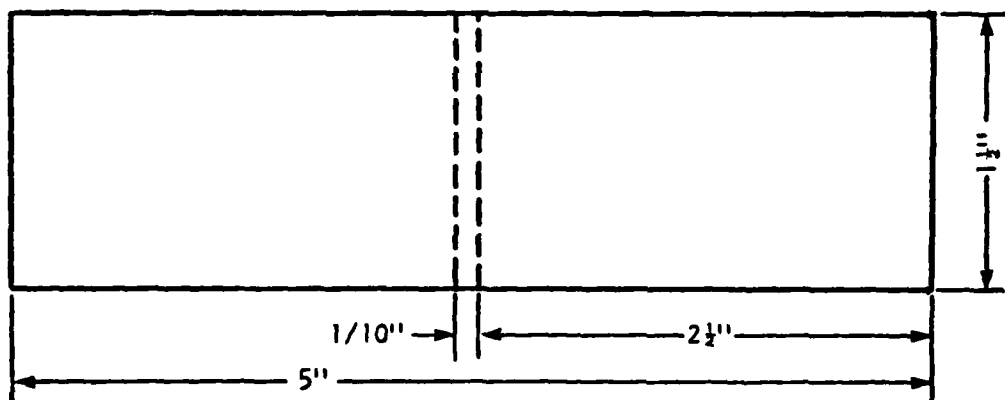
Figure A7. Schematic of FP/Mg casting plate with fiber
misalignment. (a) Separation of casting plate;
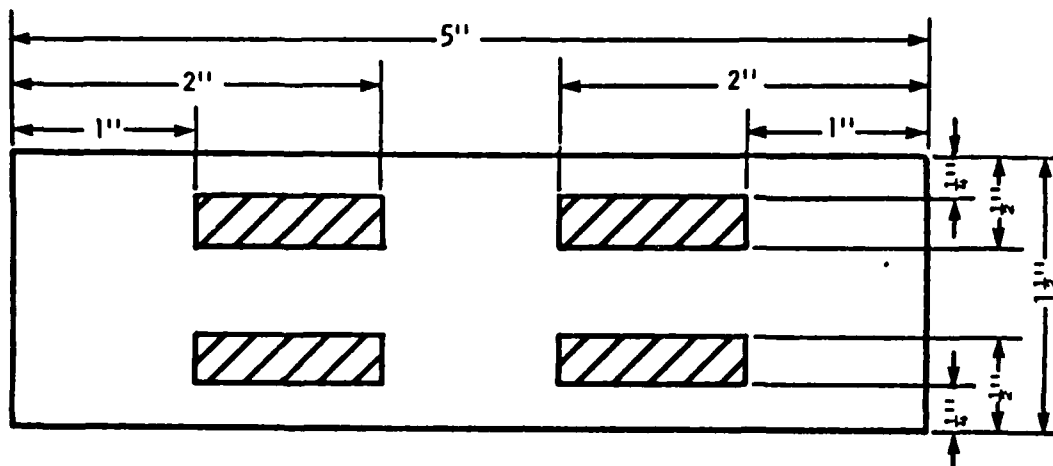(b) location of off-axis fibers through the thickness.

Figure A8. Schematic of FP/Mg coupons with fiber fracture of the fourth ply. (a) Fractured fiber ply butted together. (b) Fractured fiber ply separated by 1/10 in.

97

☑ Area of Fiber/Matrix Debonding

*Figure A9.   Schematic of FP/Mg coupon with areas of fiber/matrix
debonding of the fourth ply.*

TABLE A1. PHYSICAL PROPERTIES

Specimen		Width, mm/in.	Length, mm/in.	Depth, mm/in.	Mass, g/lb	Density, g cm^{-3}/ lb in^{-3}
Type N1:	1	38.28/1.507	127.53/5.021	6.38/0.251	88.05/0.194	2.83/0.102
	2	38.25/1.506	127.43/5.017	6.38/0.251	87.53/0.193	2.81/0.102
	3	38.28/1.507	127.41/5.016	6.38/0.251	87.43/0.192	2.81/0.102
	4	38.33/1.509	127.36/5.014	6.38/0.251	86.82/0.191	2.79/0.101
Type N2:	1	38.15/1.502	127.61/5.024	6.32/0.249	83.16/0.183	2.70/0.098
	2	38.18/1.503	127.51/5.020	6.35/0.250	83.87/0.185	2.71/0.098
	3	38.20/1.504	127.41/5.016	6.35/0.250	83.18/0.185	2.76/0.100
	4	38.15/1.502	127.46/5.018	6.35/0.250	83.36/0.183	2.70/0.098
Type N3:	1	38.15/1.502	126.92/4.997	6.55/0.258	88.88/0.196	2.80/0.101
	2	38.15/1.502	127.03/5.001	6.53/0.257	90.77/0.200	2.87/0.104
	3	38.15/1.502	127.13/5.005	6.53/0.257	90.63/0.199	2.86/0.103
	4	38.15/1.502	127.25/5.010	6.58/0.259	89.89/0.198	2.81/0.102
Type N4:	1	38.15/1.502	127.53/5.021	6.35/0.259	88.07/0.194	2.85/0.103
	2	38.15/1.502	127.46/5.021	6.35/0.250	88.10/0.196	2.89/0.104
	3	38.15/1.502	127.46/5.018	6.35/0.250	89.16/0.196	2.89/0.104
	4	38.13/1.501	127.48/5.019	6.38/0.251	86.96/0.191	2.81/0.101
Type N5:	1	38.18/1.503	127.46/5.018	6.32/0.249	86.34/0.190	2.81/0.101
	2	38.15/1.502	127.28/5.011	6.30/0.248	88.01/0.194	2.88/0.104
	3	38.13/1.501	127.91/5.036	6.30/0.248	88.28/0.194	2.87/0.104
	4	38.13/1.501	127.84/5.033	6.30/0.248	84.80/0.187	2.76/0.100

A3. FABRICATION UNDER AMMRC CONTRACT DAAG46-80-C-0070

The following is a brief description of the procedures used to generate the defects in the metal matrix specimens used in the previous project.[11]

- Type 01: <u>No intentional flaws</u>

- Type 02: <u>Fiber/Matrix Debonding</u>. The flaws were obtained by applying a release agent (boron nitride) to the two middle plies of the FP fiber stack before the magnesium alloy was introduced. The release agent prevented the matrix material from wetting the fibers.

- Type 03: <u>Porosity</u>. Porosity was produced by controlling the cooling rate and amount of make-up material added to the casting mold. By accelerated cooling and depriving the mold of make-up material, shrinkage voids, but not cracks, could be generated in the matrix.

- Type 04: <u>Fiber Misalignment, Figure A10.</u> Fiber misalignment was created by cutting the middle two plies in such a way that the fibers were oriented at 10° with the longitudinal axis of the specimen.

- Type 05: <u>Fiber Fracture, Figure A11.</u> Fiber fracture was generated by cutting the second, fourth, and sixth fiber plies at staggered positions along the length of the specimen. When the fiber plies were stacked, the cut plies were separated by approximately 0.32 cm (0.13 in.) providing a migration path for the matrix material.

- Type 06: <u>Nonuniform Fiber Distribution, Figure A12.</u> In two of the specimens, nonuniform fiber distribution was created by removing a 1.3 cm (0.5 in.) wide strip of fibers from the fourth and fifth plies of the laminate parallel to the longitudinal axis of the specimen. In the third specimen, a 1.3 cm (0.5 in.) diameter hole was cut in the fourth fiber ply near the center of the specimen.

- Type 07: <u>Matrix Fracture.</u> Matrix fracture was created by quenching the cooling casting in a liquid nitrogen bath.
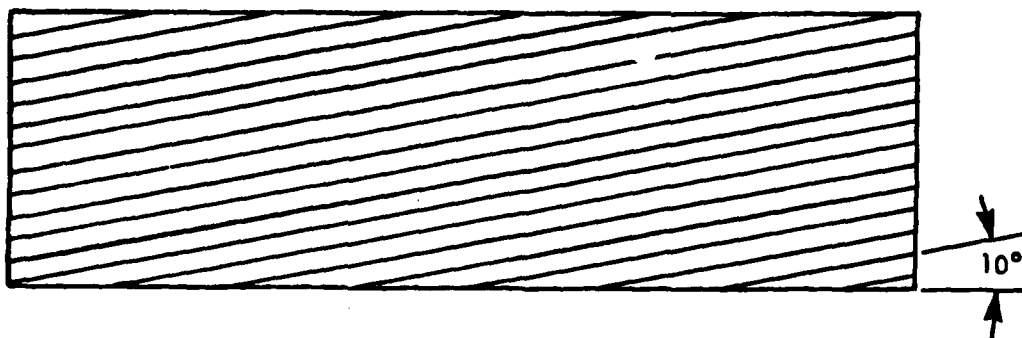
Figure A10. Fiber orientation of fourth and fifth layers of Type 04 FP/Mg specimens.
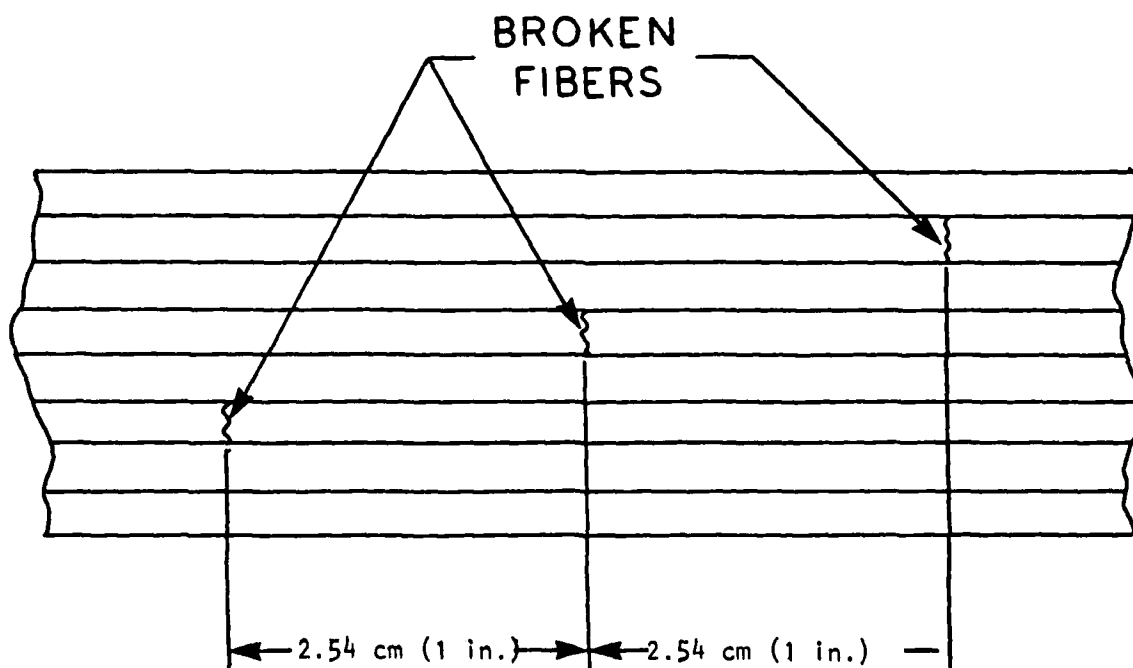
Figure A11. Fiber fracture of second, fourth, and sixth layers of Type 05 FP/Mg specimens.

(a)

1.3 cm (0.5 in.)

1.3 cm (0.5 in.) Diameter
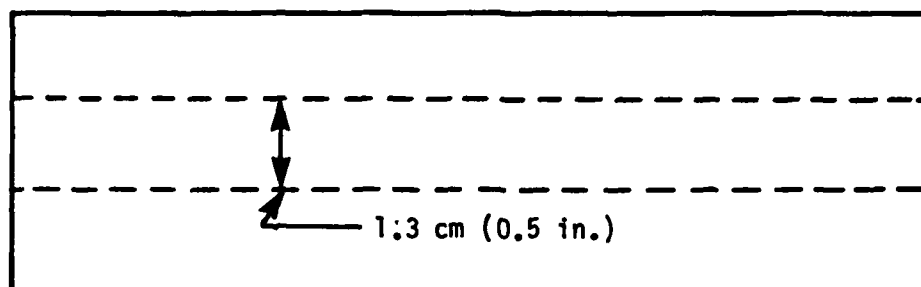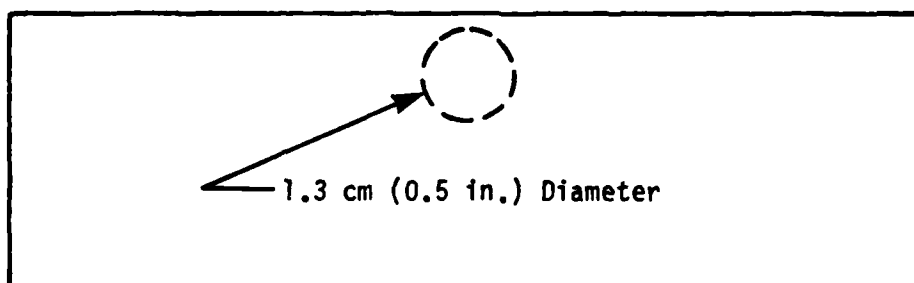
(b)

Figure A12. Areas where fibers were removed in fourth layer Type O6 FP/Mg specimens: (a) specimens O6-1 and O6-3, (b) specimen O6-2.

DISTRIBUTION LIST

No. of Copies	To

1   Office of the Under Secretary of Defense for Research and Engineering,
    The Pentagon, Washington, DC 20301

2   Commander, Defense Technical Information Center, Cameron Station, Building 5,
    5010 Duke Street, Alexandria, VA 22314

    Metals and Ceramics Information Center, Battelle Columbus Laboratories,
    505 King Avenue, Columbus, OH 43201
1   ATTN: Mr. Robert J. Fiorentino, Program Manager

1   Defense Advanced Research Projects Agency, Defense Sciences Office/MSD,
    1400 Wilson Boulevard, Arlington, VA 22209

    Headquarters, Department of the Army, Washington, DC 20314
1   ATTN: DAEN-RDM, Mr. J. J. Healy

    Commander, U.S. Air Force Wright Aeronautical Laboratories, Wright-Patterson
    Air Force Base, OH 45433
1   ATTN: AFWAL/MLC
1   AFWAL/MLLP, D. M. Forney, Jr.
1   AFWAL/MLBC, Mr. Stanley Schulman
1   AFWAL/MLLS, Dr. Terence M. F. Ronald
1   AFWAL/FIBEC, Dr. Steve Johnson

1   Edward J. Morrissey, AFWAL/MLTE, Wright-Patterson Air Force Base, OH 45433

    Commander, Army Research Office, P.O. Box 12211, Research Triangle Park,
    NC 27709
1   ATTN: Information Processing Office
1   Dr. George Mayer

    Commander, U.S. Army Materiel Command, (AMC), 5001 Eisenhower Avenue,
    Alexandria, VA 22333
1   ATTN: AMCLD

    Commander, U.S. Army Armament, Munitions and Chemical Command,
    Dover, NJ 07801
1   ATTN: AMDAR-SCM, J. D. Corrie
1   Mr. Harry E. Pebly, Jr., PLASTEC, Director

    Commander, U.S. Army Aviation Systems Command, 4300 Goodfellow Blvd., St. Louis,
    MO 63120
1   ATTN: AMDAV-NS, Harold Law

    Director, U.S. Army Ballistic Research Laboratory, Aberdeen Proving Ground,
    MD 21005
1   ATTN: AMDAR-TSB-S (STINFO)

No. of Copies	To

Commander, U.S. Army Electronics Research and Development Command, Fort Monmouth, NJ 07703
1 ATTN: AMDSD-L
1   AMDSD-E

Commander, U.S. Army Foreign Science and Technology Center, 220 7th Street, N.E., Charlottesville, VA 22901
1 ATTN: Military Tech, Mr. Marley

Commander, U.S. Army Materiel Systems Analysis Activity, Aberdeen Proving Ground, MD 21005
1 ATTN: AMXSY-MP, H. Cohen

Commander, U.S. Army Missile Command, Redstone Arsenal, AL 35898
1 ATTN: Technical Library
1   AMSMI-RLM
1   AMSMI-RLA, Dr. James J. Richardson

Commander, U.S. Army Belvoir Research and Development Center, Fort Belvoir, VA 22060
1 ATTN: STRBE-D
1   STRBE-G
1   STRBE-X
1   STRBE-N
1   STRBE-VL

Commander, U.S. Army Research and Technology Labs, Applied Technology Laboratory (AVSCOM), Fort Eustis, VA 23604
1 ATTN: AMDAR-ATL-ATP, Mr. James Gomez, Aerospace Engineer

Commander, U.S. Army Tank-Automotive Command, Warren, MI 48090
1 ATTN: AMSTA-RCKM

Director, Benet Weapons Laboratory, LCWSL, USA AMCOM, Watervliet, NY 12189
1 ATTN: AMSMC-LCB-TL
1   AMSMC-LCB-PS, Dr. I. Ahmad

David Taylor Naval Ship Research and Development Center, Annapolis, MD 21402
1 ATTN: Dr. Michael Vassilaros - Code 2814

Office of Naval Technology, 800 N. Quincy Street, Arlington, VA 20017
1 ATTN: Mr. J. J. Kelly - Code MAT 0715

Naval Research Laboratory, Washington, DC 20375
1 ATTN: Dr. C. I. Chang - Code 5830
1   Dr. G. R. Yoder - Code 6384
1   Dr. S. C. Sanday - Code 6370

Chief of Naval Research, Arlington, VA 22217
1 ATTN: Code 471
1   Dr. Steven G. Fishman

No. of Copies	To

Naval Sea Systems Command, Washington, DC   20362
1   ATTN: Mr. Marlin Kinna - 62R4

Naval Air Development Center, Warminster, PA   18974
1   ATTN: Dr. E. U. Lee - Code 60632

Naval Surface Weapons Center, White Oak, Silver Spring, MD   20910
1   ATTN: John V. Foltz - Code R32
1   Dr. Herbert Newborn - Code R34

National Aeronautics and Space Administration, Washington, DC   20546
1   ATTN: Mr. G. C. Deutsch - Code RW
1   Mr. Michael A. Greenfield, Program Manager for Materials, Code RTM-6

National Aeronautics and Space Administration, Lewis Research Center,
Cleveland, OH   44135
1   ATTN: Dr. James A. DiCarlo, Mail Stop 106-1

National Aeronautics and Space Administration, Marshall Space Flight Center,
Huntsville, AL   35812
1   ATTN: R. J. Schwinghammer, EH01, Dir, M&P Lab
1   Mr. W. A. Wilson, EH41, Bldg. 4612

The Boeing Vertol Company, P.O. Box 16858, Philadelphia, PA   19142
1   ATTN: Mr. Robert L. Pinckney, Mail Stop P62-06
1   Mr. Joseph W. Lenski, Jr., Mail Stop P32-09

E. I. DuPont De Nemours and Company, Inc., Textile Fibers Department,
Pioneering Research Laboratory, Experimental Station, Wilmington, DE   19898
1   ATTN: Blake R. Bichlmeir
1   Joyce W. Widrig

1   Mr. Rex C. Claridge, TRW, Incorporated, Manufacturing Division,
    Mail Stop 01-2210, 1 Space Park, Redondo Beach, CA   90278

1   Dr. James A. Cornie, Materials Processing Center, Bldg. 8, Room 237,
    Massachusetts Institute of Technology, 77 Massachusetts Avenue,
    Cambridge, MA   01239

1   Dr. Bhagwam K. Das, Engineering Technology Supervisor, The Boeing Company,
    P.O. Box 3999, Seattle, WA   98124

1   Leroy Davis, NETCO, 2225 East 28th Street, Building 5, Long Beach, CA   90806

1   Mr. Joseph F. Dolowy, Jr., President, DWA Composite Specialties, Inc.,
    21133 Superior Street, Chatsworth, CA   91311

1   Mr. Robert E. Fisher, President, AMERCOM, Inc., 8948 Fullbright Avenue,
    Chatsworth, CA   91311

No. of Copies	To

1 Mr. Louis A. Gonzalez, Kaman Tempo, 816 State Street, Santa Barbara, CA 9310!

1 Prof. James G. Goree, Dept. of Mechanical Engineering, Clemson University, Clemson, SC 29631

1 William F. Grant, AVCO Specialty Materials Division, 2 Industrial Avenue, Lowell, MA 01851

1 Mr. Jacob Gubbay, Charles Stark Draper Laboratories, 555 Technology Square, Mail Station 27, Cambridge, MA 02139

1 Mr. John E. Hack, Southwest Research Institute, 6220 Culebra Road, San Antonio, TX 78284

1 Dr. H. A. Katzman, The Aerospace Corporation, P.O. Box 92957 Los Angeles, CA 90009

Lockheed California Company, Burbank, CA 91520
1 ATTN: Mr. Rod F. Simenz, Department of Materials and Processes

Lockheed Georgia Company, 86 South Cobb Drive, Marietta, GA 30063
1 ATTN: Materials and Processes Engineering Department
1   Mr. James Carroll

Material Concepts, Inc., 2747 Harrison Road, Columbus, OH 43204
1 ATTN: Mr. Stan J. Paprocki
1   Mr. David Goddard

1 Dr. Mohan S. Misra, Martin Marietta Aerospace, P.O. Box 179, Denver, CO 80201

1 Mr. Patrick J. Moore, Staff Engineer, Lockheed Missiles and Space Company, Organization 62-60, Building 104, P.O. Box 504, Sunnyvale, CA 94086

1 R. Byron Pipes, Professor & Director, Center for Composite Materials, University of Delaware, Newark, DE 19711

1 Dr. Karl M. Prewo, Principal Scientist, United Technologies Research Center, Mail Stop 24, East Hartford, CT 06108

1 Dr. B. W. Rosen, Materials Sciences Corporation, Gwynedd Plaza 11, Bethlehem Pike, Spring House, PA 19477

1 Prof. Marc H. Richman, Division of Engineering, Brown University, Providence, RI 02912

1 Mr. Ronald P. Tye, Energy Materials Testing Laboratory, Biddeford Industrial Park, Biddeford, ME 04005

1 Mr. Robert C. Van Siclen, Vought Corporation, Advanced Technology Center, P.O. Box 226144, Dallas, TX 75266

No. of Copies	To
1	Prof. Franklin E. Wawner, Department of Materials Science, School of Engineering and Applied Sciences, University of Virginia, Charlottesville, VA 22903
1	Dr. Carl Zweben, General Electric Company, Valley Forge Space Center/M4018, P.O.Box 8555, Philadelphia, PA 19101

Commander, U.S. Army Laboratory Command, 2800 Powder Mill Road, Adelphia, MD 20783-1197
1 ATTN: Technical Library

Director, U.S. Army Materials Technology Laboratory, Watertown, MA 02172-0001
2 ATTN: SLCMT-IML
1 SLCMT-IMA-P
1 SLCMT-ISC
10 John Nunes

U.S. Army Materials Technology Laboratory
Watertown, Massachusetts 02172-0001
NONDESTRUCTIVE EVALUATION
OF METAL MATRIX COMPOSITES
S. N. Schramm, G. M. Koller, and J. M. Adams
IIT Research Institute
10 West 35th Street
Chicago, IL 60616
Technical Report MTL TR 85-31, December 1985, 107 pp.
D/A Project 1L263102071
Illus-tables, Contract DAAG-82-C-0039
Final Report, April 1982 to June 1984

Key Words

Metal matrix composites
Nondestructive testing
Fiber-reinforced composites
Magnesium
Castings
Aluminum oxide

The objective of this program was to apply nondestructive evaluation (NDE) methods to identify potentially harmful casting defects in FP/magnesium composites; establish detectability and reproducibility limits of NDE applied to FP/magnesium composites; and establish relationships between casting defects and failure modes of FP/magnesium composites. The material investigated was ZE41A magnesium alloy reinforced with FP (aluminum oxide) fibers. The 27 coupons (4 coupons each of 5 flaw types and 7 coupons from a related program, Contract No. DAAG46-80-C-0070) were evaluated using ultrasonic scanning, wave propagation velocity, and wave attenuation inspection techniques. The coupons evaluated were 12.7 cm (5 in.) long x 3.8 cm (1.5 in.) wide x 0.6 cm (0.25 in.) thick, with a fiber volume fraction of 0.50. After the detectability and reproducibility NDE inspections, tensile and/or bend specimens were machined from the parent coupons, strain gaged, and statically loaded to failure. Micrographs were made of the fracture surfaces for comparison with the NDE records. It was found that ultrasonic scanning using a 20 MHz compression wave, focused transducer operated in the pulse-echo mode generating an analog C-scan provided 100% detectability and reproducibility of the intentionally flawed coupons.

END
FILMED

5-86

DTIC